

THE RESEARCH AND DEVELOPMENT OF SUB-MICRON GAP
NANODIAMOND LATERAL FIELD EMISSION DIODES

By

Xuan-Anh Celestina LeQuan

Dissertation

Submitted to the Faculty of the
Graduate School of Vanderbilt University
in partial fulfillment of the requirements

for the degree of

DOCTOR OF PHILOSOPHY

in

Electrical Engineering

December, 2010

Nashville, Tennessee

Approved:

Weng Poo Kang

Jim Davidson

Bo. K. Choi

Bharat Bhuva

Alvin M. Strauss

Sharon M. Weiss

Above all else, Soli DEO Gloria

To my beloved family.

ACKNOWLEDGEMENTS

A very special thank you to my advisor, Professor Weng Poo Kang, for giving me this valuable research opportunity. I truly admire your technical expertise and ingenuity. Professor Davidson, a.k.a., Dr. D, your business acumen is unparalleled; thank you for being so supportive of me and for actively providing me with the guidance to complete my Ph.D. Professor Kang and Professor Davidson, thank you for offering me a conducive environment for fulfilling my research goals. Thank you to Professor Choi for taking the time to teach me the various lab tools and processes. I am also grateful to Professor Bhuvra, Professor Weiss, and Professor Strauss for serving on my Ph.D. Committee. I will always remember your advocacy.

To my grandmother, Ngoai, your wise words will never part from me. I miss you dearly. My loving parents Mr. and Mrs. Huy and Anh LeQuan, amazing sister Christina, and baby brothers Jonathan and David have instilled in me the motivation to keep forging ahead even when I was in great despair. I can never thank you enough.

TABLE OF CONTENTS

DEDICATION	ii
ACKNOWLEDGEMENTS	iii
LIST OF FIGURES	vii
LIST OF TABLES	xi
ABBREVIATIONS	xii
1 INTRODUCTION	1
1.1 Overview and motivation for sub-micron gap nanodiamond lateral device.....	2
1.2 Introduction to nanodiamond as a cathode material	3
1.2.1 Field emission enhancement by doping	3
1.2.2 The role of sp^2	4
1.3 Advantages of lateral field emission devices.....	5
1.4 Objective of this research.....	6
1.5 Organization of this dissertation	7
2 OVERVIEW OF ELECTRON EMISSION	8
2.1 Electron emission into vacuum	8
2.1.1 Fowler-Nordheim tunneling.....	9
2.1.2 Field-enhanced thermionic emission	10
2.2 Bulk electron conduction mechanism	12
2.2.1 Space charge limited current.....	12
2.2.2 Poole-Frenkel.....	13
2.3 MIM model overview	14
2.3.1 Electron emission based on MIM model	14
2.4 Summary of models	16
3 NANODIAMOND	17
3.1 Diamond deposition techniques	17
3.1.1 Reported work on diamond.....	18
3.2 Macroscopic electron emission from diamond films.....	21
3.2.1 Hybrid conduction models.....	22
3.3 Tools for monitoring electronic changes in diamond	24

3.3.1 Field emission test set-up for CVD diamond films	26
3.4 The effect of sp^2/sp^3 hybridized bonding content on the field emission characteristics of nanodiamond.....	26
3.4.1 XPS Results	27
3.4.2 Three-film field emission performance	31
3.4.3 Study summary	32
3.5 Micro-Raman and electron field emission characterization	33
3.5.1 Surface preparation techniques	34
3.5.2 Raman spectra.....	36
3.5.3 Five-film field emission performance.....	37
3.5.4 Study summary	39
3.6 Nanodiamond film study conclusions.....	40
4 SUB-MICRON GAP RESEARCH APPROACH	41
4.1 Overview of lateral device in diode configuration	42
4.2 Process development for fabrication.....	43
4.3 Lateral device field emission characterization.....	45
4.3.1 Device conditioning	46
5 DEVICE FABRICATION AND CHARACTERIZATION	48
5.1 Experimental	48
5.1.1 The identification of metal masking material	48
5.1.2 EBL parameters	50
5.1.3 Study summary	54
5.2 Mixed lithography approach and CHF_3/O_2 fluorine-based diamond etch.....	54
5.2.1 CHF_3/O_2 fluorine-based diamond etch fabrication results.....	56
5.2.2 Field emission characterization.....	57
5.2.3 Study summary	68
5.3 Demonstration of using EBL to fabricate lateral diode	60
5.3.1 Fabrication results.....	60
5.3.2 Field emission characterization	61
5.3.3 Study summary	61
5.4 The effect of 350 nm, 3- and 12- emitter tip density on V_{TO}	63
5.4.1 Fabrication results.....	63
5.4.2 Device characterization and analysis	67

5.4.3 Discussion	68
5.4.4 Study Summary	70
5.5 Sub-micron gap field emission performance as a function of gap.....	71
5.5.1 Fabrication of variable gap lateral diodes	71
5.5.2 Conditioning process for the lateral diodes	72
5.5.3 Field emission characterization	73
5.5.4 Study summary	89
6 CONCLUSIONS AND RECOMMENDATIONS.....	80
6.1 Conclusions of nanodiamond film study	80
6.2 EBL approach used to achieve sub-micron emission gap	82
6.3 Field emission performance summary of lateral diodes	83
6.4 Recommendations for future work	84
LIST OF PUBLICATIONS	85
REFERENCES.....	96
APPENDIX.....	92

LIST OF FIGURES

Figure 1.1. Nanodiamond film sample.....	5
Figure 2.1. Illustration of Schottky barrier lowering.	12
Figure 2.2. The energy band diagram for MIM microstructure model.....	16
Figure 3.1. A snapshot of CH ₄ /H ₂ /N ₂ microwave plasma during nanodiamond deposition.....	19
Figure 3.2. Nanodiamond film configurations reported by a) Joseph al [57]; b) Subramanian [6]; c) May et al. [26]; and d) Barbosa et al. [58]	22
Figure 3.3. Example configurations of CVD diamond films that were synthesized in effort to identify the best configuration for subsequent device patterning	23
Figure 3.4. Visualization of sp ² -enhanced nanodiamond film conduction models proposed by a) Tuck et al.[63]; b) Forbes et al. [44]; and c) Toyama et al. [65]....	24
Figure 3.5. Field emission test circuit for diamond films	27
Figure 3.6. Nanodiamond thin film Samples A, B, and C viewed at 30 k \times . When comparing the low growth rate films, a) and c), the grain boundaries become more well-defined when nitrogen is used in the reactant gas	27
Figure 3.7. a) C 1s of <i>Sample A</i> , a non-nitrogenated, low growth rate film. b) C 1s of <i>Sample B</i> , a high-pressure high-power growth rate film with N ₂ reactant gas used. c) C 1s of <i>Sample C</i> , a nitrogenated, low-pressure low-power growth rate film.....	29
Figure 3.8. Three-film <i>I-E</i> and Fowler-Nordheim characteristics	33
Figure 3.9. SEM of nanodiamond films showing the effect of surface preparation and growth rates. BEN prepares the sample surface for a high volume of grain boundaries and as the growth rate is increased, the grain sizes get larger	36
Figure 3.10. Raman spectra of the CVD diamond films.....	38
Figure 3.11. Corresponding current emission and F-N behavior of the films presented in this study.....	39

Figure 4.1. Lateral field emission diode operation43

Figure 4.2. A snapshot showing the EBL chamber.....45

Figure 4.3. The lateral diode is designed to have a) 2 mm × 2 mm contact pads and a 20µm × 100µm device area. The top-down material configuration consists of b) 1µm nanodiamond, 2µm silicon, 4µm oxide, and 525µm Si46

Figure 4.4. a) Cross section of substrate configuration used for lateral device fabrication. b) Higher magnification of the top 4 layers of the substrate. As shown, the PMMA and aluminum are 500 nm, ND is 1µm thick, and the active Si layer is 2µm.....46

Figure 4.5. Diagram of the vacuum field emission test set-up for the nanodiamond lateral diode.....47

Figure 4.6 Field emission characterization setup.....47

Figure 5.1. SEM micrographs of four different trials of lateral field emitter structures with insufficient aluminum mask thickness to withstand the duration of ND RIE. As a result of the incomplete ND etch, all devices shown were shorted and further processing could not be completed.....50

Figure 5.2. SEM micrographs a) - d) show the interface incompatibility between Cr mask and diamond surface. Images e) – l) show planar views of mask peeling as a result of poor adhesion.....51

Figure 5.3. SEM cross sections of PMMA, aluminum, and diamond adhesion51

Figure 5.4. High and low magnification image pairs of lateral devices where insufficient (10kV) accelerating voltage was used for EBL writing. As a result of the shallow bore-through voltage, the anode and cathode structures are not distinctly defined Images a) – h) show planar views of the effect of the insufficient e-beam accelerating voltage53

Figure 5.5. SEM images showing the effect of increasing dosage (1.0 to 1.5 of 105 µC/cm²) on a closely packed multi-emitter lateral field emission structure. The dosage increases from a low dose in image a) with the highest dosage in image f). It is clear that as the dosage increases, the area in between the emitters are cleared, however the emission gap also gets progressively larger54

Figure 5.6. SEM images showing the effect of developing time. Images a) is a 4-emitter lateral structure where the developing time was not sufficient, resulting in a shorted device. Images b) to e) are 30 k× SEM of each emitter showing the short. Image f) is a four-emitter lateral structure where the developing time was sufficient to create an opening in the anode-cathode structure. Images g) to j) are

30 k \times images showing the delineation of each emitter, on average of 1 μ m	55
Figure 5.7. Process flow for the mixed lithography lateral device fabrication process	57
Figure 5.8. SEM image pairs of a 12-emitter, images a) through b), and a 4-emitter tip lateral field emission device, images c) through d), both with a 1.2 μ m emission gap. The shading effect surrounding the cathode area is indicative of successful silicon etching to isolate the nanodiamond structure from the silicon support layer. Image e) shows the webbing of the polymer by-product.....	58
Figure 5.9. <i>I-E</i> characteristics of a 12-emitter and 4-emitter lateral device where diamond etch was performed using an 8:1 ratio of CHF ₃ and O ₂ gas	59
Figure 5.10. Background: SEM of diode structure with 2 mm contact pads. The left inset is an optical image of the diode during the nanodiamond etch process. The right inset is the final device delineation showing a 1.8 μ m cathode-anode distance product.....	62
Figure 5.11. <i>I-V</i> plot of the 10-finger lateral diode with ~1.8 μ m anode-cathode spacing. The inset shows the negative-sloped linear F-N plot	63
Figure 5.12. Current stability over time collected in 1 second intervals	63
Figure 5.13. Process flow for the single step EBL lateral field fabrication process	65
Figure 5.14. Optical and SEM images of the 12-emitter device showing the progression through the series of material removal for device definition	66
Figure 5.15. a) Uniform delineation of a 350 nm emission gap, 12-emitter lateral vacuum FED; b) side view of the lateral diode showing the Si undercut; c) higher magnification showing the uniformity of the cathode tips; d) side view showing columnar structure of the diamond film; e) and f) the estimated emitter tip radius is ~150 nm	67
Figure 5.16. a) Uniform delineation of a <350 nm emission gap, 3-emitter lateral vacuum FED; b) side view of the lateral diode showing the Si undercut; c) and d) higher magnification showing the uniformity of the cathode tips; e) and f) the emitter tip radius is ~150 nm	68
Figure 5.17. a) Current-voltage results for the 350 nm gap, 3- and 12-emitter sub-micron lateral diodes.....	69
Figure 5.18. Corresponding F-N plot.....	70

Figure 5.19. a) SCLC conformance indicates space charge build up at emitter tip; b) Concurrent Frenkel-Poole conduction indicates electron “hopping” from the proposed structural changes in the oxide surface and c) field-enhanced thermionic emission would indicate a lowered potential barrier to vacuum.....72

Figure 5.20. SEM images of the 3- and 12- emitter devices after testing show damage to oxide and emitter tips72

Figure 5.21. SEM of a) 500 nm; b) 850 nm, and c) 1.5 μm gap devices.....74

Figure 5.22. Various side views of the device delineation with oxide removal. The SEM in d) highlights the deliberate oxide removal74

Figure 5.23. a) Complete *I-V* for the three devices; b) Corresponding *I-E* characteristics.....76

Figure 5.24. a) Low voltage *I-V* for the three diodes with different emitter gap configurations77

Figure 5.25. *I-E* characteristics and corresponding F-N behavior of the lateral vacuum diodes are shown in a) and b). Figure a) shows the *I-E* for $E < 20 \text{ V}/\mu\text{m}$ and the corresponding F-N conformance is presented in b)..78

Figure 5.26. a) Full *F-N* characterization of the three devices. The deviation from F-N at $E > 20\text{V}/\mu\text{m}$ seen by the 500 nm and 850 nm gap devices are more clearly seen in b) and c)78

Figure 5.27. Both the 500 nm and 850 nm gap devices show conformance to FTE and SCLC at $E > 20 \text{ V}/\mu\text{m}$80

Figure 5.28. Current as a function of lateral emission gap at a constant voltage. As the voltage rises higher, the trend becomes more exponential due to the overcalling conduction mechanisms81

LIST OF TABLES

Table 2.1. Summary of conduction mechanisms encountered in this work.....	17
Table 3.1 Summary of kinetic energy (KE) of electrons for each bonding configuration from Figure 3-5. C1 and C2 are the sp^2 and sp^3 bonding types, respectively. Higher kinetic energy corresponds to a lower binding energy	31
Table 3.2 Binding energy (BE) and bonding contributions to C 1s. C1 and C2 are the sp^2 and sp^3 bonding types, respectively. The percent area contribution is also shown in addition to the bonding configuration	31
Table 3.3 Recipe summary for Samples A-E.....	36
Table 3.4 Summary of Raman peak assignments and sp^2/sp^3 ratio of all film spectra	38
Table A.1 Summary of β factors for 1.5 μm , 850 nm, and 500 nm gap lateral diodes	96

ABBREVIATIONS

Al	Aluminum
AOE	Advanced oxide etch
Ar	Argon
BEN	Bias enhanced nucleation
CH ₄ /H ₂ /N ₂	methane/hydrogen/nitrogen
CHF ₃	Trifluoromethane
Cr	Chromium
CVD	Chemical vapor deposition
EBL	Electron beam lithography
FED	Field emission device
FIB	Focused ion beam
F-N	Fowler-Nordheim
FWHM	Full width half maximum
GaN	Gallium Nitride
ICP	Inductively coupled plasma
I-E	Current-electric field
IPA	Isopropyl alcohol
I-V	Current-voltage
Li	Lithium
LOCOS	Local oxidation of silicon
MIBK	Methyl-isobutyl ketone
ND	Nanodiamond
OEB	Optical and electron beam lithography
P	Phosphorus
PMMA	Poly methyl methacrylate
RIE	reactive ion etching
SBL	Schottky Barrier Lowering
SCLC	Space Charge Limiting Current
SEM	Scanning electron microscopy
Si	Silicon
SIMOX	Separation by implantation of oxygen
SOI	Silicon -on-insulator
SBL	Schottky Barrier Lowering
VFED	Vacuum field emission device
VTE	Vacuum thermal electric
XPS	X-Ray photoemission spectroscopy

CHAPTER I

INTRODUCTION

This first chapter introduces the motivation for this research. An overview of vacuum field emission is provided followed by the need for nanodiamond as a cold field emission material and the premise for the sub-micron gap, lateral emitter field emission diode device configuration. Last are the research objectives and chapter summaries of this dissertation.

1.1 Overview of vacuum field emission research

Electron sources are increasingly important for device technology and scientific research tools. Applications include flat panel displays, television monitors, electron beam microscopy, and electron beam lithography. However, the trend towards vacuum device miniaturization has prompted research on alternative electron sources which are smaller and more efficient. For the past two decades, the core research of vacuum microelectronics has been focused on efficient cold cathode materials with a low turn-on field [1-5] and subsequently a low turn-on voltage with stable emission current maintained at practical vacuum levels [6]. With turn-on voltage being limited by the properties of the emitter material and the processes that are used to fabricate the field emission devices [7], cathodes derived from diamond would offer the potential for low-power operation that would be necessary for more densely packed vacuum field emitter arrays.

Vacuum field emission is the phenomenon by which electrons are emitted from the surface of a condensed material under applied electric field. In comparison to solid-state devices, vacuum microelectronics has the potential for higher operational limits [8] due to

ballistic electron transport [9-11] as opposed to transport through a solid medium. The electron transport through a crystal lattice, in solid state devices, would also place limits on device scaling and switching speed. In 1961 Kenneth Shoulders originated the design of micron-sized vacuum field emission devices and envisioned applications that were later carried out from 1968 by Capp Spindt [12-13], who proceeded to develop field emission technology. The original bulky and fragile vacuum tubes were deemed outdated upon the development of solid-state transistors in the 1940s and integrated circuits in the 1960s [14-16]. However, with the new generation of micron-sized vacuum microelectronics, the interest in vacuum tube technology became renewed.

Metal and silicon-based field emission device technology are well developed and widely studied. However both configurations have limited potential applications as field emission devices due to high work function properties and sensitivity to impurity adsorption. Metal-based emitter designs would require complicated fabrication processes since the technology for producing sharp metal emitters is limited [5]. Silicon-based emitters have shown improvement over metal cathodes, demonstrating low operating voltages [17-18]; Han et al. reported 5 nA at a 13 V turn-on voltage using a ~40 nm emission gap lateral device [17]. However, characterized by a 4.05 eV electron affinity, low thermal conductivity, and low breakdown field properties, in addition to high 10^{-10} - 10^{-11} Torr vacuum requirements, Si-based field emission devices are inhibited from practical operating conditions [6].

Gallium nitride (GaN) is a wide band gap (3.4 eV) [19] material that has also attracted attention due to its material hardness and chemical inertness [20], however the material does not possess the low electron affinity property that is characteristic of diamond [19]. Underwood et al. reported a threshold voltage that varied between 400V and 700V for a GaN field emitter array with an integrated anode spacing of 0.1 mm [20].

Therefore, diamond as a cathode material offers the potential to significantly improve the performance of vacuum field emission devices (VFEDs). Advancements can be made in two key areas: (1) the capture of a low-work function diamond material in a smooth, thin-film form and (2) the design and fabrication of an emitter structure that would permit sub-volt turn-on and low operating voltage. By employing field-enhancing nano-structures to attain conductive, low effective work function nanodiamond films in addition to the fabrication of lateral diode devices with sub-micron anode-cathode spacing, both criteria can be met.

1.2 Introduction to nanodiamond as a cathode material

Carbon can exist in different forms, making it unique and versatile. Diamond possesses notable qualities such as high hardness, thermal conductivity, chemical inertness, and a wide band gap. On the other hand, graphite is considered a metal, characterized by a zero band gap [22]. Of particular interest to the dissertation topic is the control of graphite in diamond, obtained through nitrogen-incorporated nanodiamond via MPECVD. However, for electron emission to occur there must be a continuous supply of electrons and a sustainable transport mechanism for electrons to reach the surface. The role of doping to enhance the supply of electrons and the role of sp^2 in electron emission is discussed in sections 1.2.1 and 1.2.2.

1.2.1 Field emission enhancement by doping

Low positive or negative electron affinity property of diamond is believed by many researchers to be responsible for observed low field emission from diamond because a small electron affinity would allow electrons from the conduction band to emit into vacuum easily with

low applied electric field. However, the supply of electrons in the conduction band of diamond is limited due to wide band gap material properties [6].

In theory, the low electron affinity of diamond coupled with the incorporation of n-type donor impurities would require a very small electric field to induce electron emission. However in practice, in spite of reported successful diamond film doping with nitrogen (N) and phosphorous (P) [23-24], substitutional doping is not easy due to the tight lattice structure of diamond [6]. Regardless, of primary interest is the increased sp^2 content as a result of introducing impurities. P-type doping has also been explored; Geis et al. reported electron emission from boron-doped diamond using 20-50 V/ μm while nitrogen-doped type Ib diamond required only 0-1 V/ μm [25-26]. Building upon previous work, nitrogen-incorporated nanodiamond will continue to be employed as the underlying emitter material for subsequent lateral device fabrication.

1.2.2 Role of sp^2

Improved electron field emission characteristics that are exhibited by nitrogen incorporated nanodiamond films are not necessarily a result of substitutional doping, but rather by the creation of defects, such as graphite components and grain boundaries, that result from using nitrogen during film growth [5, 27-28]. As nitrogen is preferentially incorporated into diamond at the grain boundaries, new electronic states associated with carbon and nitrogen can be produced at and above the Fermi level [5-6, 29]. The incorporation of nitrogen leads to the overlap of sp^2 clusters, thereby enhancing the connectivity between graphite-induced conduction paths and emitter surface regions. The reported effective work function for nitrogen-incorporated nanodiamond film is ~ 0.5 eV and less [30-31]. In addition to increased sp^2 -carbon

bonding content and n-type electrical conductivity, nitrogen-incorporated nanodiamond films have a smooth morphology [6 and 32], a property that is important for patterning nanometer-sized dimensions. The sample shown in Figure 1.1 is a nitrogen-incorporated nanodiamond film that was fabricated using Vanderbilt University's microwave, plasma-enhanced chemical vapor deposition (MPECVD) system.

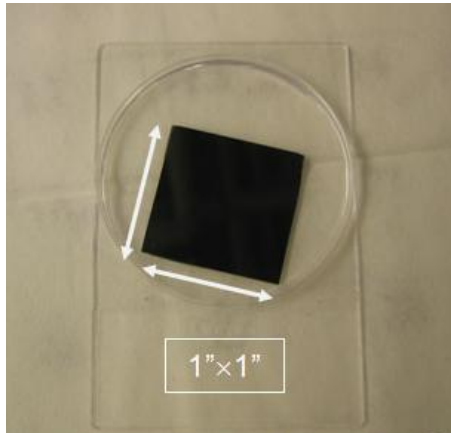


Figure 1.1. Diamond sample grown using microwave-enhanced CVD system.

Apart from the desirable chemical, mechanical, and thermal properties of conventional CVD microcrystalline diamond films, nanodiamond film configurations possess a higher volume density of grain boundaries for aiding electron emission at room temperature and smooth morphology for patterning nano-scale designs. The ability to control and reproduce field enhancing properties of nanodiamond elevates the utility of diamond for vacuum nanoelectronic device applications [6].

1.3 Advantages of lateral configuration vacuum field emission devices

One of the major challenges in vacuum electronics is the development of emitter arrays that would deliver uniform emission current over a large area. The lateral configuration constitutes a versatile array construct comprising of integrated anode and cathode electrodes to

form a complete device. The lateral configuration reduces the processing complexity and furthermore the electrodes may be placed at closer distances [6, 33]. Precise lithographically-controlled micron and sub-micron inter-electrode spacing would enable a significant reduction in device operating voltages, further enhancing the practicality of the lateral device. Lateral devices employing nanodiamond as the emitter material would achieve operability at extremely low turn-on fields and voltages. In this research we have successfully developed a process for achieving sub-micron anode-cathode emission gap scaling using nanodiamond.

1.4. Objectives of this research

The objectives of this research were to understand the underlying control parameters of nanodiamond films and to derive sub-micron-gap lateral field emission devices in diode configuration from nanodiamond films that have been optimized for design and fabrication. The sub-micron gap delineation should demonstrate a sub-volt turn-on and be operable at low electric fields. This research encompasses the following milestones:

- Develop a CVD process for depositing nanodiamond films;
- Study and optimize nanodiamond films for enhanced electron field emission;
- Use EBL to design nanodiamond field emission diodes in lateral configuration for sub-volt turn-on;
- Develop a repeatable diamond patterning process for obtaining sub-micron gap delineation for various cathode configurations;
- Characterize and analyze the field emission performance of nanodiamond films and derived lateral emitter diodes.

1.5. Organization of this dissertation:

There are six chapters in this dissertation and they are organized as follows:

- *Chapter I* provides background information on vacuum field emission applications and describes the motivation for using nanodiamond as a cathode material for fabricating sub-volt turn-on, sub-micron gap lateral field emission diodes.
- *Chapter II* incorporates the theoretical background of electron field emission with interface and bulk conduction mechanisms that are commonly encountered in vacuum electronics. This chapter also describes electron transport through a metal-insulator-metal structure.
- *Chapter III* introduces various types of diamond films, with particular emphasis on correlations between the field emission performance of each film with electron binding energy and sp^2/sp^3 content.
- *Chapter IV* describes the design and fabrication approach used in this research to achieve sub-micron emission gap for assorted cathode geometry.
- *Chapter V* analyzes the field emission performance of multiple nanodiamond lateral diode configurations as the emission gap was scaled to sub-micron dimensions.
- *Chapter VI* summarizes key findings from Chapter III and Chapter V and provides recommendations for further research to expand upon sub-micron gap nanodiamond lateral device technology.

CHAPTER II

OVERVIEW OF ELECTRON EMISSION MECHANISMS

In this chapter, the theoretical aspects of cold vacuum field emission and related conduction mechanisms are described. The importance of nano-structures for low field emission is also discussed.

2.1 Fundamental electron emission into vacuum

Electron field emission is the process of emitting electrons from a solid surface into vacuum under applied electric field. Electrons in a solid are bounded to core atoms by electrostatic force. The electrostatic force forms a potential barrier at the surface and is characterized by the work function (Φ). In order to extract electrons from a solid surface, energy must be applied to the solid in order for electrons to overcome the barrier and emit into vacuum [6]. Electron emission mechanisms that are of specific interest to this research are Fowler-Nordheim (F-N) electron tunneling and field-enhanced thermionic emission (FTE).

At low temperature, most electrons have total energy below Fermi level. A strong external electric field must be applied to thin down the potential barrier at the solid/vacuum interface for electrons to quantum-mechanically tunnel into vacuum [6]. This is called field emission because electric field is the main source of energy that induces electron emission.

In graphite-incorporated diamond films, low field emission may occur as a result of defects/impurities raising the Fermi level and thus reducing the tunneling barrier [6, 34]. Well-connected, graphite-induced conduction paths to emitter surface regions, as discussed in section

1.2, may permit field-enhanced thermionic emission at room temperature under moderate applied field.

2.1.1 Fowler-Nordheim tunneling

Fowler-Nordheim tunneling emission is a carrier transport process in which electrons tunnel through a diamond-vacuum energy barrier under applied electric field conditions. The Fowler-Nordheim emission current for an emitter array is given by [6]:

$$I = n \alpha \frac{1.54 \times 10^{-6} (\beta E)^2}{\phi} \exp \left(-6.83 \times 10^7 \frac{\phi^{\frac{3}{2}}}{\beta E} \right) \quad (2.1)$$

where n is the number of emitters in the array, α is the emitting area, and β is an enhancement factor comprising of contribution from emitter geometry (β_{geometry}) and sp^2 content (β_{sp^2}), as per prior research by Wisitsorattat [5]. The electric field E is given by:

$$E = V/d \quad (2.2)$$

where V is the anode-cathode voltage and d is the anode-cathode spacing. For a sharp microstructure, the electric field at the apex is

$$E = \beta V/d \quad (2.3)$$

where β is the factor by which the local electric field is increased due to a sharpened microstructure relative to the planar structure [5-6].

In order to extract measurable current from cold cathode materials, it is necessary to consider cathode designs with a high aspect ratio. Sharp emitter structures ensure that the maximum field is at the apex, making the determination of local fields and emission behavior more predictable. With the electric field of a sharp tip being strongest at the apex and reduced rapidly in regions further away from the apex, it can be deduced that most of emission current

arises from electron tunneling within the vicinity of the highest electric field region [6]. Conformance to Fowler-Nordheim may be analyzed using the experimental form of equation 2.1:

$$\ln\left(\frac{I}{E^2}\right) = \ln\left(\frac{n\alpha 1.54 \times 10^{-6} \beta^2}{\phi}\right) - 6.83 \times 10^7 \frac{\phi^{\frac{3}{2}}}{\beta E} \quad (2.4)$$

Therefore, by plotting the emission current in the form of $\ln(I/E^2)$ versus $1/E$, a straight line should be obtained with a slope proportional to $\phi^{3/2}/\beta$ and an intercept proportional to β^2/ϕ [6]. Materials that are characterized by a low work function, which manifests as a shallow, negative F-N slope, would typically permit higher emission current at a given applied electric field due to the closer proximity of the Fermi level to the conduction band.

2.1.2 Field-enhanced thermionic emission (Schottky barrier lowering)

One of the direct consequences of an image potential associated with a metal-insulator (e.g., sp²-sp³) or vacuum (e.g., semiconductor-vacuum) interface is Schottky barrier lowering (SBL) [35]. At moderate temperature, which may encompass internal heating as a result of current flow [36] in nanodiamond, some electrons may have total energy above the Fermi level but below the vacuum level [6]. In order for these electrons to emit into vacuum, only a moderate electric field must be applied to thin down the barrier [6].

The origin of SBL comes from the image potential that an electron experiences near a conducting surface. In addition to a narrowing effect in the presence of electric field, the barrier also becomes lowered due to the image potential. The force between two charges is well known:

$$F = \frac{q^2}{4\pi r^2} = \frac{q^2}{4\pi(2x)^2 \epsilon_0} \quad (2.1.5)$$

The potential energy is found by integrating the force, F , from x to infinity, resulting with:

$$V(x) = \frac{-q^2}{16\pi\epsilon_0 x} \quad (2.1.6)$$

where ϵ_0 is the vacuum permittivity (8.85×10^{-14} F cm⁻¹). Upon applying an external electric field:

$$V(x) = -qEx \quad (2.1.7)$$

The maximum potential of the sum of the mirror charge field and applied electric field can be obtained by taking the derivative [37]:

$$\phi' = \frac{d}{dx} \left[\frac{-q^2}{16\pi\epsilon_0 x} - qEx \right] = -q \left[\frac{qE}{4\pi\epsilon_0} \right]^{\frac{1}{2}} \quad (2.1.8)$$

Therefore under applied fields the surface potential barrier, ϕ_b , is effectively reduced to:

$$\phi_b = \phi - \phi' \quad (2.1.9)$$

The emission current associated with SBL, namely FTE, is given by:

$$J = A^{**} T^2 \exp \left(\frac{-q(\phi_b - \sqrt{qE_i / 4\pi\epsilon_i})}{kT} \right) \quad (2.1.10)$$

where A^{**} is the effective Richardson's constant, ϵ_i is the material permittivity, and kT/q is the thermal voltage [38]. FTE can be verified by plotting the square root of the electric field as abscissa (x-axis) and the natural log of $(J/A^{**}T^2)$ as the ordinate (y-axis); a positive-sloped straight line would indicate FTE [21, 39-41]. Figure 2.1 is an illustration of SBL.

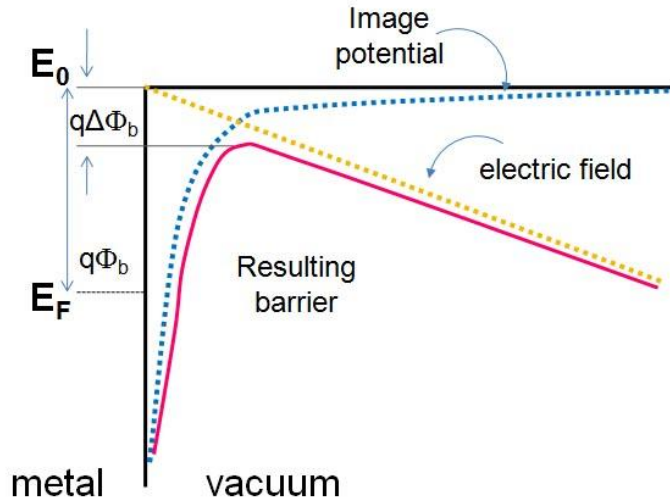


Figure 2.1. Illustration of Schottky barrier lowering. Adapted from [42].

2.2 Bulk electron conduction mechanisms

Electrical conduction through more resistive materials may experience space-charge effects [43], which restricts current emission. Electron transport through insulative bulk material is mainly controlled by structural defects or induced conduction paths that cause a leaky dielectric behavior [44]. In instances where a significant number of defect or impurity sites permit the formation of energy bands that are closely spaced, the Poole-Frenkel electron hopping mechanism could easily provide a steady flow of electrons to the surface and sustain a stable electron emission [6, 45-46].

2.2.1 Space Charge Limited Current

SCLC may occur in insulative or low mobility semiconductors [47]. SCLC is applicable to both oxide and the nanodiamond materials. Pertaining to oxide, charges invariably get trapped in parts of the oxide as current flows across the oxide. The trapped charges increase over time, forming high electric field and high current regions along the way. In the nanodiamond

structure, if the mobility is low then the charge injection will be limited by the rate at which the charge can be transported to the surface. The carriers that are emitted into vacuum form a space charge layer at the emitter tip; the potential due to this charge will repel any additional carriers [48]. The SCLC expression is described using:

$$J = \left(\frac{9\varepsilon_i \mu V^2}{8d^3} \right) \quad (2.1.11)$$

where ε_i the dielectric constant, μ is the charge carrier mobility, and d is thickness of the material [38 and 49].

2.2.2 Poole-Frenkel

Poole–Frenkel conduction is a bulk process associated with shallow defects or impurity sites within an insulator. The charge carriers residing on these defect sites are able to “hop” from one site to another if the sites are sufficiently close together [47]. However, if the defects sites are too far apart, the hopping mechanism can become space-charge limited [47 and 50]. The Poole-Frenkel current density, J , is given by:

$$J \propto E_i \exp \left(\frac{-q(\phi_b - \sqrt{qE_i / \pi\varepsilon_i})}{kT} \right) \quad (2.1.12)$$

where ϕ_b is the trap level barrier height, E_i is the electric field in the emitter material, and ε_i is the material permittivity [38].

2.3 Energy band diagram for diamond MIM structure

Assuming a diamond surface with small positive electron affinity, for electron emission to occur the electrons must first quantum-mechanically tunnel through the potential barrier at the

metal-diamond interface into the diamond. Electrons drift through the diamond bulk and overcome a small potential barrier at the diamond-vacuum interface. The Metal-Insulator-Metal (MIM) band diagram model used by Wisitsorat-at [5] and Subramanian [6] take into account the effect of sp^2 content in grain boundaries and structural field enhancement factors that are associated with nitrogen-incorporated nanodiamond films used in this work.

2.3.1 Electron emission based on graphite-in-diamond MIM model

Wisitsorat-at and Subramanian proposed that the conduction mechanism of diamond with graphitic particles involves the creation of conducting channels via hot electron emission process. Grain boundaries in diamond films have also been suggested to function as conduction channels [6]. Essentially, electrons can get into the conduction band through the channels and subsequently escape into the vacuum [5-6]. Wisitsorat-at indicates that there exist defect states located at the bottom of the conduction band that effectively raises the Fermi level and reduces the energy barrier to electron tunneling [5]. It was also offered that defects in diamond, namely vacancies, stacking faults, and grain boundaries, are probable sources that provide electrons for field emission enhancement [6]. Subramanian further asserts that defective or lower quality diamonds have better emission properties [6].

A model proposed by Wisitsorat-at [5] based on a series of cascaded MIM structures, which enhances the electric field inside the diamond film and thereby increases the field enhancement factor is illustrated in Figure 2.2. For electron emission from diamond to occur the electrons must:

- 1) *Tunnel through the potential barrier at the metal-diamond interface.* Electron tunneling at the metal-interface depends on the barrier height which varies with the type of metal contact.

2) *Be transported through the diamond bulk.* Conduction through the diamond layer is primarily determined by the diamond's sp^2/sp^3 composition. The graphite sp^2 particle is represented by an energy level equivalent to a metal contact but with a very small dimension [5]. The sp^2 introduces a potential between itself and the metal contact, $\Delta V' \approx (1/Ks)(\Delta d/V)$, where V is the anode-cathode voltage, d is the inter-electrode distance, $\Delta d'$ is the separation between the floating conducting particle and the metal-diamond interface, W' is the tunneling distance, and Ks is the diamond dielectric constant [5].

3) *Tunnel through the diamond-vacuum interface.* The portion of electrons that can tunnel through the successive sp^2 - sp^3 structure potential barrier will be accelerated toward the vacuum interface. The geometry of the diamond cathode emitter geometry controls the electric field and the tunneling probability through the diamond-vacuum interface. It is customary to design cathode emitter tips with a high-aspect ratio.

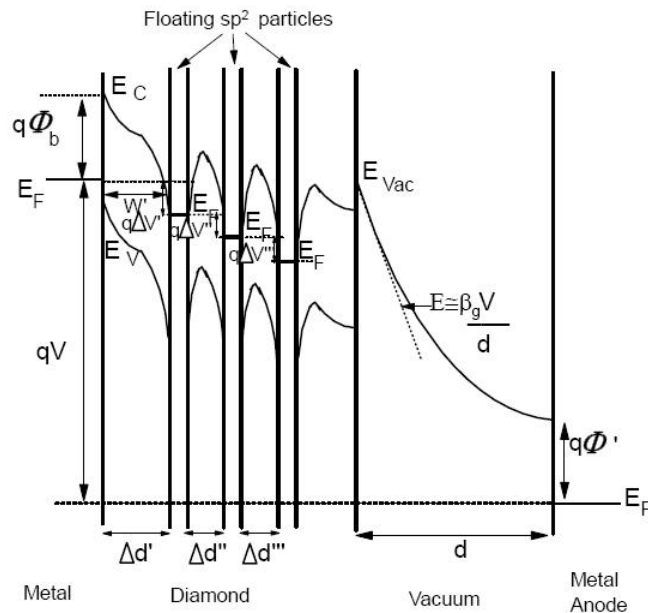


Figure 2.2. The energy band diagram for MIM microstructure model. Adapted from [5, 25, and 48].

While Fowler-Nordheim tunneling behavior in nanodiamond films and derived devices has been reported, it will be seen in Chapter V that FTE may arise as the distance between the anode and cathode is scaled into the sub-micron range. Similarly, structural surface changes as a result of processing technology such as RIE, provides opportunities for Frenkel-Poole defect-induced electron emission.

2.4 Summary of conduction models applicable to nanodiamond

A non-F-N model for electron emission from a diamond surface that is within the scope of this work is FTE as a result of Schottky Barrier Lowering (SBL) and low effective work function materials. Additionally, the structural alterations due to processing technology permit Frenkel-Poole to become evident. Table 2.1 is a summary of the respective current density expressions for the conduction mechanisms.

Conduction Mechanism	Expression
Field-enhanced Thermionic Emission	$J = A^{**} T^2 \exp\left(\frac{-q(\phi_b - \sqrt{qE_i / 4\pi\epsilon_i})}{kT}\right)$
Space Charge Limited Current (SCLC)	$J = \left(\frac{9\epsilon_i \mu V^2}{8d^3}\right)$
Frenkel-Poole	$J \propto E_i \exp\left(\frac{-q(\phi_b - \sqrt{qE_i / \pi\epsilon_i})}{kT}\right)$

Table 2.1. Summary of conduction mechanisms encountered in this research and their expected dependencies. Adapted from [38].

CHAPTER III

FABRICATION AND CHARACTERIZATION OF NANOCRYSTALLINE DIAMOND

This chapter explores nanodiamond film as a cold cathode emitter material by reviewing macroscopic electron field emission behavior and correlating the results with X-ray photoelectron (XPS) and Raman spectroscopy results. Several configurations of diamond film exist; representative growth methods and conditions are compared and reported in this chapter. Of particular interest is the nitrogen-incorporated nanodiamond film configuration due to the reduced threshold field that is attributed to enhanced conductivity, based on the MIM model that was described in Chapter II. For comparison, the chemical and electrical properties of conductive nanodiamond films will be compared to more insulative films that were synthesized using $\text{CH}_4/\text{H}_2/\text{N}_2$ and CH_4/H_2 reactant gas mixtures, respectively.

3.1 Diamond Deposition Techniques

Chemical vapor deposition refers to a gas-phase chemical reaction that occurs above a solid substrate, thereby resulting in a film deposition that occurs on top of the sample substrate. Figure 3.1 shows a picture of the active RF plasma during nanodiamond film growth. Plasma-enhanced CVD was used to synthesize all diamond films that are reported in this research. The primary surface pre-treatment method used for preparing the substrate surface for diamond growth was mechanical abrasion to create nucleation sites. Diamond nucleation on non-diamond surfaces without pre-treatment is usually very difficult and slow.



Figure 3.1. A snapshot of $\text{CH}_4/\text{H}_2/\text{N}_2$ microwave plasma during nanodiamond deposition.

By adjusting the plasma conditions, CVD diamond can possess grain sizes ranging from a few nanometers to several microns. The grain size, along with other characteristics, namely the sp^2/sp^3 (graphite/diamond) content, strongly depends on growth conditions. It has been shown that low pressure and low power conditions result in nano-crystalline diamond while high pressure and high power conditions yield larger-grained structures [6, 51-56].

3.1.1 Reported work on the effect of growth conditions on diamond surface morphology

Diamond film nucleation is highly sensitive to the seeding sites created by surface abrasion while the surface morphology may vary widely with changes in reactant gas mixtures, chamber pressure and power, and substrate temperature. Joseph et al. and Subramanian [6, 57] reported on the influence of CH_4/H_2 in addition to power and pressure parameters on nano-crystalline and ultra-nanocrystalline diamond morphology while May et al. [26] reported on the effect of surface abrasion and CH_4/H_2 content on grain size. The effect of substrate temperature was investigated by Barbosa et al. [58], showing that an increase in substrate temperature will result in decreasingly smaller diamond crystallites.

May et. al reported on achieving different types of nanodiamond surface morphology, distinguishing between multi-faceted and amorphously defined grains. The substrate preparation techniques varied between mechanical polishing with diamond grit, ultrasonic agitation, and ion bombardment to create nucleation sites. The crystalline surface morphology was described as being faceted, possessing diamond grains as large as 100-500 nm. In order to attain the 20-100 nm cauliflower-like nanodiamond, the methane concentration was increased from 1% to 5%. The chamber pressure and substrate temperature were kept constant at 20 Torr and 900°C, respectively [26].

In his *Ph.D. Dissertation*, Subramanian [6] showed that nanodiamond can be obtained by increasing the nucleation rate and decreasing the growth rate by adjusting the microwave power, reactant pressure, and gas flow rate. Lowering the microwave power reduces the energy of the plasma whereby decreasing the reactant pressure spreads out the plasma in the CVD growth chamber. Reducing the methane decreases the carbon growth source, effectively slowing the growth rate. As a result of reducing the growth rate, diamond nucleation and growth compete against each other for the limited amount of energy that is available, resulting in an increased nucleation density and diminished grain size. Subramanian further observed that the grain sizes in nitrogen-incorporated diamond films decreased as the degree of sp^2 bonded carbon content in the film increased [17, 59].

Joseph et al. [57] reported on using CH_4/Ar plasma to produce nanodiamond at a relatively lower 400°C substrate temperature due to the low activation energy requirement for disassociating CH_4 to form sp^3 -bonded carbon. For comparison, when using CH_4/H_2 -based plasma, the substrate temperature requirement would be in the 800°C range since the methyl group must overcome a larger activation energy to form diamond nuclei. It can be shown that

diamond film growth is thermally activated; with increasing substrate temperature the growth rate also increased. Barbosa et al. [58] showed that the activation energy for fine grained material with a high sp^2/sp^3 carbon ratio is low compared to that of micro-crystalline diamond structures. With increasing substrate temperature, the sp^2/sp^3 carbon ratio increased while the diamond grain size decreased. Therefore, a smooth, conductive film can be obtained using increasingly higher substrate temperature during the film growth process.

Figure 3.2 portrays the different nanodiamond films achieved by the referenced authors. An increased density of grain boundaries in nanodiamond, in comparison to fast growth rate microcrystalline diamond, exhibits less abrupt features and would exhibit an increase in electrical conductivity due to the presence of more “channels” for electron transport through the diamond film [60]. Incorporating past observations on the effect of substrate abrasion, plasma parameters, gas mixture constituents, and reactant gas ratios on obtaining nanodiamond film, section 3.2 presents new results from identifying the optimal nanodiamond film configuration for subsequent sub-micron lateral device fabrication.

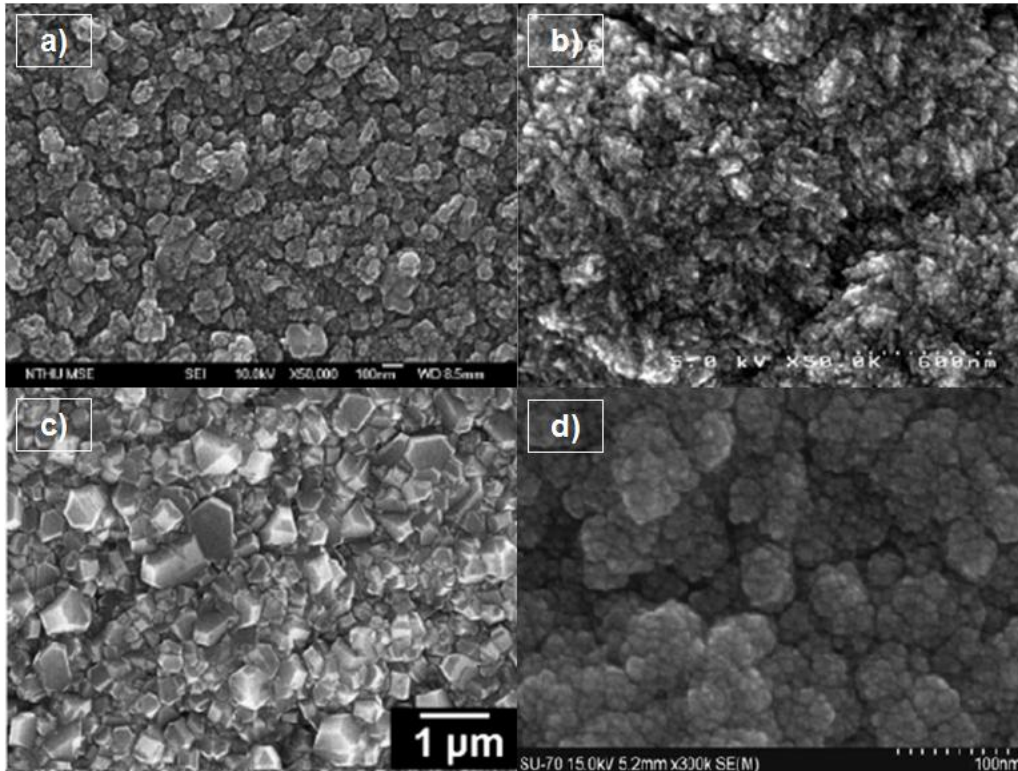


Figure 3.2. Nanodiamond film configurations reported by a) Joseph et al [57]; b) Subramanian [6]; c) May et al. [26]; and d) Barbosa et al. [58].

3.2 Macroscopic electron emission from diamond films

Figure 3.3 shows an extensive set of CVD diamond films that was fabricated in order to identify a smooth, conductive nanodiamond film for sub-micron gap lateral VFED patterning. In this work, grain sizes as small as ~5-10 nm were obtained without any external polishing. Several films from this set were down-selected for further study of electron field emission properties. The results are presented in sections 3.4 and 3.5.

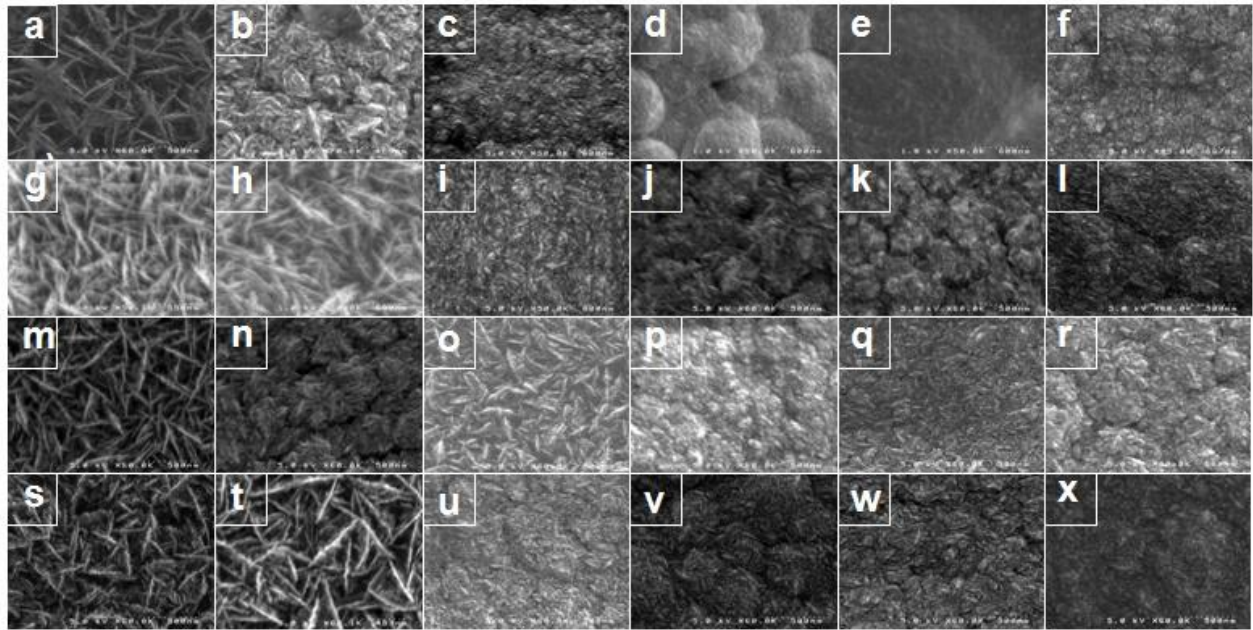


Figure 3.3. Example configurations of CVD diamond films that were synthesized in effort to identify the best configuration for subsequent device patterning.

Nanodiamond films can behave as macroscopic electron field emitters, being able to generate electrons when subjected to $2.2 \text{ V}/\mu\text{m} - 3.3 \text{ V}/\mu\text{m}$ [6, 44, 61, and 62]. The emission occurs because the films are comprised of electrically heterogeneous nano-structures, forming conducting channels that connect surface regions. It is proposed that these channels form paths to emitting features that are near or on the film/vacuum surface. Several conduction models are surveyed in section 3.3.1 to better understand the behavior of electron transport in nanodiamond. Analysis of the nanodiamond film emission suggests that emission is primarily due to geometrical field enhancement arising from the conducting nanostructures.

3.2.1 Proposed hybrid models illustrating low macroscopic field emission mechanism

Electron emission mechanism is aided by conductive particles embedded in an insulating matrix, as described in our previous research [5-6]. Similar models have also been proposed by

other research groups [44, 63-64]. There are several suggested nanostructure configurations that may be used to illustrate actively field emitting films. It can be agreed from the collective research that field emission occurs as a result geometrical enhancement from conducting nanostructures that are either inside the film or near the film/vacuum interface [44]. It is helpful to visualize the referenced mechanisms by applying the proposed principles to a cross section of one of our diamond films, as shown in Figure 3.4. Figure 3.4 a) portrays the proposed structure by Tuck et al. consisting of conducting inclusions deliberately dispersed in the field emitting dielectric material, forming channels with sharp end tips protruding into the vacuum [63]. Figure 3.4 b) represents the hypothetical channel formation through a high density of conductive clusters that are embedded in a smooth film (only representative clusters are shown for clarity) [44 and 64]. Figure 3.4 c) is a cross-sectional representation of a carrier transport model portraying the belief that grain boundaries composed of non-diamond phases are the primary electron emission sites [65].

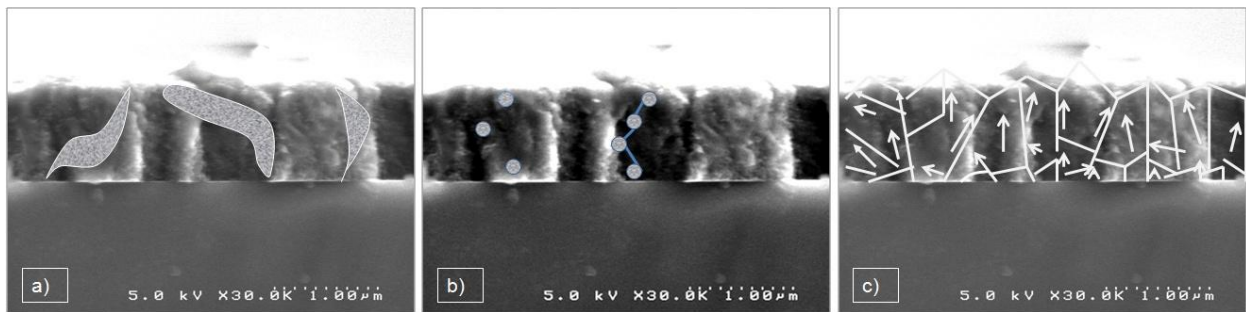


Figure 3.4. Visualization of sp^2 -enhanced nanodiamond film conduction models proposed by a) Tuck et al. [63]; b) Forbes et al. [44]; and c) Toyama et al. [65].

The underlying principles of the proposed models resemble Wisitsorath's proposed MIM [5] or hot electron transport mechanism [1, 6, 66-67]; graphitic sp^2 is responsible for forming conducting channels throughout the diamond film. While enhanced local field strength would

enable low field electron emission or field-assisted thermionic emission to occur, sufficiently high external electric field would allow electrons from lower energy levels to tunnel into the vacuum and contribute to emission [68]. Different research groups [5-6, 69-70] have attributed low field electron emission to defects, which in this research may encompass leakage from oxide, a commonly used material for structural support. Deviation from F-N behavior is further discussed in Chapter V.

To investigate the belief that field emission current is controlled by carrier transport in the diamond and corresponding electron emission from the film surface to the vacuum, the original work reported in this chapter examines the effect of graphite-to-diamond content (sp^2/sp^3) and the corresponding morphology on field emission performance. The content of the diamond films were monitored using X-ray photoelectron and Micro-Raman spectroscopy and the surface morphology features were captured using a Hitachi S-4200® scanning electron microscopy (SEM). Through correlating the control parameters that were used to create the individual film configurations with changes in turn-on field, the nanodiamond film growth process becomes more predictable.

3.3 Tools for monitoring electronic changes in nanodiamond content

a) XPS:

XPS provides information on the elemental composition and the oxidation state of film samples and moreover identifies the types of carbon, nitrogen, and oxygen groups that present in the films. The samples were excited using $MgK\alpha$ (1253.6 eV) photon energy X-rays. The binding energy E_{binding} is the difference of the electron kinetic energy, E_{kinetic} , and the work function of

the spectrometer, $\Phi_{spectrometer}$, from the photon energy of the X-ray, E_{photon} . The binding energy is distinctly characteristic of the atom and orbital from which the electron is emitted [71].

$$E_{binding} = E_{photon} - E_{kinetic} - \Phi_{spectrometer}, \quad (3.1)$$

b) Raman spectroscopy:

Micro-Raman spectroscopy can be used to capture the differences in electronic and structural features across different film configurations. Using a commercial Raman micro spectrometer (LabRam, Jobin-Yvon), the measurements were executed using a grating of 1800 grooves/mm and a He-Ne laser (632.8 nm) at 11 mW. The laser-optical Raman technique differentiates with great precision the atomic binding states of sp^2 (graphite) and sp^3 (diamond) from other non-diamond forms.

Relatively low levels of nitrogen incorporation (a 1:9 ratio to methane) in densely packed grain boundaries may cause a diamond film to consequently lose diamond-like characteristics. Using a wavenumber scan from 1000 to 1700 cm^{-1} , ND films would typically exhibit two to three main peaks corresponding with different diamond and graphite phases. A disorder peak would not be present in single crystalline graphite since it is characteristic of fine graphite only [72], e.g. the periodicity of long-range order is more easily lost. A diamond peak near 1170 cm^{-1} is indicative of nanocrystalline diamond [6]; Filik and Pfeiffer [72-73] suggest the indication of shallow donors from surface states. Only a low level of nitrogen was needed in order to induce graphitic, metallic behavior from the CVD diamond films.

3.3.1 Field emission test set-up for CVD diamond films

The electron field emission characteristics of the CVD diamond films reported in this work were obtained by using a vertical diode configuration devised of a parallel plate test set-up involving an external n^{++} silicon anode ($\rho=0.002\text{-}0.008 \text{ }\Omega\text{-cm}$) and alumina spacers. The test schematic is shown in Figure 3.5.

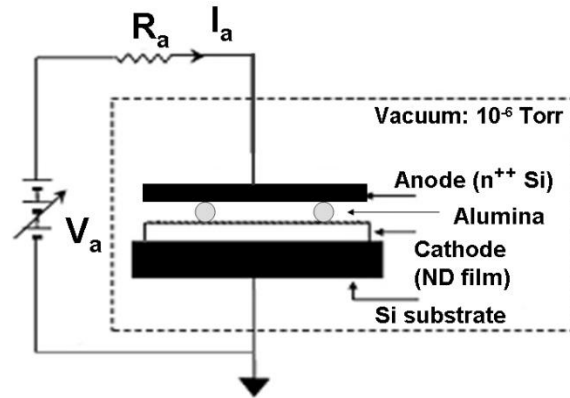


Figure 3.5. Field emission test circuit for diamond films. Adapted from [6].

The emission testing was performed at room temperature and in a vacuum environment of 10^{-6} Torr. The emission current from the as-deposited CVD diamond films was measured as a function of applied voltage. The emission characteristics can be obtained from the emission current and anode voltage. The electric field is simply the anode voltage per anode-to-cathode distance. In this configuration the anode-to-cathode spacing, or inter-electrode distance, is the diameter of the alumina spacers. The F-N scale can be derived as described in Chapter II.

3.4. The study of sp^2 and sp^3 hybridized bonding and corresponding electron field emission characteristics of nanodiamond films

In order to investigate enhanced field emission behavior attributed to carbon bonding hybridizations, three distinct ND films exhibiting differentiable grain structures and carbon

chemical bonding content were fabricated using CVD under different growth conditions. Two of the three films were deposited under low-pressure and low-power conditions while the third film was deposited using high reactant pressure and high microwave power conditions. The ND film surfaces were imaged using SEM at 30 k \times magnification. Sample A “LPLP-noN₂” and Sample C “LPLP-N₂” consist of nanodiamond clusters characterized by individual grain sizes measuring approximately ~10-20 nm as determined by SEM scale markers, see Figures 3.6 a) and 3.6 c). The morphology of Sample C resembles that of the non-nitrogenated Sample A, with the exception that the grain boundaries appear much coarser, potentially yielding sharper emission sites favorable to electron field emission. The high-pressure, high-power growth film, Sample B “HHP-N₂” seen in Figure 3.6 b), is characterized by longer individual grain structures, with lengths up to 600 nm and clusters resembling stacks of hay.

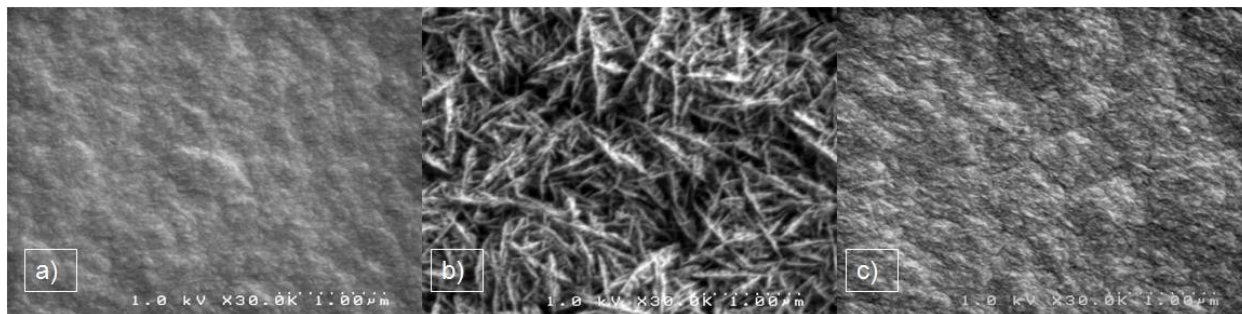


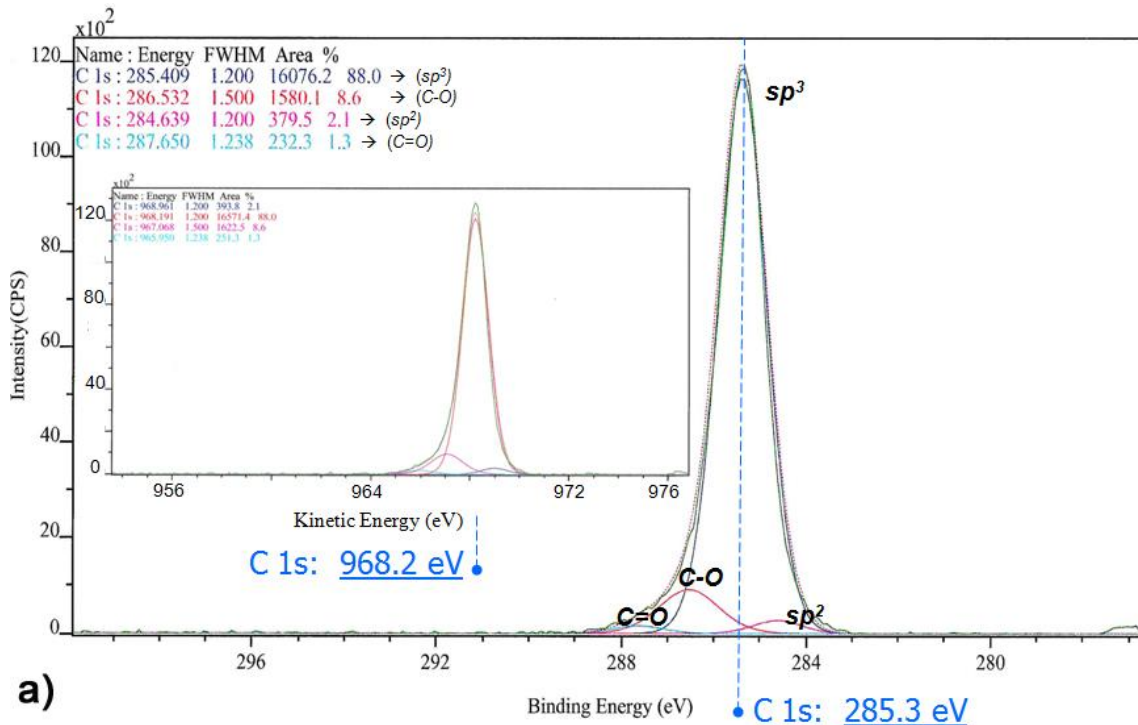
Figure 3.6. Nanodiamond thin film Samples A, B, and C viewed at 30 k \times magnification. When comparing the low growth rate films, a) and c), the grain boundaries become more well-defined when nitrogen is used in the reactant gas.

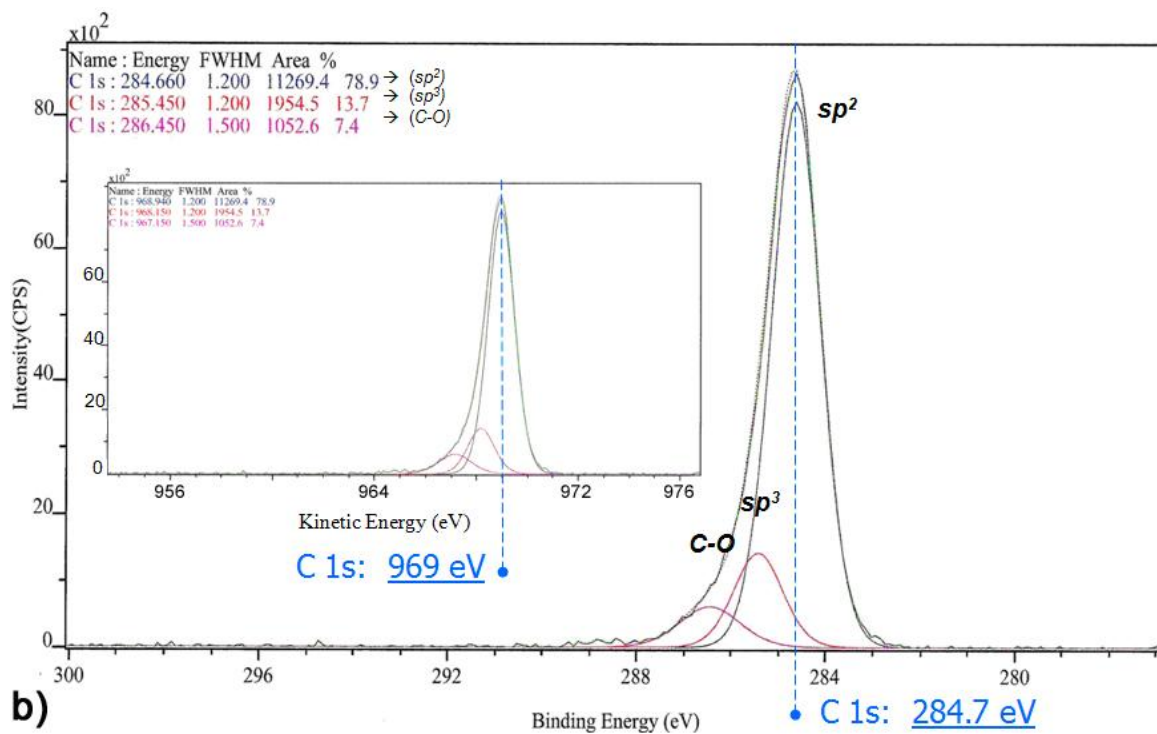
3.4.1 XPS Results

The corresponding XPS spectra are shown in Figure 3.7. The intensity and relative content of the sp² and sp³ hybridized configurations are summarized in Table 3.1. The full width at half-maximum (FWHM) for the C1 (C=C), C2 (C-C), and C3 (C-O) components remain constant at 1.2 eV, 1.2 eV, and 1.5 eV, respectively, for all three films. There was no broadening

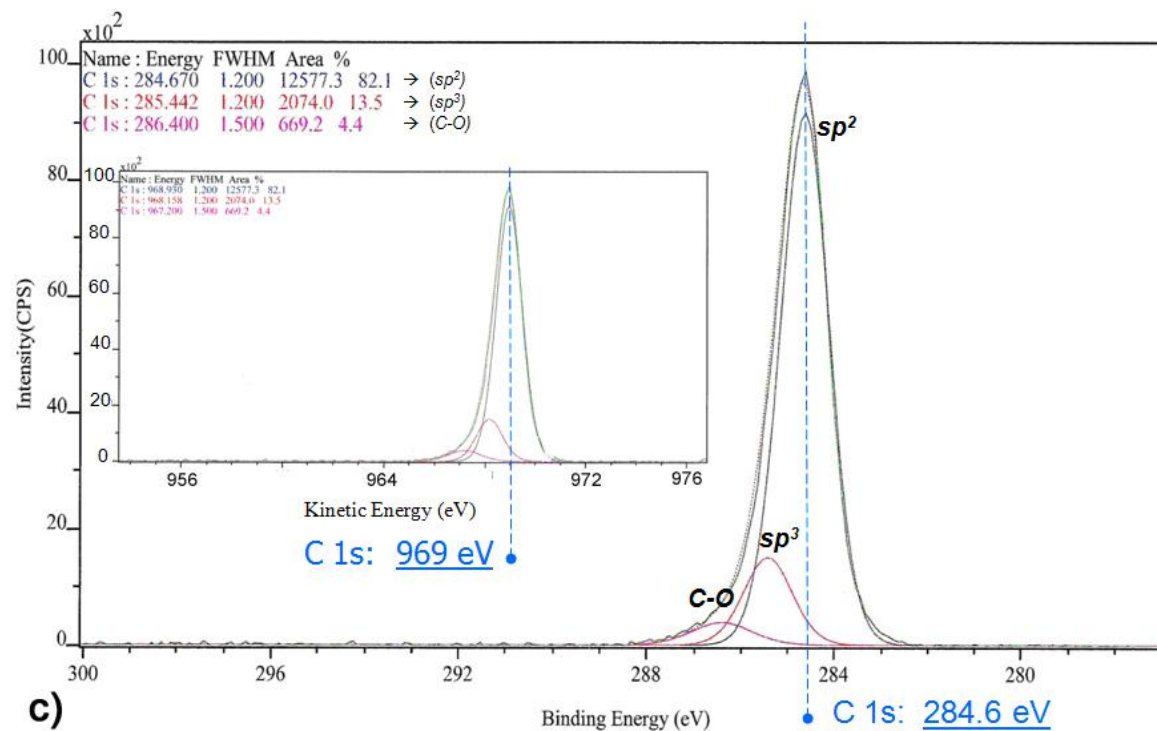
of the FWHM peaks, indicating the same atomic bonding types for all three samples. The amount of nitrogen incorporation was not within the detection sensitivity limits of XPS [74], however, its effect presence is evident due to the structural and sp^2/sp^3 concentration changes. The concentration was obtained using the area under each C 1s component. Sample A showed the highest sp^3 intensity (more insulating) while Sample C contained the highest relative sp^2 intensity. A shift to lower binding energy is observed for Samples B and C when compared to the undoped Sample A, indicating the electrons from the latter samples escaped more easily into the vacuum.

The insets of Figure 3.7 a) through c) show the corresponding C 1s kinetic energy spectra. Table 3.1 and Table 3.2 summarize the kinetic and binding energy components for each film. Sample C possessed the highest sp^2 content, sp^2/sp^3 ratio, and the highest kinetic energy electrons.





b)



c)

Figure 3.7. a) C 1s of *Sample A*, a non-nitrogenated, low growth rate film. b) C 1s of *Sample B*, a high-pressure high-power growth rate film with N_2 reactant gas used. c) C 1s of *Sample C*, a nitrogenated, low-pressure low-power growth rate film.

Sample	C1 (KE, Area%)		C2 (KE, Area%)		C3 (KE, Area%)		C4 (KE, Area%)	
<i>Sample A</i>	967.07	2.1	968.96	88	968.19	8.6	965.95	1.3
<i>Sample B</i>	968.94	78.9	968.15	13.7	967.15	7.4	0	0
<i>Sample C</i>	968.93	82.1	968.16	13.5	967.2	4.4	0	0
<i>Bonding</i>	C=C		C-C		C-O		C=O	

Table 3.1. Summary of kinetic energy (KE) approximations of electrons for each bonding configuration from Figures 3.6 a)-c). C1 and C2 correspond to sp^2 and sp^3 bonding, respectively. Higher kinetic energy corresponds to a lower binding energy.

Sample	C1 (BE, Area%)		C2 (BE, Area%)		C3 (BE, Area%)		C4 (BE, Area%)	
<i>Sample A</i>	284.64	2.1	285.41	88	286.53	8.6	287.7	1.3
<i>Sample B</i>	284.63	78.9	285.45	13.7	286.45	7.4	0	0
<i>Sample C</i>	284.67	82.1	285.44	13.5	286.4	4.4	0	0
<i>Bonding</i>	C=C		C-C		C-O		C=O	

Table 3.2. Binding energy (BE) and bonding components of C 1s. C1 and C2 correspond to sp^2 and sp^3 bonding, respectively. The percent area contribution is also shown.

The more insulative Sample A is characterized by a 42.3 sp^3/sp^2 peak ratio (0.024 sp^2/sp^3 peak ratio). The corresponding bonding content, as shown by the C 1s spectra for sample A, was dominated by 88% sp^3 carbon bonding type. Sample B is characterized by a sp^2/sp^3 peak ratio of 5.3 with 78.9% of the C 1s area dominated by sp^2 bonding. The sp^2/sp^3 peak ratio for sample C was 6.0 and the C 1s area was dominated by 82.1% sp^2 bonding type. It can be inferred that the C 1s shift to lower binding energy, which was characteristic of the nitrogenated films, is due to the relatively high sp^2/sp^3 content.

3.4.2 Field emission performance:

Based on the previous section, it can be expected that a nitrogen-incorporated nanodiamond film with a higher sp^2/sp^3 ratio would yield the lowest turn on field. The electron field emission behavior corresponding with the diamond films presented in Figure 3.6 are shown in Figure 3.8. The negative slopes of the linear F-N curves prove that all three films exhibit Fowler-Nordheim tunneling emission behavior. As shown by equation 2.3, The F-N emission current I is a function of enhancement factor β , the applied electric field E , and material work function. The β value for sample B was estimated to be ~ 100 and assuming a constant β value across all films for simplicity, the effective work function for samples A, B, and C are ~ 1.8 eV, ~ 0.9 eV, and ~ 0.6 eV, respectively. We can then deduce that the film that exhibited the shallowest relative F-N slope also possessed the smallest relative work function, which would be in agreement with [28], namely the increase in sp^2/sp^3 ratio results in field emission enhancement since the associated defects including grain boundaries, vacancies, and stacking faults, essentially raise the Fermi level, permitting electrons to emit directly into vacuum. As shown by the inset of Figure 3.8, Sample C exhibited a shallower slope than Sample A, corresponding with having the lowest turn-on field.

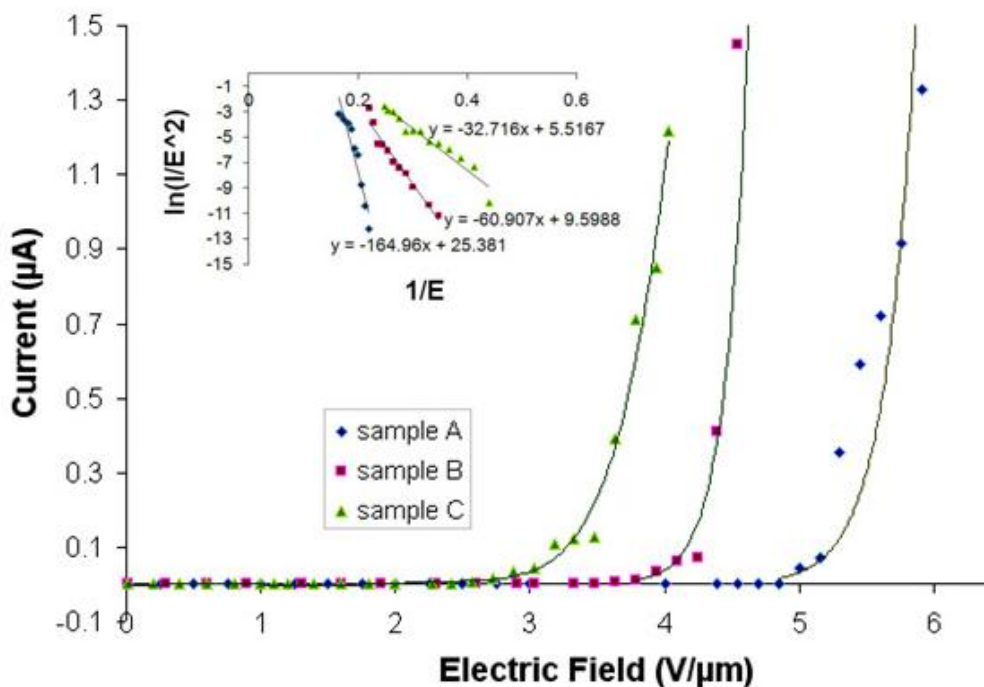


Figure 3.8. (I - E) curve of *Sample A*: a non-nitrogenated, low growth-rate film characterized by a turn-on field at ~ 5.75 V/ μm ; *Sample B*: a nitrogenated high growth-rate film with turn-on field at ~ 4.8 V/ μm ; and *Sample C*: a nitrogenated low growth-rate film with turn-on field at ~ 3.6 V/ μm . The negative linear slopes show that all films exhibit Fowler-Nordheim tunneling emission. The slopes becoming shallower from *Sample A* to *Sample C* communicates the effect of increased sp^2 content on work function and field enhancement factors.

3.4.3 Summary:

It was shown that nitrogen incorporation in diamond leads to significant changes in the film morphology and the relative amount of sp^2 -bonded carbon content. By comparing the binding energy characteristics of each film we found that the nitrogen-incorporated nanodiamond films that were physically characterized by clustering nano-sized grains also possessed the lowest binding energy. This condition is favorable for field emission since electrons with lower binding energy can escape into the vacuum more easily.

From the I - E curves in Figure 3.8 it was seen that there was also a distinct change in emission characteristics between films that were synthesized with and without nitrogen in the

precursor reactant gas. When the sp^2 content in a diamond film was increased as a result of nitrogen incorporation at low growth-rate conditions, the threshold field was reduced to ~ 3.5 V/ μm from ~ 5.75 V/ μm when compared to an undoped low-growth rate film. The results are in agreement with previous reports that a higher sp^2/sp^3 ratio indicates a larger overlap of sp^2 clusters that are embedded in an insulative sp^3 medium. Since the overlap would create a good interconnection between the sp^2 clusters, electron emission to the surface layers would be more easily accomplished [44].

Comparing XPS and field emission results, the film that was characterized as exhibiting the lowest turn-on field also contained electrons with the lowest relative binding energy. The same film also exhibited the shallowest Fowler-Nordheim slope, indicative of a lower effective work function. Therefore, nitrogen incorporation promotes favorable electron emission characteristics from diamond.

3.5 Micro-Raman and electron field emission characterization of nanodiamond films

This study extends the research from section 3.4 to include the effect of surface abrasion techniques on nanodiamond properties. Micro-Raman spectroscopy was introduced as a tool for monitoring changes in graphite and diamond content across five different film configurations. Details of the five different nanodiamond surface morphologies were captured using SEM at 60 k \times magnification. As seen in Figure 3.9 the diamond film surface features vary between nano-sized grained clusters to long-grained “haystacks”. The nano-grained clusters, also known as “cauliflower” per Subramanian [6], are further characterized by individual grain sizes on the order of ~ 10 nm, resulting from using a ~ 0.16 $\mu\text{m/hr}$ growth rate. Sample C, as distinguished by ~ 250 nm grained, needle-like haystacks, resulted from a 0.4 $\mu\text{m/hr}$ growth rate. In comparison

to Samples D and E where no nitrogen gas was used in the precursor reactant mixture, the grain boundaries of Samples A and B appeared coarser, with more distinct grain boundary definition.

3.5.1 Surface preparation techniques:

Bias enhanced nucleation (BEN) was explored and compared to traditional mechanical polishing in effort to standardize seeding techniques. Mechanically polishing does not allow a high degree of reproducibility from one operator to another. Furthermore, abrasion of the silicon surface with diamond powder may damage and roughen the substrate surface if not performed correctly, potentially resulting in a diamond film with irregular crystal sizes which may in turn adversely affect material properties and device patterning results. Bias enhancement should not cause any mechanical damage to the substrate. In this research, BEN was applied at a bias voltage of -200 V for one hour. As revealed by the SEM images of Samples A and D in Figure 3.9, the application of a negative bias to the substrate prior to deposition resulted in considerably denser volume of grain boundaries, which is promising for electron emission due to the increase in potential emission sites.

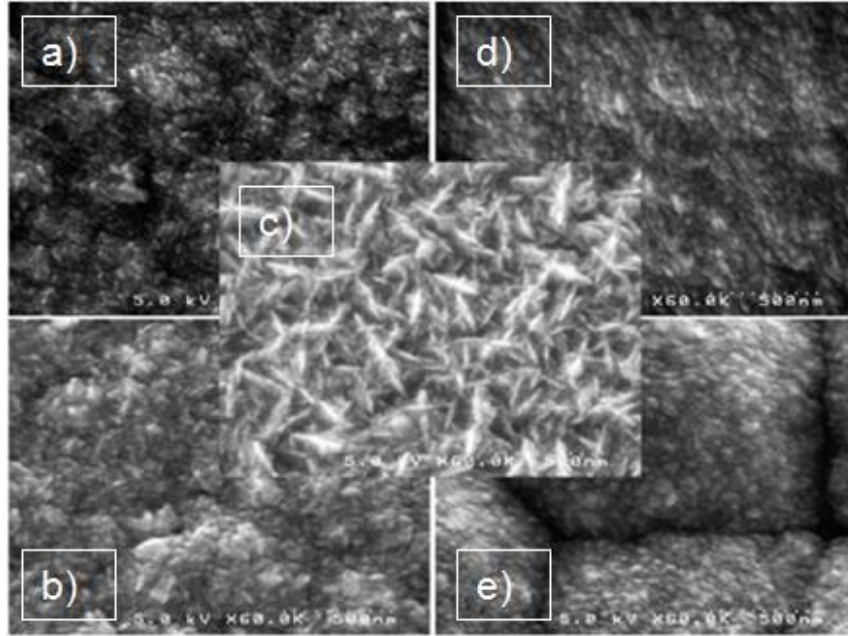


Figure 3.9. SEM of nanodiamond films showing the effect of surface preparation and growth rates: a) BEN-prepared, low growth-rate nitrogen-incorporated film; b) low growth-rate nitrogen-incorporated film; c) high growth-rate nitrogen-incorporated film; d) BEN-prepared, low growth-rate intrinsic film; and e) low growth-rate intrinsic film. BEN prepares the sample surface for a high volume of grain boundaries and as the growth rate is increased, the grain sizes get larger.

The grain sizes were effectively decreased by lowering the growth rate through the adjustment of the CVD process parameters, including the microwave power, reactant pressure, and gas flow rate as before. By reducing the microwave power from 1000 W to 550 W and the reactant pressure from 28 Torr to 13 Torr, nano-sized grained diamond films were reduced from the more sparsely distributed haystack structure to the more continuous nanodiamond configuration, in agreement with [51]. Table 3.3 is a summary of the recipes that were used in this work.

Sample	Precursor	Power	Pressure	Temperature	BEN
Sample A	CH ₄ /H ₂ /N ₂	660 W	20 Torr	800 ° C	-200V
Sample B	CH ₄ /H ₂ /N ₂	550 W	20 Torr	800 ° C	0
Sample C	CH ₄ /H ₂ /N ₂	1000 W	28 Torr	800 ° C	0
Sample D	CH ₄ /H ₂	660 W	20 Torr	800 ° C	-200V
Sample E	CH ₄ /H ₂	550 W	20 Torr	800 ° C	0

Table 3.3 Recipe summary for Samples A –E.

By comparing both mechanical polishing and bias enhanced nucleation results, it can be gathered that in addition to low growth rates, seeding techniques play a large role in decreasing the grain size and increasing the nucleation density. During the MPECVD diamond growth process, lowering the microwave power and decreasing the reactant pressure effectively decreased reaction processes and starved reactions that would otherwise form larger grain sizes. Henceforth, the two events, diamond nucleation and growth competed against each other for the limited amount of energy available and in this condition the nucleation density increased and the grain size significantly decreased [51], leading to the growth of a nanodiamond film.

3.5.2 Raman spectra

Figure 3.10 shows the Raman spectra for the diamond films from Figure 3.8 and Table 3.4 summarizes the peak characteristics of each sample. Diamond sp³ bonding is well known to be assigned to 1332 cm⁻¹ [73]. Nanocrystalline diamond would also exhibit a peak in the 1150 - 1170 cm⁻¹ range, confirming a nanocrystalline phase interspersed in the diamond film [6, 75]. In general nanodiamond films are known to exhibit a relatively broad peak at 1332 cm⁻¹ [6, 73], indicating a hybrid structure. Interestingly, as shown in this work, as the grain size was reduced to the lower nanometer range as with Sample A, the Raman graphite peak increased and subsequently surpassed the diamond peak intensity. Sample A further exhibited another peak sp²

-related peak at $\sim 1350\text{ cm}^{-1}$, indicating disordered, non-crystalline sp^2 bonded carbon, contributing to its low threshold field as discussed in section 3.5.3.

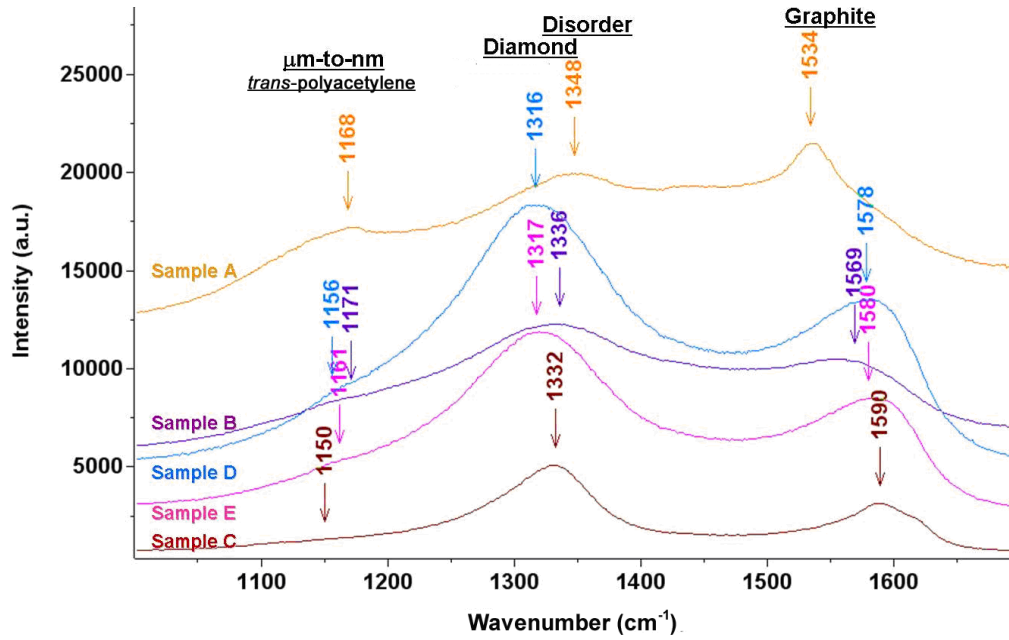


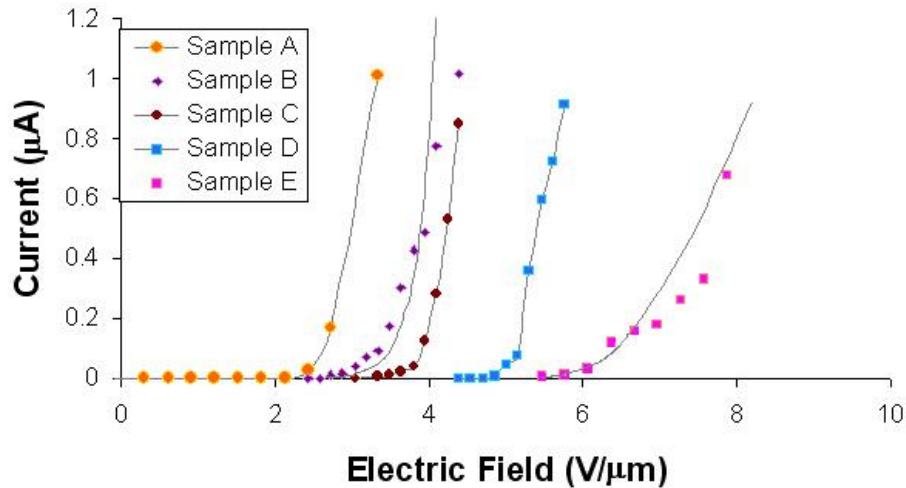
Figure 3.10. Raman spectra of the CVD diamond films.

Sample	$\mu\text{m-nm ND transition}$	Diamond ₁ (cm ⁻¹)	Diamond (cm ⁻¹)	Disorder (cm ⁻¹)	HOPG (cm ⁻¹)	sp ² /sp ³
Sample A	1168	-	-	1343	1534	1.8
Sample B	1171	-	1334	-	1569	6.4
Sample C	-	-	1335	-	1596	2.5
Sample D	1156	1315	-	-	1586	0.03
Sample E	1161	1323	-	-	1586	0.03

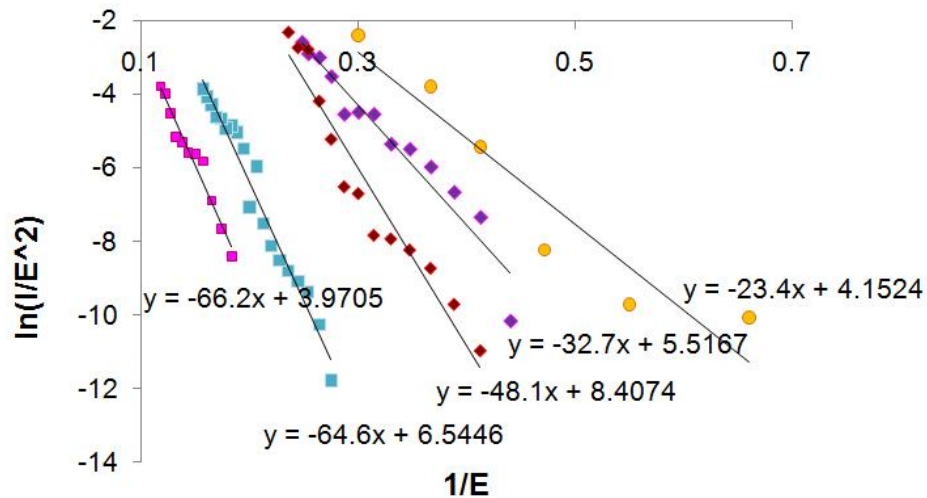
Table 3.4. Summary of Raman peak assignments and sp^2/sp^3 ratio of all film spectra.

3.5.3 Electron field emission:

The electron field emission behavior and F-N conformance of the five diamond films, as shown in Figure 3.11, can be used to relate the changes in field emission behavior to variations in nucleation seeding methods coupled with film synthesis conditions.



a) (I - E) curve of *Sample A*: BEN-prepared, low growth-rate nitrogen-incorporated film characterized by a turn-on field at ~ 1.5 V/ μm ; *Sample B*: low growth-rate nitrogen-incorporated film with turn-on field at ~ 2.2 V/ μm ; *Sample C*: high growth-rate nitrogen-incorporated film with turn-on field at ~ 2.4 V/ μm ; *Sample D*: BEN-prepared, low growth-rate intrinsic film with turn-on field at ~ 3.6 V/ μm ; and *Sample E*: low growth-rate intrinsic film with turn-on field at ~ 5.5 V/ μm .



b) All five films exhibit Fowler-Nordheim tunneling emission behavior. Increasingly shallower slopes indicate a combination of field enhancement factors and a reduced work function as a result of increased sp^2 content. The negative linear slopes show that all films exhibit Fowler-Nordheim tunneling emission. The slopes becoming shallower from *Sample A* to *Sample C* communicates the effect of increased sp^2 content on work function and field enhancement factors.

Figure 3.11. a) I - E characteristics of the five different films presented and this study and b) the corresponding F-N behavior.

From Figure 3.11 a), it can be readily seen that Sample A, the ND film dominated by sp^2 content in terms of relatively high disorder and graphitic bonding, returned the lowest threshold field at $3.3 \text{ V}/\mu\text{m}$, as compared to intrinsic nanodiamond in which the turn-on field was at $\sim 8.2 \text{ V}/\mu\text{m}$. The effective work function for samples A, B, C, D, and E are $\sim 0.5 \text{ eV}$, $\sim 0.6 \text{ eV}$, $\sim 0.8 \text{ eV}$, $\sim 0.94 \text{ eV}$, and $\sim 0.98 \text{ eV}$, respectively. The results indicate that with a small ratio of nitrogen reactant gas, defects such as grain boundaries and other imperfections may be introduced in a diamond film and effectively enable a more conductive behavior that would result in a reduced threshold field. The corresponding low effective work function is presumably due to the increased sp^2 content and grain boundary emission as a result of increased nitrogen incorporation at a low growth rate.

3.5.4 Summary:

SEM imagery showed the changes in crystal size from $\sim 250 \text{ nm}$ down to $\sim 10 \text{ nm}$ as we varied the growth rate from $\sim 0.4 \mu\text{m}/\text{hr}$ to $\sim 0.16 \mu\text{m}/\text{hr}$. Nanodiamond films have a smoother and more uniform morphology compared to a film with larger-grained features. Finely abraded surfaces contributed to the low surface roughness that is important for subsequent micro-patterning and device formation. Raman spectroscopy analysis was performed on all five films and the results consistently showed that films characterized by decreasingly smaller grain sizes exhibited a relatively high degree of sp^2 -bonded carbon content.

All F-N plots exhibited negative slopes, confirming F-N governance and revealing cold field emission behavior. According to F-N theory [76-77] the emission current is dependent on material work function and field enhancement features; as the sp^2 content was increased the F-N slopes became shallower, suggesting reduced work function and possibly more effective field

enhancement factors. The diamond films containing increasingly higher sp^2 bonding content, as indicated by both D and G bands, consistently exhibited reduced turn-on fields.

3.6 Nanodiamond film study conclusions

In this chapter, considerable efforts were taken to identify the optimal nanodiamond film configuration for subsequent lateral device fabrication. The inter-electrode spacing cannot be reduced much further from the sub-micron range therefore the emitter material choice for field emission applications is of utmost importance. External research indicated the important role of embedded conductive nanostructures in providing diamond and related materials the capability for low field emission. Tuck et al., Forbes et al., and Toyama et al. [63, 44, 65] proposed hybrid structures that are in agreement with our reported MIM conduction model [5-6] for nitrogen-incorporated nanodiamond films. To arrive at a smooth, conductive nanodiamond film structure, surface abrasion and growth parameters were carefully considered. Bias-enhanced nucleation may offer a less abrasive technique for creating diamond nucleation sites, however mechanical polishing may also be optimized to achieve continuous, nanocrystalline diamond using nitrogen-incorporated low CVD growth rate conditions.

With the optimal nanodiamond film configuration identified, Chapter IV describes the procedures involved with the design, fabrication, and characterization of EBL-delineated nanodiamond lateral field emission diode technology.

CHAPTER IV

SUB-MICRON GAP LATERAL FIELD EMISSION DEVICE DESIGN AND CHARACTERIZATION APPROACH

This research is focused on the development of a series of nanodiamond lateral field emission diodes, particularly with a sub-micron emission gap design, owing to the configuration's immense and unexplored potential as a microelectronic device. Electron field emission, as described in chapter II, is highly dependent on the cathode-anode distance and the emitter tip geometry. In recent years there has been much interest in the study of diamond lateral field emission devices [6, 78-79], however a sub-micron gap delineation is yet to be reported. Minimizing the gap is necessary for achieving a sub-volt turn-on. However, the fabrication of nanodiamond lateral devices is a subtractive process. Each additional process that requires etching for selectively removing unwanted material potentially widens the final emission gap delineation, for example, over-etching the surface metal masking layer may cause a sub-micron gap design to be transferred onto the diamond film as a $> 1 \mu\text{m}$ emission gap pattern. Electron beam lithography (EBL) is introduced in this research in order to achieve the sub-micron gap design requirements.

Micron-range anode-cathode spacing defined using conventional photolithography and RIE processes have been reported for the nanodiamond lateral device configuration [6]. Incorporating EBL into the fabrication process would require the development of a new series of recipes in order to optimize material compatibility. Research for achieving an EBL-designed, sub-micron emission gap nanodiamond lateral device would involve the identification of photoresist type and thickness, metal masking material, EBL patterning parameters, design development time, and RIE etching conditions.

4.1 Overview of lateral vacuum field electron emission devices in diode configuration

A field emission diode can be designed for sub-volt turn by minimizing the anode-cathode spacing. The fundamental lateral field emission diode operation is described by Figure 4.1. The electrodes are separated by a vacuum medium. When a sufficient voltage greater than the turn-on value is applied to the anode, electrons are extracted from the cathode tip and emitted into the vacuum. These electrons travel through the inter-electrode space, strike the anode and are absorbed. As the inter-electrode spacing is reduced to the sub-micron range, the voltage requirement for extracting the electrons would be substantially less.

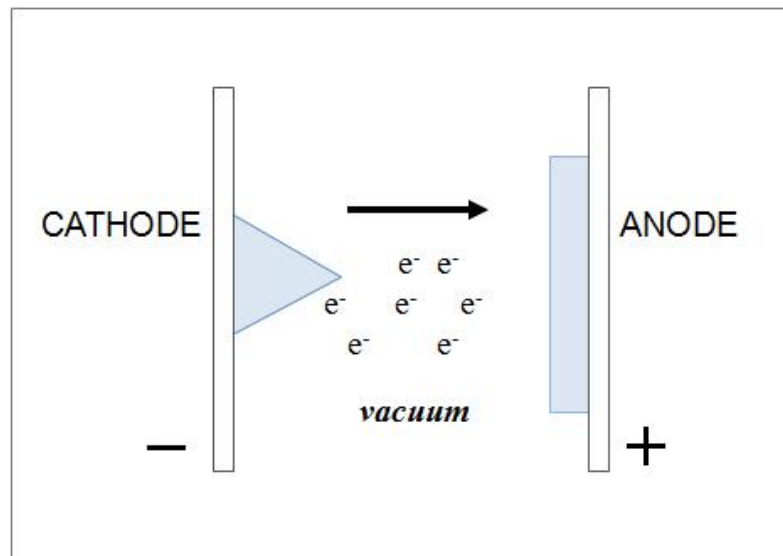


Figure 4.1. Lateral field emission diode operation.

Patterning techniques that can be used to build the lateral devices include optical lithography [6], EBL [81], oxidation sharpening [33], separation by implantation of oxygen (SIMOX) [17], and standard wet and dry chemical etch processing [82]. Sub-micron spacing has been achieved, however the reported turn-on voltages are 13 V- 40 V [17-18 and 33]. CVD

diamond, specifically nanodiamond, has been used to demonstrate efficient and reliable VFEDS due to its desirable attributes including low electron affinity and low work function upon nitrogen incorporation [6]. However, very little work has been reported on diamond lateral devices with sub-micron emission gap due to the difficulty in realizing micron/sub-micron gap electrode isolation. In this research we have developed an EBL-integrated process for achieving the sub-micron gap configuration.

4.2 Process development for the fabrication of the nanodiamond lateral field emission diode

There are four physical ways for decreasing the turn-on voltage/field: (1) reducing the cathode material work function; (2) decreasing the anode-cathode distance; (3) enhancing the effective field at the emitter tip through sharpening; and (4) increasing the number of emitter tips for a given area, i.e., tip density. While the first method was addressed in Chapter III, the last three approaches will be discussed in Chapter V.

The EBL-delineated lateral vacuum diodes that are reported in this work were designed to be self contained; the design is comprised of an array of uniformly spaced, high aspect ratio, finger-like cathode emitters separated by a small distance and isolated by an oxide (SiO_2) layer from a straight-edged, integrated anode structure. Two different approaches were employed to incorporate EBL into the sub-micron gap lateral device fabrication process, namely a mixed lithography approach combining conventional optical lithography with EBL and an EBL-only process for the complete device delineation. Figure 4.2 shows an image of the EBL vacuum chamber and illustrates the beam-writing process.



Figure 4.2. A snapshot showing the EBL chamber.

Software-driven EBL designs are versatile. Figure 4.3 a) shows an EBL mask design layout for patterning multiple diodes on a single film sample. Figure 4.3 b) shows the notional device configuration and material stack-up for fabricating a nitrogen-incorporated nanodiamond lateral field emission diode device. Figure 4.4 a) shows the SEM cross-section of a structure corresponding to the material stack-up illustrated in Figure 4.4 b). The active silicon layer of a silicon-on-insulator (SOI) substrate serves as the supporting structure during fabrication but is removed from the critical device area prior to characterization in order to avoid contribution by the silicon to the device performance.

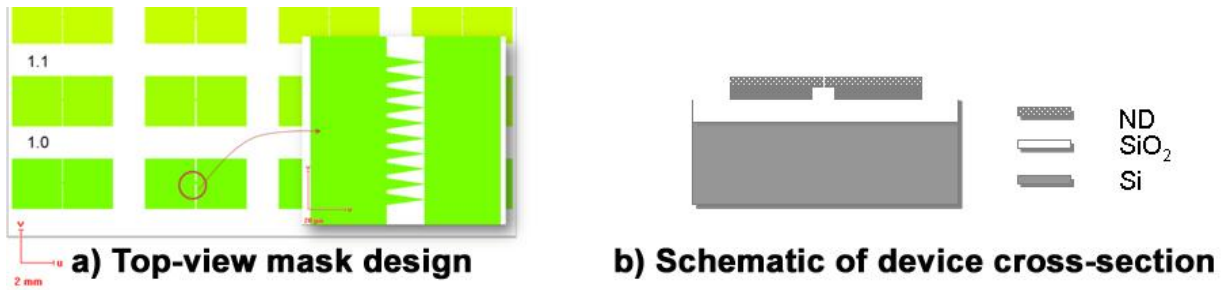


Figure 4.3. The lateral diode is designed to have a) $2\text{ mm} \times 2\text{ mm}$ contact pads and a $20\ \mu\text{m} \times 100\ \mu\text{m}$ device area. The top-down material configuration consists of b) $\sim 1\ \mu\text{m}$ nanodiamond, $2\ \mu\text{m}$ silicon, $4\ \mu\text{m}$ oxide, and $525\ \mu\text{m}$ Si.

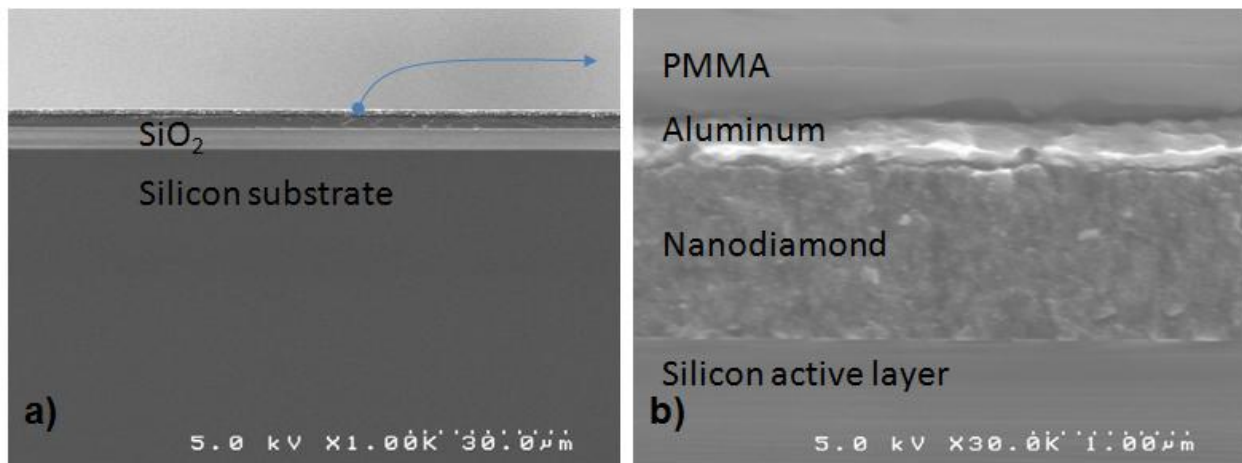


Figure 4.4. a) Cross section of substrate configuration used for lateral device fabrication; b) SEM at $30\ \text{k}\times$ magnification showing the top 4 layers of the material stack. As shown, the PMMA and aluminum are $\sim 500\ \text{nm}$, ND is $\sim 1\ \mu\text{m}$ thick, and the active Si layer is $\sim 2\ \mu\text{m}$.

4.3 Lateral Device Field Emission Characterization

The electrical performances of all lateral diodes were characterized in a 10^{-6} - 10^{-7} Torr vacuum environment. As illustrated in Figure 4.5, gold metal dots were placed on the nanodiamond contact pads of the cathode and anode of the lateral device and were electrically connected to the circuit using metal probes. Figure 4.6 shows the field emission setup. The

devices were seated on a heater stage; prior to I-V characterization the devices were subject to conditioning, including thermal treatments.

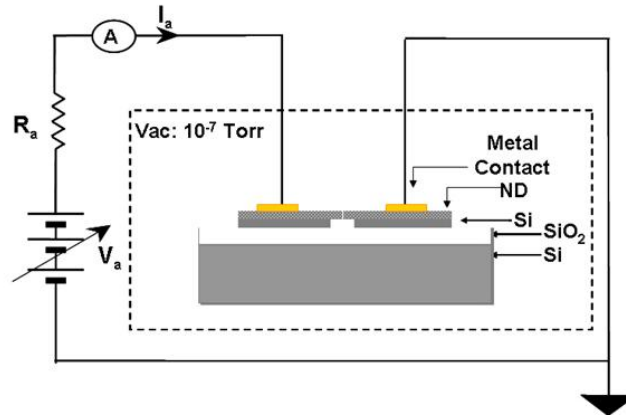


Figure 4.5. Diagram of the vacuum field emission test set-up for the nanodiamond lateral diode.

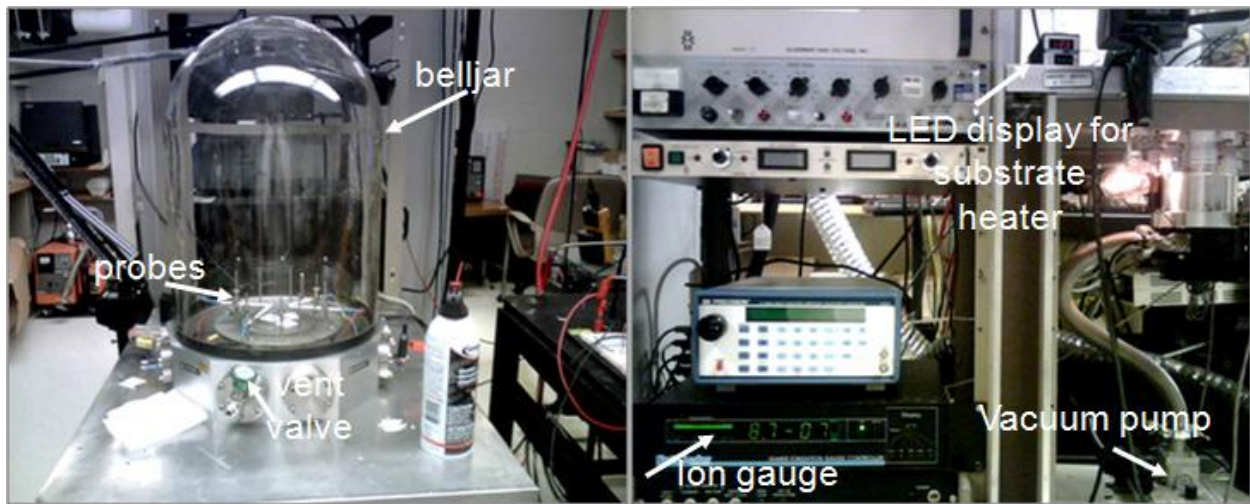


Figure 4.6. Field emission characterization setup.

4.3.1 Device Conditioning:

Prior to performing emission characterization, the devices were subjected to vacuum thermal-electric (VTE) treatment [6]. It has been reported that following VTE, emitter structures exhibit an increased local electric field on the tip surface for a given applied voltage [78]. The

increase in field can lower the turn-on voltage and cause a desirable shift of the I-V characteristic (higher emission current per given bias). Spindt et al. [83] applied 35 V to his emitter array for an extended time and found that the emission current increased from five to six orders of magnitude.

VTE conditioning is a process performed by heating the cathode to $\sim 150^{\circ}\text{C}$ while under vacuum [5] and the emission current is kept at a constant value, e.g. $1\ \mu\text{A}$, by adjusting the anode voltage. The VTE treatment is repeated until a stable current is obtained for a considerable amount of time, usually 1-2 hours. Deviations from this treatment are individually noted accordingly in each sub-section of Chapter V.

CHAPTER V

SUB-MICRON GAP LATERAL VACUUM FIELD EMISSION DIODE FABRICATION AND CHARACTERIZATION

This chapter describes the processing techniques developed for the fabrication of sub-micron gap lateral field emitter devices. A discussion on the electrical performance follows the device fabrication results in each section.

Due to the resolution of optical lithography, much of the early research on lateral vacuum FEDs was limited to inter-electrode spacing in the micron range. Sub-micron spacing would essentially offer high field strength without the use of high voltage and can be achieved using EBL, as proposed in Chapter IV. In this chapter, five studies leading up to sub-volt turn-on, sub-micron emission gap lateral field emission diode devices were conducted. The studies evaluated the: (5.1) compatibility of various metal masks with diamond and EBL parameters for sub-micron gap design; (5.2) demonstration of a mixed-lithography approach and the effect of fluorine-based O₂ diamond etch on lateral device delineation and field emission performance; (5.3) demonstration of EBL-designed lateral diode using thin nanodiamond film; (5.4) effect of 350 nm gap, 3- and 12- emitter tip density on threshold voltage; and (5.5) the outcome from scaling the emission gap into the sub-micron regime on field emission performance.

5.1 Experimental

5.1.1 Metal mask compatibility with nanodiamond

Metal used as an etching mask would protect un-exposed areas on the nanodiamond layer from being removed. Both aluminum (Al) and chromium (Cr) were tested for compatibility with nanodiamond. Thickness is a critical parameter; the mask must be thick enough to withstand the

completion of ND etch. Although aluminum was compatible with nanodiamond, Figure 5.1 shows the results from using insufficient metal masking thicknesses for the diamond etching process.

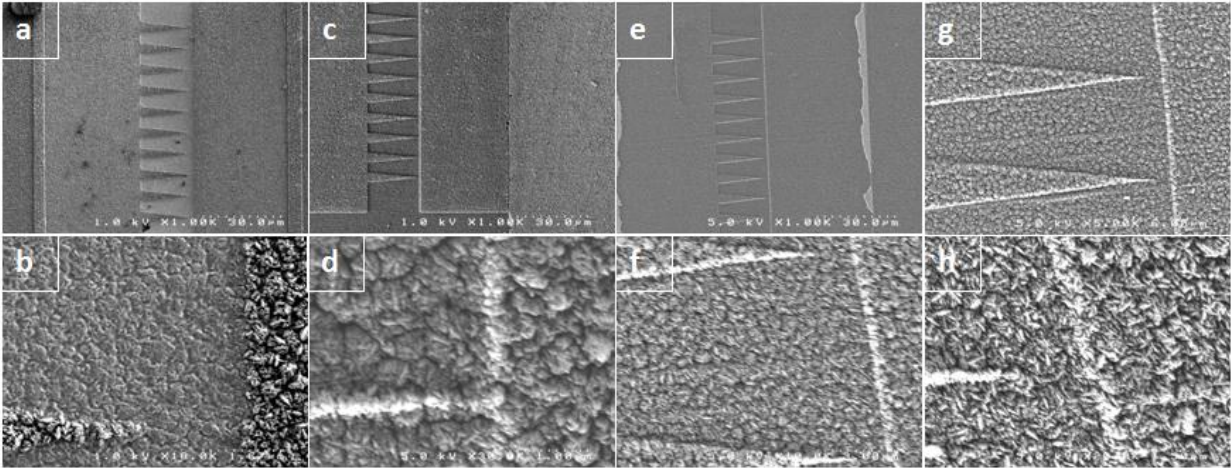


Figure 5.1. SEM micrographs of four different trials of lateral field emitter structures with insufficient aluminum mask thicknesses for withstanding the duration of ND RIE. As a result of the incomplete ND etch, all devices shown were shorted and further processing could not be completed.

Chromium was also evaluated as a diamond mask however, as seen in Figure 5.2, the surface adhesion was poor. SEM observation shows a creeping gap in between the Cr mask and the diamond surface. As a result of the surface incompatibility, there was considerable mask peeling, compromising the design pattern. Since the aluminum did adhere well to the diamond substrate, for subsequent lateral field emission device processing the Al mask thickness was optimized accordingly for individual diamond film configurations. Figure 5.3 shows an example of the adhesion compatibility of PMMA and Al mask with CVD nanodiamond. The selectivity of diamond etch against Al was found to be suitably high for transferring device pattern designs.

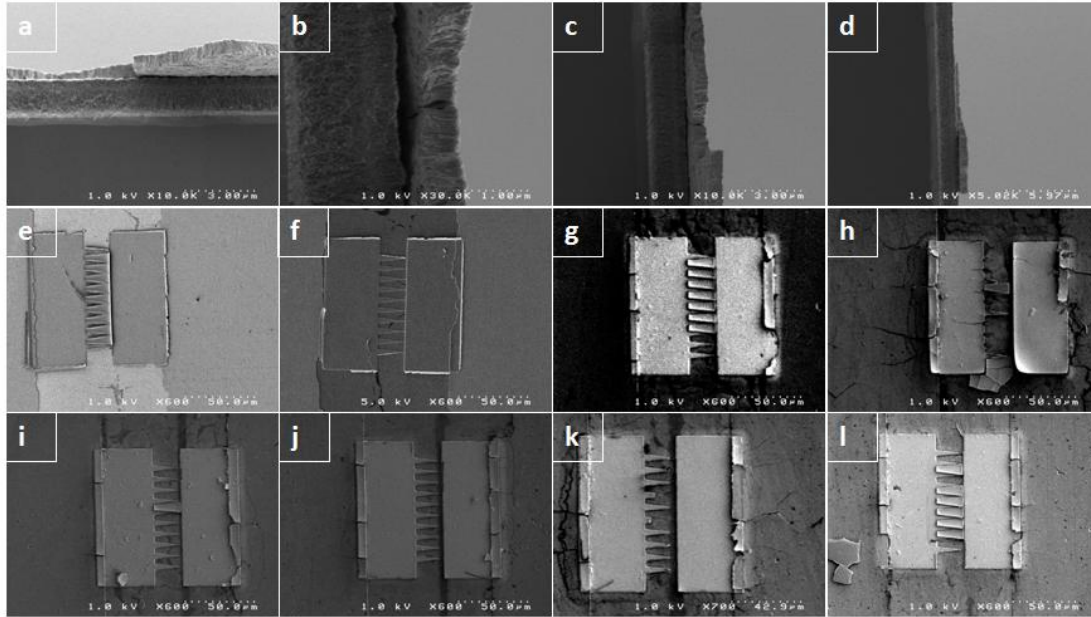


Figure 5.2. SEM micrographs a) - d) show interface incompatibility between the Cr mask and diamond surface. Images e) – l) show mask peeling as a result of poor adhesion.

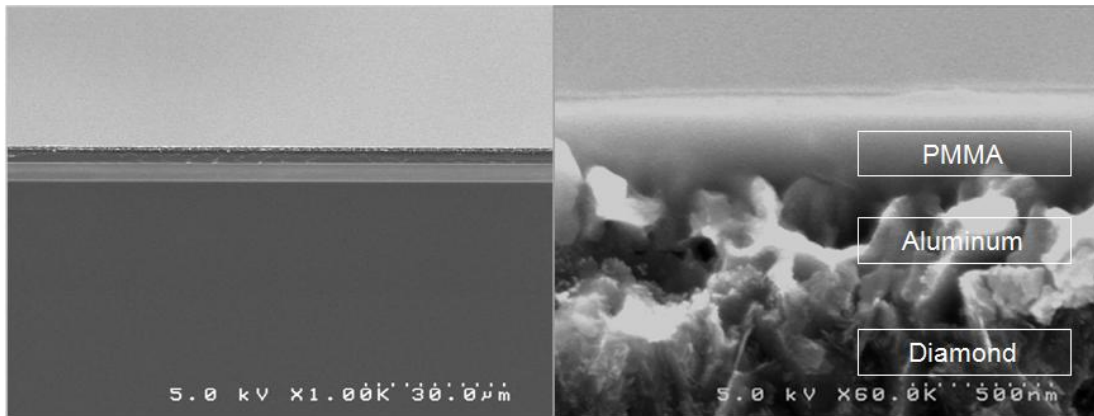


Figure 5.3. SEM cross sections of PMMA, aluminum, and diamond show interface compatibility.

5.1.2 EBL Parameters Experimentation

Whereas optical lithography is limited by the wavelength of the light which is used for exposure, EBL utilizes a direct write system based on moving an electron beam spot with respect to the wafer to expose one pixel at a time [84]. The lateral devices reported in this work were

designed using Raith GDSII software and exposed onto a subject wafer. Several studies were conducted to optimize EBL parameters, including the incident beam voltage, resist thickness, and substrate thickness. Essentially, a reduction in line widths and proximity effects can be attained for progressively thinner films, thereby reducing the lateral extent of electron scattering [86]. Scattering is undesirable due to the potential exposure of areas outside of design patterns [84]. Pattern definition is also sensitive to electron beam dosage and the duration of sample immersion in development solution. The observations are discussed in this section.

a) Accelerating Voltage

There is a delicate balance between an adequate accelerating voltage and tolerable back scattering. Ideally, a higher accelerating voltage (e.g., 20kV, 30kV, etc.) would result in a higher resolution for dense patterns such as sub-micron gap inter-electrode spacing and high aspect ratio cathode emitter structures. However, the well known EBL proximity effect, referring to the variation in width of patterned lines with the density of nearby shapes, makes high resolution difficult to obtain. With increasing accelerating voltage, the electron penetrating path increases, making higher patterning resolution. In contrast, a lower accelerating voltage would cause less back scattering, however the beam resolution may not be sufficient to delineate fine patterns. Figure 5.4 shows the effect of using 10 kV for pattern delineation; the areas in between the cathode fingers were not cleared. The lower accelerating voltage should be reserved for larger line width patterns. With increasing accelerating voltage, the dosage should also be increased to optimize pattern widths.

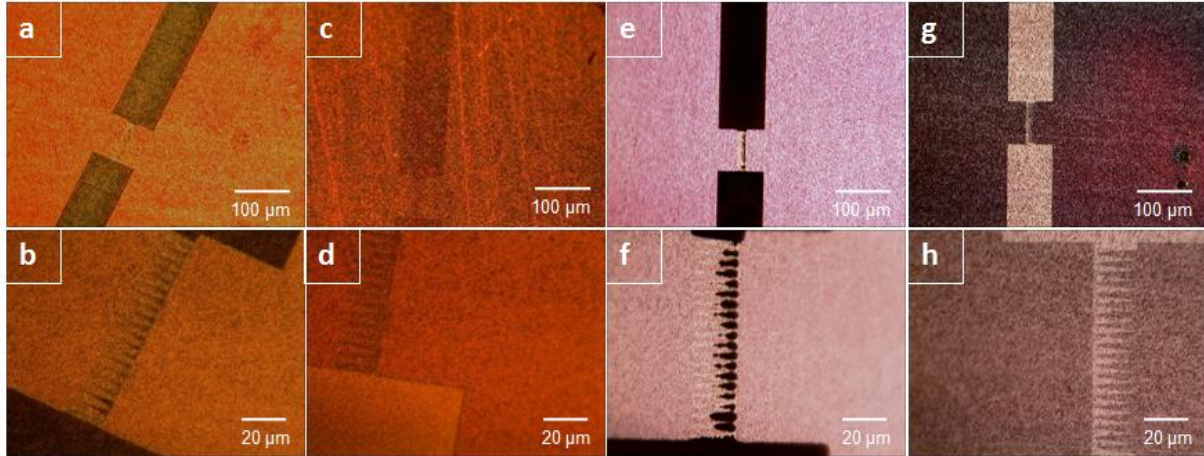


Figure 5.4. Images a) –h) show high and low magnification image pairs of lateral devices where 10 kV accelerating voltage was used for EBL writing. The anode and cathode structures were not distinctly defined.

b) Dosage

Another important EBL parameter to consider for attaining sub-micron gap dimensions is the exposure dose. As a general rule, the exposure dose should be increased for decreasing feature sizes [85]. In this work, insufficient dosage resulted in shorted devices while over aggressive dosage factors resulted in wide inter-electrode distances. Increased dosage is also known to induce cross-linking, a result that forms a negative resist on the surface layer [85]. As a result of the negative resist residue on the substrate, exposed design areas would remain masked. Figure 5.5 is a collection of SEM images showing the effect of increasing the beam dosage. All patterned poly methyl methacrylate (PMMA) coated films were developed using a 1:3 mixture of methyl-isobutyl ketone (MIBK) and isopropyl alcohol (IPA). PMMA is a standard positive resist and for the duration of this research, the anisole-based 950 K molecular weight form was used.

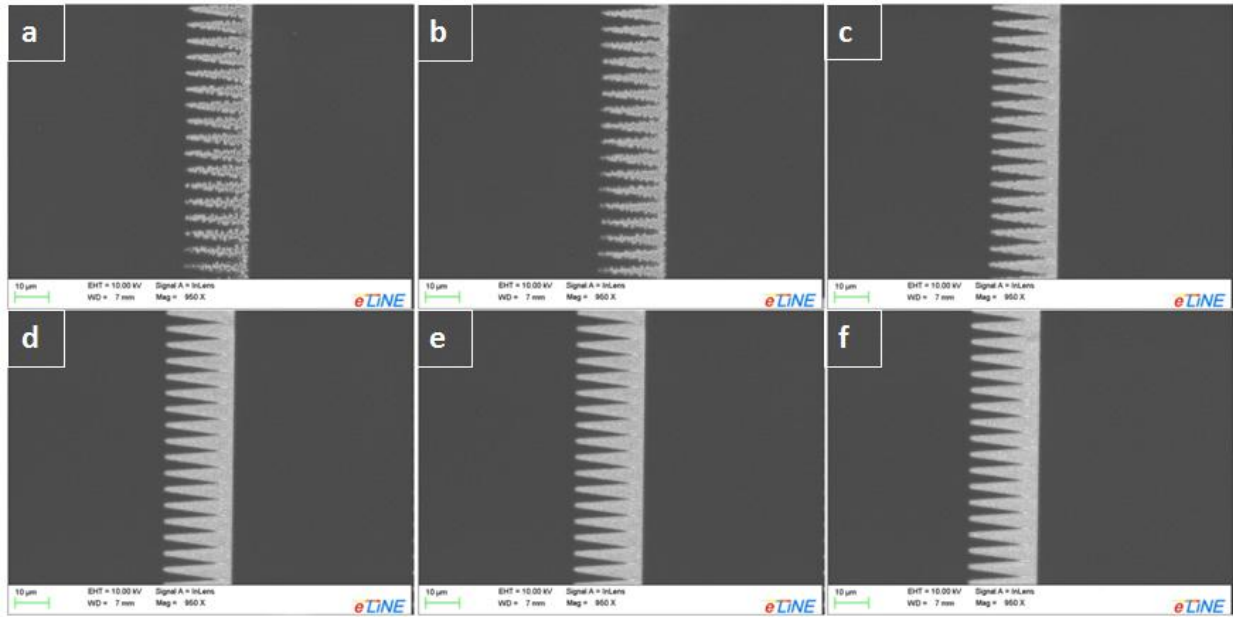


Figure 5.5. SEM images showing the effect of increasing dosage (1.0 to 1.5 of $105 \mu\text{C}/\text{cm}^2$) on a closely packed multi-emitter lateral field emission structure. The dosage increases from a low dose in image a) with the highest dosage in image f). It is clear that as the dosage increases, the area in between the emitters are cleared, however the emission gap also gets progressively wider.

c) Pattern Development

Electron beam exposure decomposes PMMA into fragments that are in turn dissolved preferentially by a developer such as diluted MIBK. EBL designs are highly sensitive to the development time; it was therefore useful to conduct an extensive set of trials in order to find the appropriate developing time per a given substrate configuration. Figure 5.6 are SEM images of the results from two different 4-emitter lateral structures immersed in MIBK:IPA for 30 seconds and 45 seconds. The 15 seconds difference in development time produced a marked difference in emission gap delineation; device a) was shorted while the emission gap distance of the device shown in image f) was $\sim 1\mu\text{m}$.

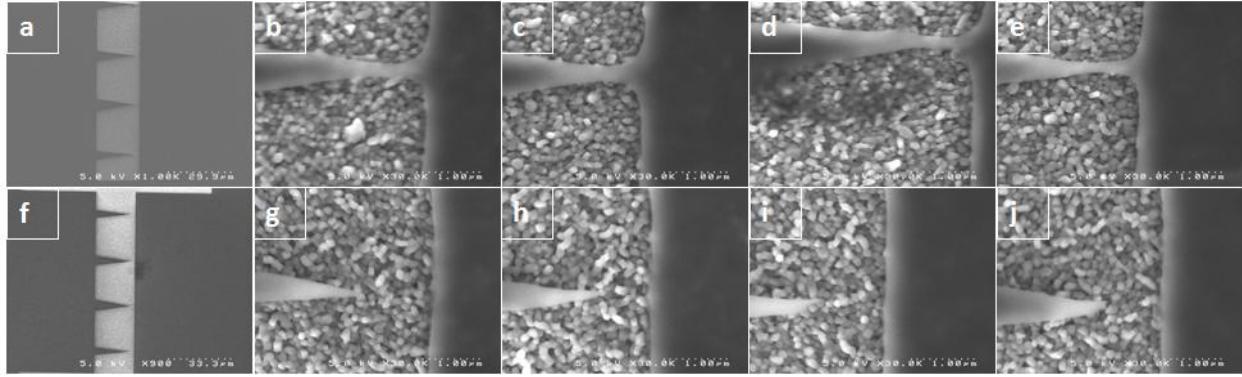


Figure 5.6. Image a) shows a shorted 4-emitter lateral structure as a result of insufficient developing time. Images b) - e) are 30 k \times SEM of image a). Image f) shows an “open” four-emitter lateral structure as a result of adequate immersion in diluted MIBK. Images g) - h) are 30 k \times images showing the $\sim 1 \mu\text{m}$ gap delineation.

5.1.3 Summary

Several variations of metal masking material and EBL designs were attempted before an optimized procedure was selected. Experiments were performed with Al and Cr to determine the candidate that could adhere well to the diamond surface and withstand the duration of ND RIE. Aluminum emerged as the better choice but required thickness optimization based on individual diamond film configurations. This study also showed the importance and sensitivity of the EBL control parameters, providing a vehicle for showing the fundamental influence of the accelerating voltage, dosage, and development time on EBL pattern resolution. In summary the use of Al masking, optimized beam parameters, and timely development schemes are critical for achieving high resolution in EBL design patterns.

5.2 The demonstration of the mixed-lithography approach and the effect of fluorine-based CHF_3/O_2 diamond etch on lateral device delineation and field emission performance

The EBL-designed nanodiamond lateral field emission devices can be fabricated using two different approaches. The first method involves the use of both optical lithography and EBL

(OEB) for designing the lateral diode structures. A second approach, outlined in section 5.4, utilizes only EBL for complete device patterning.

The final outcome of OEB processing varies and is based on etchant gases used for removing exposed unwanted layers of material. The process flow for the OEB is shown in Figure 5.7. The fabrication begins with the growth of a 0.65-1.0- μm thick nitrogen-incorporated nanodiamond film on a silicon-on-insulator (SOI) wafer (2 μm active Si on 1 or 4 μm buried oxide (BOX), all on a 525 μm Si substrate) by $\text{CH}_4/\text{H}_2/\text{N}_2$ MPECVD. Next, the diamond layer was patterned with the lateral device structures using conventional optical lithography. An aluminum metal layer of ~ 400 nm thickness was deposited on the photoresist covered nanodiamond by thermal evaporation. A lift-off procedure was used to lift off any unexposed areas. EBL was introduced for patterning the cathode structures. With aluminum serving as a mask, micropatterning of the nanodiamond film was carried out using various etchant gases as discussed in the following sections. Nanodiamond was selectively removed using coil R.F. power 600 W, platen R.F. power 100 W, oxygen flow rate of 30 sccm, and pressure 10 mTorr. Silicon was then etched to expose the SiO_2 layer of the SOI substrate, isolating the nanodiamond cathode and anode. The silicon etching process varied between using only SF_6 and SF_6/O_2 RIE to ensure no etching of the underlying SiO_2 . The process parameters were R.F. power 100 W, reactant pressure of 150 mTorr, and gas flow rate ratio of 10:1 sccm (SF_6/O_2). Post-fabrication, the nanodiamond lateral devices were subjected to industry standard Radio Corporation of America (RCA) chemical cleaning procedure to remove any contaminants that were present on the emitter surface.

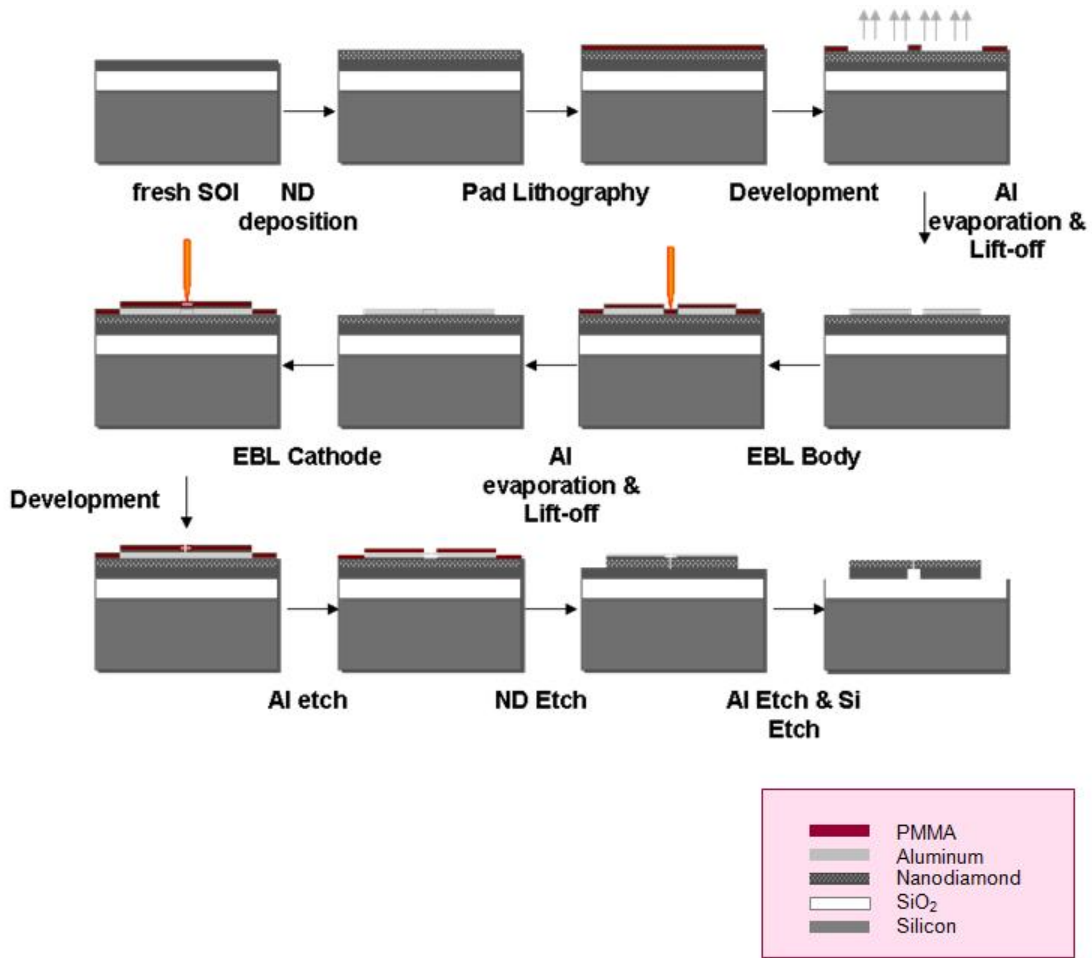


Figure 5.7. Process flow for the mixed-lithography fabrication approach.

5.2.1 CHF₃/O₂ fluorine-based diamond etch fabrication results

In order to obtain a minimum feature size of less than 100 nm, it was reported by Otterbach that 8:1 CHF₃/O₂ plasma should be used [86]. The CHF₃ trifluoromethane, more commonly known as fluoroform, is a by-product of Teflon, a polymer coating [87]. In accordance with literature [88], pure oxygen dominated plasmas would result in a fast removal of diamond however Otterbach suggested the addition of CHF₃ to reduce the roughening of the diamond surface. The results from using CHF₃/O₂ plasma to define 4- and 12-emitter nanodiamond lateral diodes can be seen in Figure 5.8. Using SEM markers, the anode-cathode

spacing was measured to be $\sim 1.2 \mu\text{m}$ and the cathode area for the 12-emitter device $\sim 5750 \mu\text{m}^2$ while the cathode area for the 4-emitter device was $\sim 2000 \mu\text{m}^2$.

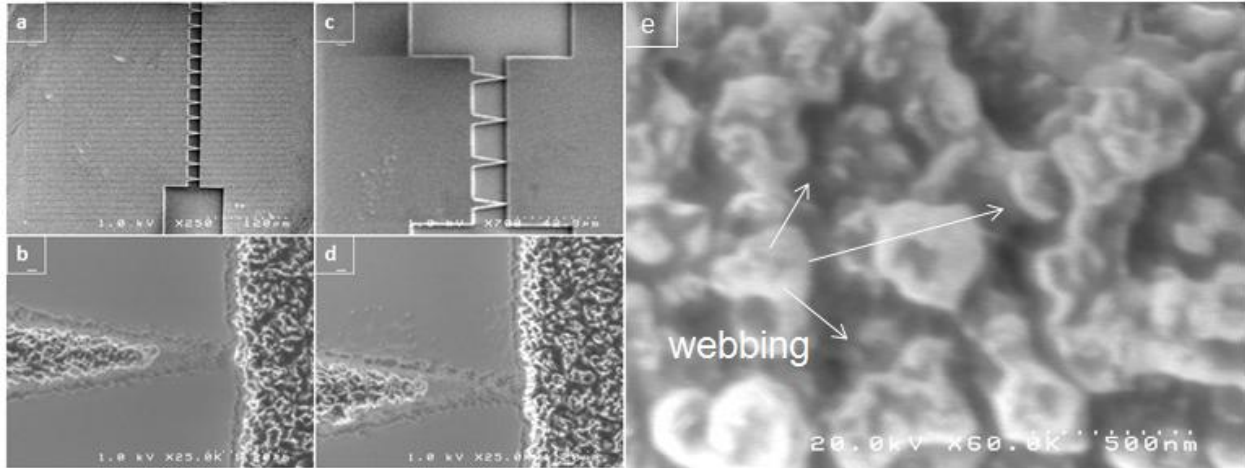


Figure 5.8. SEM image pairs of the 12-emitter tip configuration are shown in images a) through b) and images c) through d) show the delineation results for the 4-emitter tip configuration. Both devices have a measured $\sim 1.2 \mu\text{m}$ emission gap. The shading effect surrounding the inter-electrode area is indicative of successful silicon etching used to isolate the nanodiamond structure from the silicon support layer. The indicators in image e) point to connective residue indicative of the polymer by-product known to form from fluorine-based etching.

The surface texture of the devices in Figure 5.8, although successfully isolated from the active silicon layer, no longer resembles any of the nanodiamond film morphology that was reported in Chapter III. The resulting webbing-like, connective residue is indicative of polymer by-products that are typical of fluorine-based etching [86]; CHF_3 is known to promote polymer formation to selectively inhibit etching [89]. The consistency of the indicated areas also closely resembles the PMMA shown in Figures 5.3 and 5.6.

5.2.2 Device Characterization of the fluorine-based O_2 diamond etched lateral devices

The I - E characteristics of the 4- and 12- emitter lateral devices are shown in Figure 5.9. The turn-on field, as indicated by the value corresponding with 10 nA per emitter, was $\sim 63 \text{ V}/\mu\text{m}$

and ~ 67 V/ μm , respectively for the 4- and 12- emitter configurations; both values are higher than the reported 1.95 V/ μm for a 3 μm gap, 6-emitter nanodiamond lateral diode [6]. As the field strength increased, the I - E characteristics for the two devices became increasingly distinct. For comparison, the normalized current/tip at ~ 40 V/ μm was 0.022 μA (0.005 $\mu\text{A}/\text{tip}$) and 0.014 μA (0.001 $\mu\text{A}/\text{tip}$), respectively for the 4- and 12-emitter configurations. The electron field emission characteristics of intended EBL-designed nanodiamond lateral diodes will become clearer in the studies that follow.

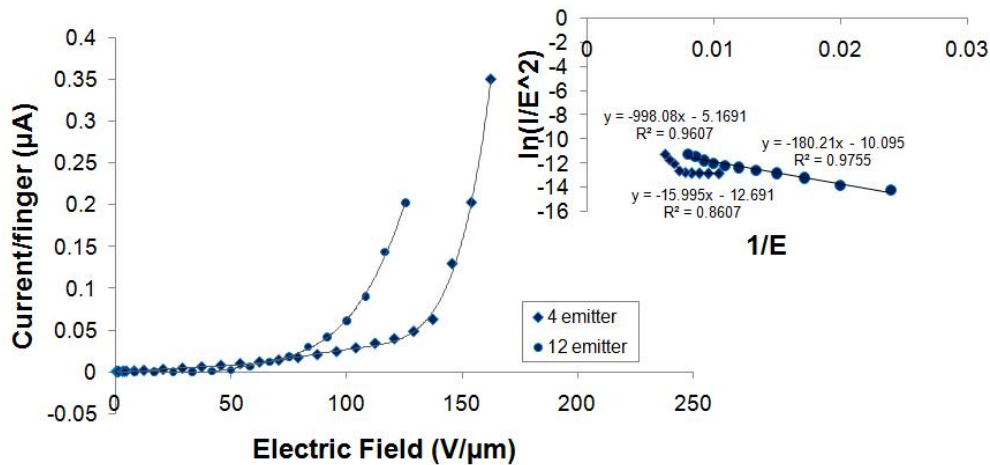


Figure 5.9. The I - E characteristics of 4-emitter and 12-emitter lateral devices with diamond etch performed using an 8:1 ratio of CHF_3 and O_2 gas.

5.2.3 Summary

The outcome of this study emphasizes the importance of identifying the appropriate etch conditions for selectively removing nanodiamond for to isolate EBL-designed lateral diode structures. Using 8:1 CHF_3/O_2 for diamond etching is not advised since the recipe did not successfully isolate the electrodes while maintaining nanodiamond features; the low normalized current/tip and high effective work function indicate a rendered non-diamond emitter material. Nonetheless, this study demonstrated the feasibility of EBL. The field emission results are not

conclusive due to the marked change in the nanodiamond features from films that were reported in Chapter III. The next section explores diamond etching using O₂ -only gas, resulting in the successful delineation of nanodiamond cathode and anode structures.

5.3 Demonstration of EBL-designed nanodiamond lateral device field emission diode fabrication (mixed lithography approach)

The motivation for the work reported in this section was to investigate the impact of using a thinner diamond film, ~1 μm, on EBL-designed lateral field emission device applications. Thicker films, ~2 μm, are compatible with optical lithography and have been used for previous lateral device work [59 and 90]. A fabrication process was developed and implemented for the EBL-micropatterning of a lateral diode design on nanodiamond film. First, a ~1 μm thick nanodiamond film was grown on a SOI wafer comprised of a 2 μm active Si, 4 μm buried oxide, and 525 μm substrate Si. Then, a ~400 nm thick aluminum masking layer was deposited onto the nanodiamond film. Since EBL writing is a relatively slower patterning process, single-mask conventional lithography was used to delineate the contact pads for both the anode and cathode structures on the photoresist-coated aluminum mask. EBL was then used to delineate the device structure on the PMMA-coated aluminum.

Reactive ion etching is the preferred dry etching technology for this research. Aluminum RIE was performed using a PlasmaTherm SLR RIE followed by diamond etching using O₂ gas in STS Advanced Oxide Etch (AOE) equipment. The coil R. F. power was 600 W while the platen R.F. power was 100 W, with oxygen flowing at 30 sccm at a pressure of 10 mTorr. The final step was silicon etch in order to properly isolate the nanodiamond lateral emitters. The active Si layer was removed from the active device area using a fluorine-based RIE system in SF₆/O₂ followed by a Piranha clean.

5.3.1 Fabrication Results

Electron emission from the lateral device was measured in a vacuum maintained under 10^{-7} Torr. The I - V behavior of the device, from which the field emission behavior is derived, was also subject to stability over time emission test. The left inset of Figure 5.10 shows the relative diamond etching rates of the lateral diode critical area and the surrounding larger structures. The scale of the diode in relation to the contact pads is put in perspective when viewing at $30\times$ magnification. The right inset of Figure 5.10 shows the device isolation achieved after the silicon etch. The measured anode-cathode spacing is $\sim 1.8\ \mu\text{m}$. The image observed at $6\times$ provides a full view of the ultra sharp apexes and the emission gap distance. The overall smooth surface morphology of the diamond film can also be seen from the same SEM image. Liou et al. reported using argon-incorporated nanodiamond as their emitter material [79] as opposed to nitrogen-incorporated nanodiamond; their lateral emitters were not as clearly delineated as the devices that are reported in this work. The nanodiamond dry etch rate was 2 nm/second and the aluminum dry etch rate was determined to be 10 nm/second. The $\sim 400\ \text{nm}$ Al layer was therefore the appropriate thickness to retain characteristic features of the lateral diode defined on a $\sim 1\ \mu\text{m}$ thick nanodiamond film.

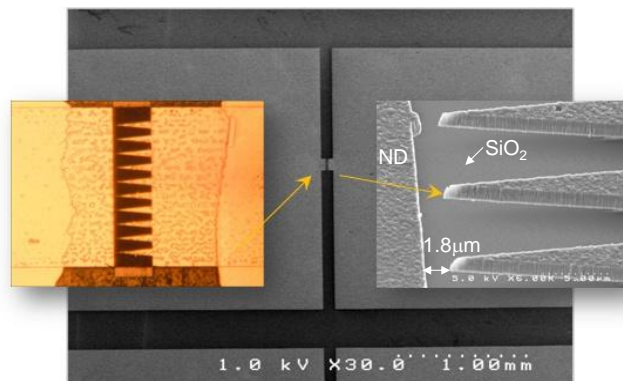


Figure 5.10. Background: SEM of diode structure with 2mm contact pads. The left inset is an optical image of the diode during the nanodiamond etch process. The right inset is the final device delineation showing a $\sim 1.8\ \mu\text{m}$ cathode-anode distance.

5.3.2 Field Emission Characterization

Figure 5.11 presents the I - V and field emission characteristics of the EBL-delineated nanodiamond lateral diode. The F-N plot included in Figure 5.11 suggests F-N tunneling occurs at $V > 25$ V. The I - V behavior is further discussed in section 5.5.

The F-N slope of the forward bias condition is shallower than the reverse bias and this can be attributed to the distinct difference between the anode and cathode geometry. Assuming the ~ 0.6 eV work function for the nitrogen-incorporated nanodiamond film reported in Chapter III, the β factors for the cathode and anode are 244 and 106, respectively; $\beta_{\text{tip}}/\beta_{\text{anode}} \sim 2.3$. As shown in Figure 5.12, the emission current for the $1.8 \mu\text{m}$ anode-cathode gap is observed to be stable over time at $\sim 1 \mu\text{A}$; the data was collected in 1 second intervals over a 1 hour period.

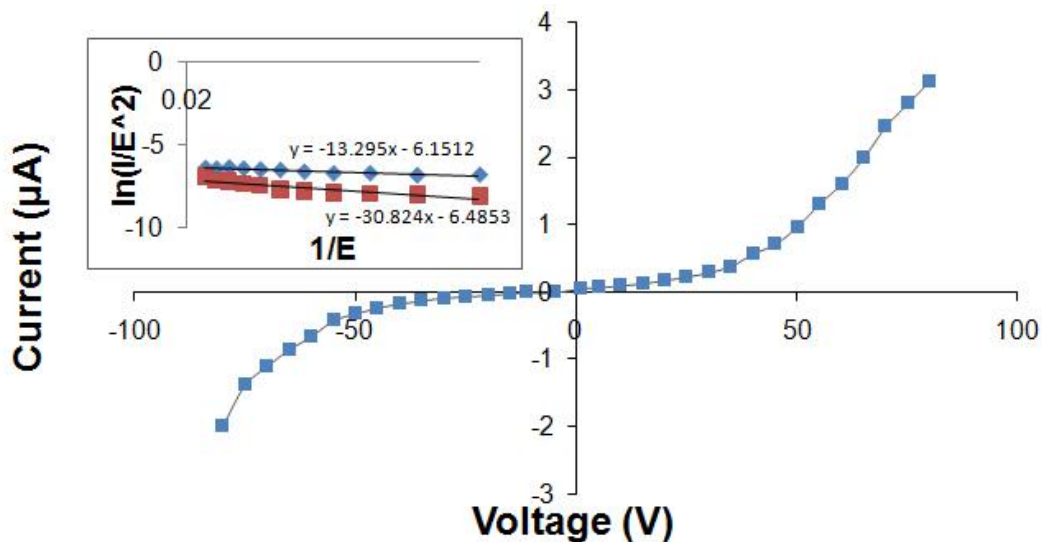


Figure 5.11. The I - V plot of the 10-finger lateral diode with $\sim 1.8 \mu\text{m}$ anode-cathode spacing is shown. The inset shows F-N conformance for the forward (blue) and reverse bias (red) data.

5.3.3 Summary

The incorporation of electron beam lithography into the fabrication of nanodiamond planar lateral field emitters was successfully demonstrated using the mixed lithography approach. Since the use of EBL required a thinner nanodiamond film, it was necessary to

investigate whether a thinner diamond film would sacrifice field emission behavior. The anode-cathode emission gap was reduced by integrating EBL into the fabrication process, however the ~30 V turn-on is higher than the reported 9 V using a 4 μm emission gap nanodiamond lateral diode device with a β value of ~1300 [80]. The I - V characteristic may also reveal leakage behavior, as determined by the measurable emission current observed under reverse bias. The next two studies are aimed towards further understanding the lateral diode device behavior by scaling the emission gap into the sub-micron regime and also by simplifying the fabrication process to reduce possible contamination from cross-processing.

5.4 The effect of 350 nm gap, 3- and 12- emitter tip density on threshold voltage

It is well known that electron field emission can be enhanced by protruding emitter geometry. By comparing 3-emitter and 12-emitter sub-micron gap lateral diode configurations, we are able to investigate the effect of scaling tip density on field emission behavior. Although similar to the study in section 5.2, the emission gap is now at the sub-micron scale and the cathode area for both devices is limited to 2000 μm^2 . There is little prior work reported for diamond lateral devices due to the difficulty in realizing device level micron/sub-micron scale diamond patterning [6]. This work developed a nanodiamond processing technology to consistently obtain sub-micron gap lateral field emission devices. The small grain size and relatively smooth surface of the nanodiamond, coupled with its material compatibility with silicon and aluminum, enabled uniform patterning of the thin film, achieving the first ever delineation of sub-micron inter-electrode spacing. Precise lithographically controlled sub-micron spacing would enable a significant reduction in device operating voltages, offering

interesting device performance characteristics such as reduced power operation [6]. A previously unobserved high field emission operating regime will be presented.

5.4.1 Fabrication of 3- and 12- emitter, 350 nm gap devices

In this work, EBL was the sole source of patterning in order to reduce the cross-contamination that occurs from device fabrication. The process is outlined in Figure 5.13 and the sub-micron delineation is shown in Figures 5.13, 5.15, and 5.16. Similar to the OEB approach described in section 5.2, the fabrication begins with the growth of a $\sim 1 \mu\text{m}$ thick nitrogen-incorporated nanodiamond film on a silicon-on-insulator (SOI) wafer ($2 \mu\text{m}$ active Si, $4 \mu\text{m}$ buried oxide (BOX), and a $625 \mu\text{m}$ Si substrate) by $\text{CH}_4/\text{H}_2/\text{N}_2$ MPECVD.

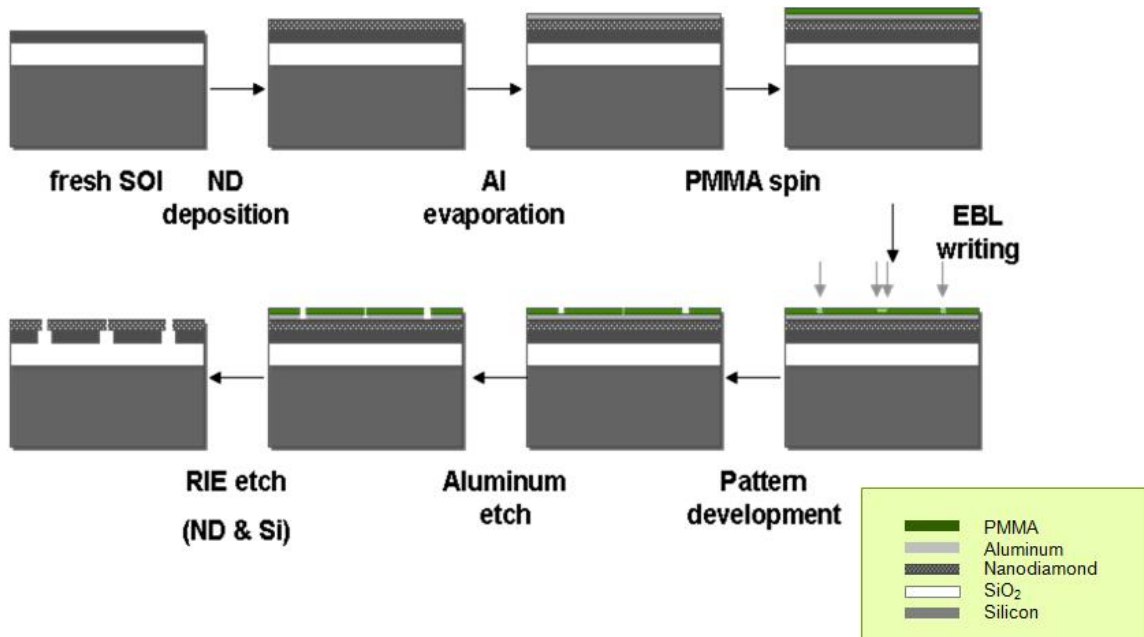


Figure 5.13. Process flow for the single-EBL mask lateral field emission fabrication process.

Following, a $\sim 400 \text{ nm}$ layer of aluminum was thermally evaporated onto the diamond. EBL was used to delineate the contact pads and the lateral structure. Following, aluminum etch was then

performed followed by a series of RIE of the ND and the Si to isolate the diamond anode and cathode. Once the nanodiamond was micro-patterned with the lateral emitter structures, the silicon layer beneath the nanodiamond was deliberately under-cut etched in order to promote the nanodiamond layer gap proximity. Figure 5.14 shows a top view progression of delineation results as the devices undergo the fabrication process. Figures 5.15 and 5.16 show different angle views of ~ 350 nm emission gap, 3-emitter and 12-emitter lateral vacuum field emission diodes.

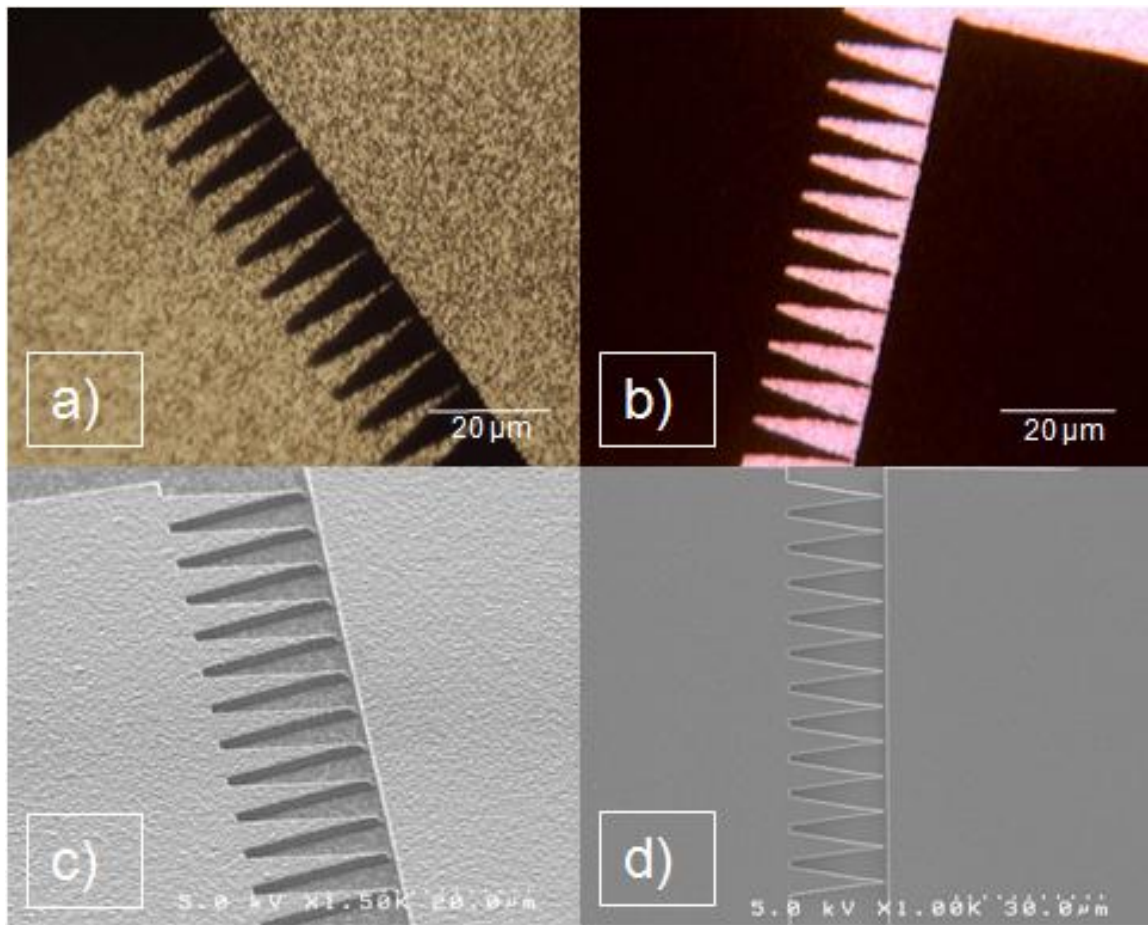


Figure 5.14. Optical and SEM images of the 12-emitter device showing the progression through the series of material removal for device definition: a) Aluminum mask on nanodiamond; b) nanodiamond on Si; c) SEM of nanodiamond on Si; and d) SEM of nanodiamond with Si layer removed.

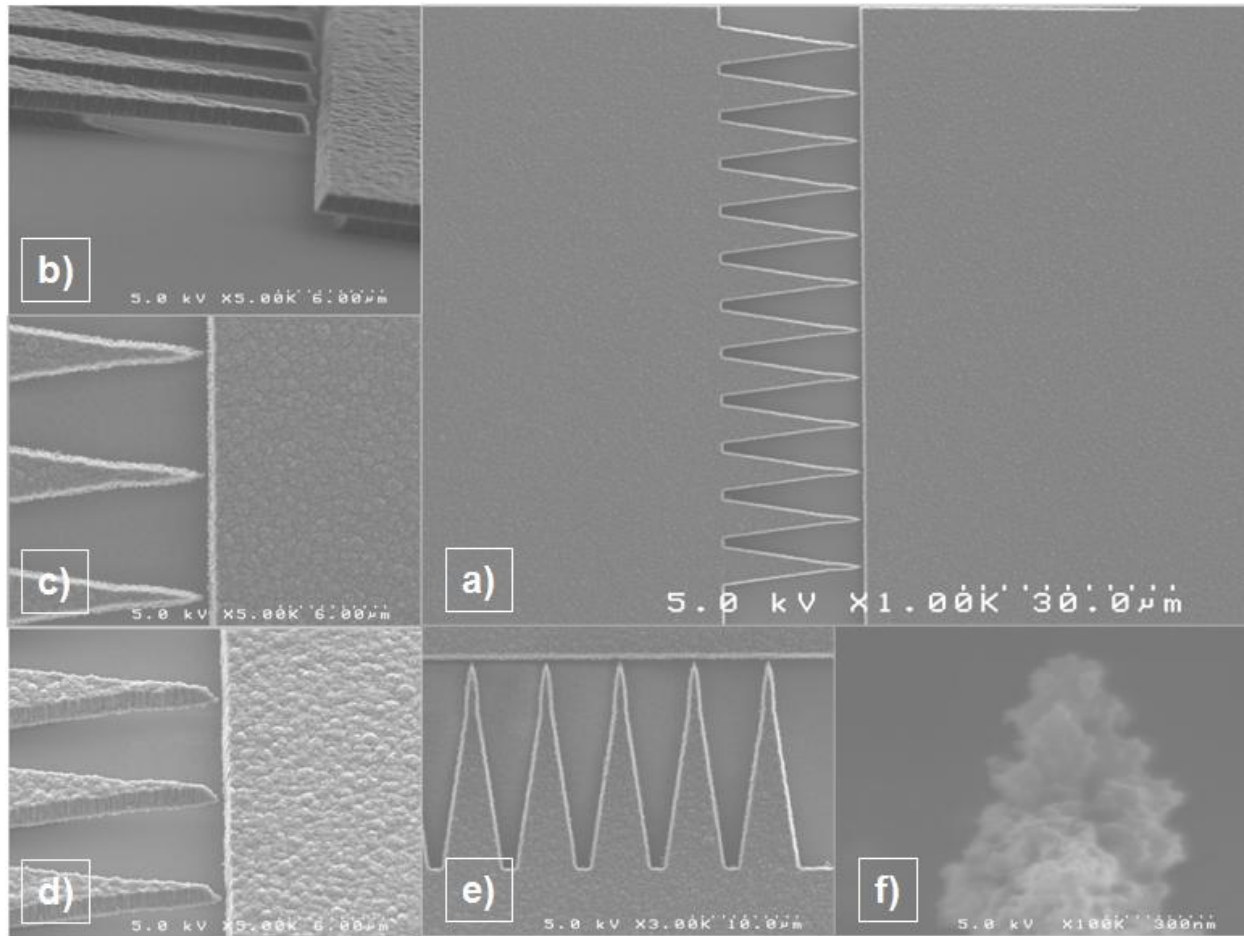


Figure 5.15. a) Uniform delineation of a ~ 350 nm emission gap, 12-emitter lateral vacuum FED; b) side view of the lateral diode showing the Si undercut; c) higher magnification showing the uniformity of the cathode tips; d) side view showing the columnar structure of the diamond emitters; e) and f) the estimated emitter tip radius is 150 nm.

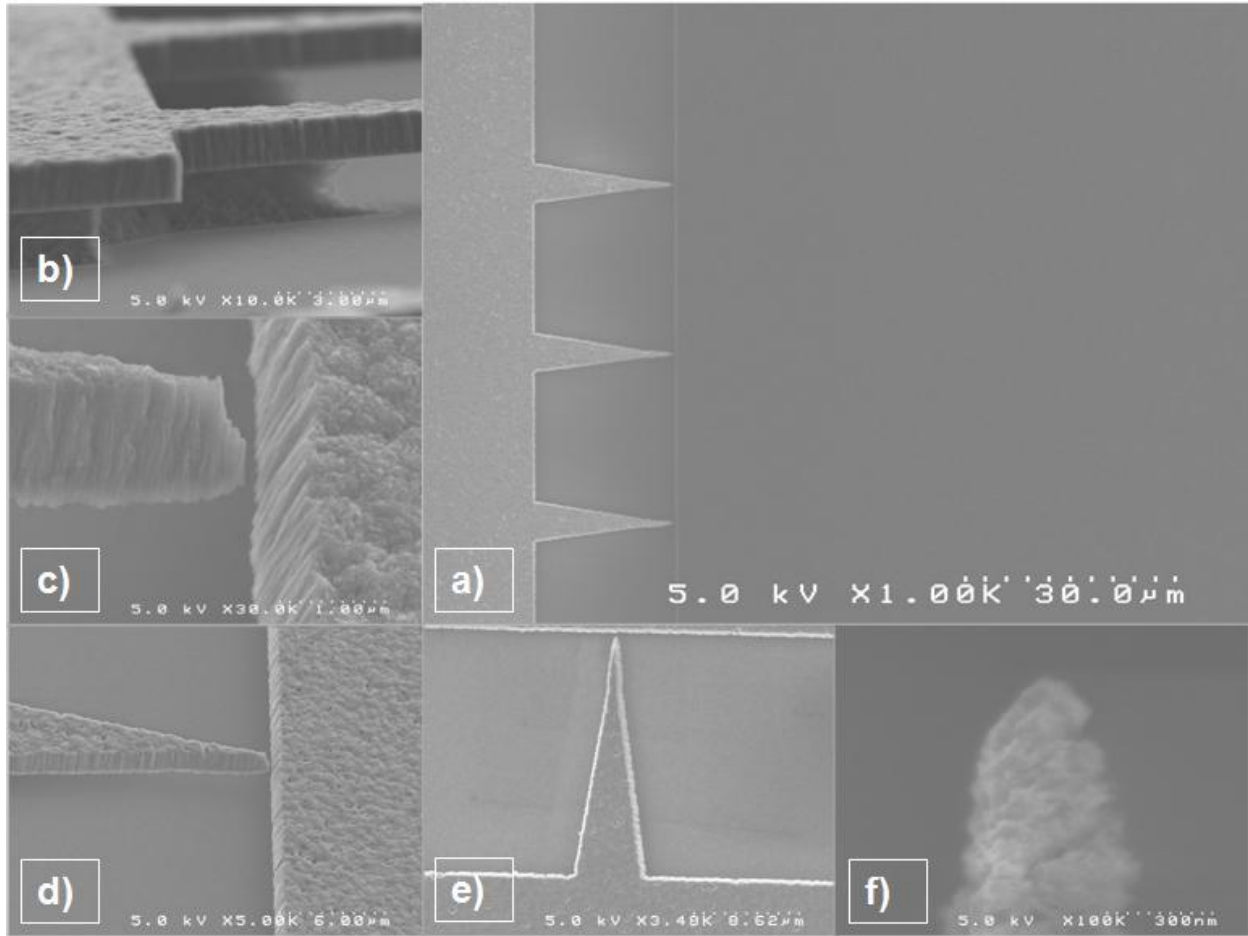


Figure 5.16. a) Uniform delineation of a $<350\text{ nm}$ emission gap, 3-emitter lateral vacuum FED; b) side view of the lateral diode showing the Si undercut; c) and d) higher magnification showing the uniformity of the cathode tips; e) and f) the estimated emitter tip radius is 150 nm .

5.4.2 Device Characterization of the 3- and 12- emitter, 350 nm gap devices

Prior to emission characterization the devices were subject to in-situ vacuum thermal and electrical tip conditioning in vacuum at 100°C and 1-10 μ A for ~1 hour or more until a stable current was obtained. The extracted field emission current was used to execute a more localized cleaning of the nanodiamond emitter tips [6]. During testing, the voltage is cycled to obtain a stable and reproducible current-voltage response [47]. The *I-V* characteristics for the devices taken after the stabilizing thermal and electrical conditioning are given in Figure 5.17.

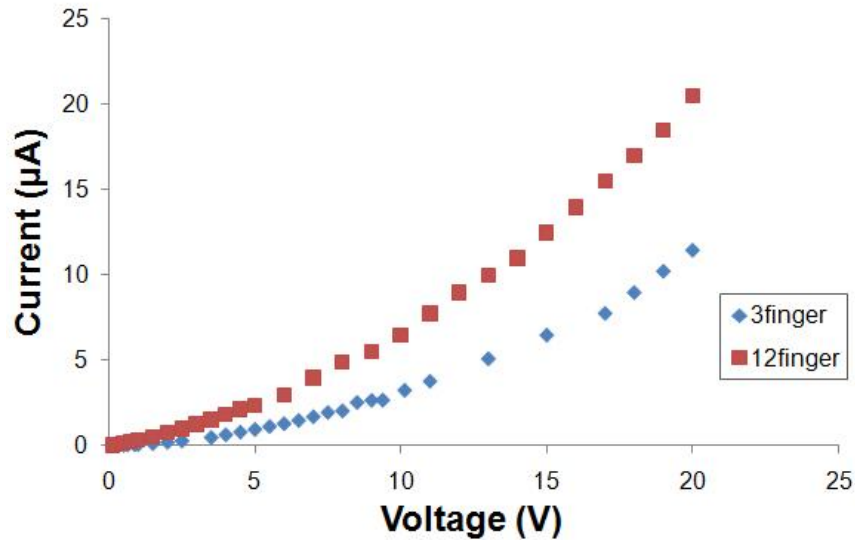


Figure 5.17. Current-voltage results for the 3- and 12-emitter sub-micron (~350 nm) gap lateral vacuum devices are shown. Notable characteristics: at 1.42 V/ μ m (0.5 V) the emission current is 35 nA and 164 nA and at 40V/ μ m (16V), the emission current is 7.8 μ A and 14 μ A for the sub-micron 3- and 12-emitter configurations, both respectively.

Figure 5.18 shows deviation from Fowler-Nordheim tunneling behavior. This behavior suggests that a different conduction mechanism is occurring in these devices. The cathode current may be following leakage paths in the supporting oxide layer as a result of exposure to RIE, (See discussion in section 5.4.3.). As will be discussed next, we overcame the oxide damage with the devices described in section 5.5 by removing the surface damage.

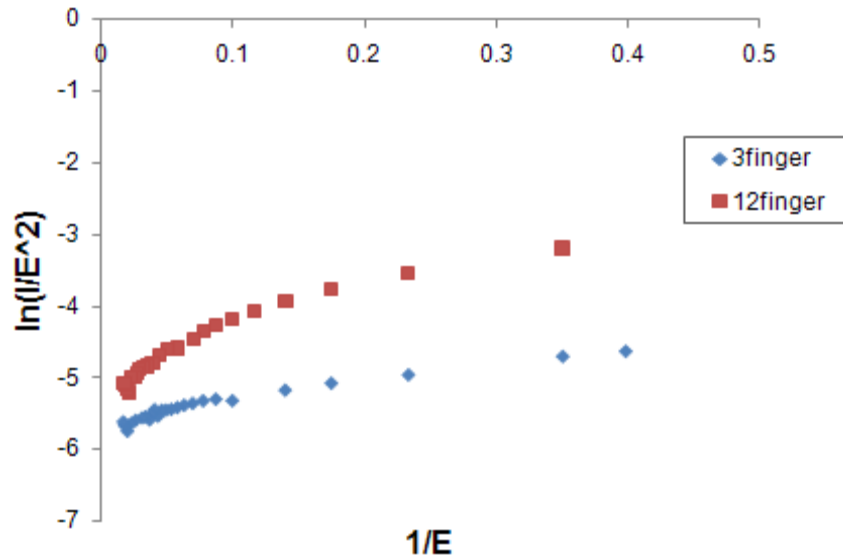
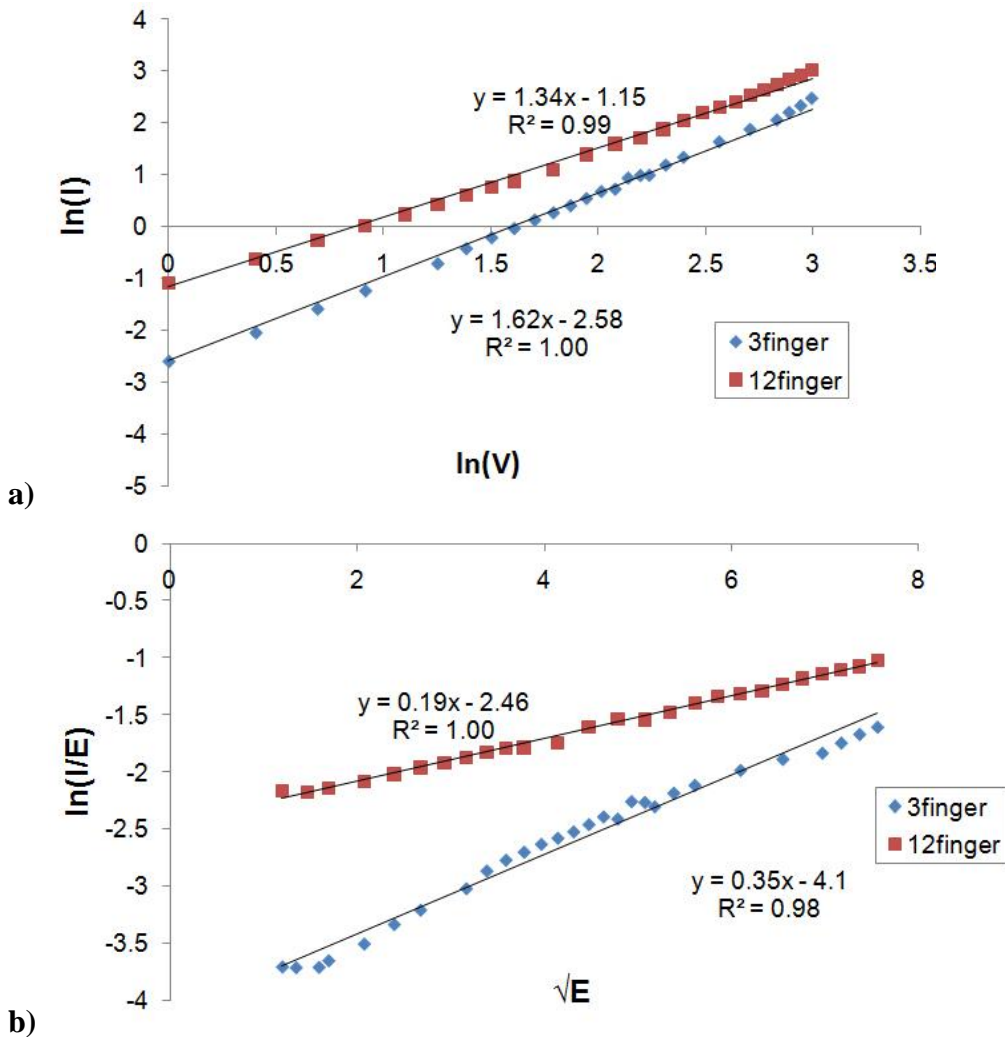


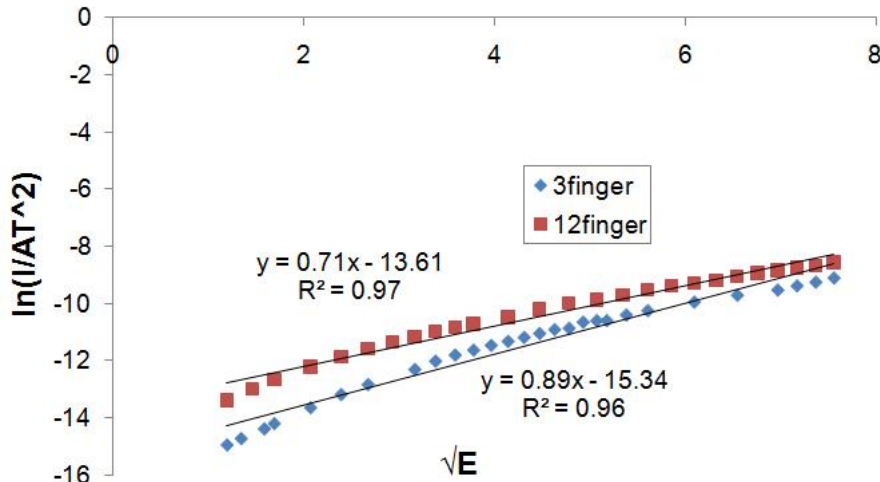
Figure 5.18. Corresponding F-N plot.

5.4.3 Discussion

For films that are intrinsically electrical insulators, such as silicon dioxide, Frenkel-Poole conduction mechanism can describe electrical leakage, especially in circumstances where process damage from, for example, reactive ion etching may arise as a part of the processing procedures. RIE effects such as lattice damage are well known [90] whereby insulating surfaces or layers may become less insulative. Examining the data from the lateral devices, while considering the potential occurrence of all possible conduction mechanisms, can better describe the electrical behavior of these sub-micron gap devices. Figure 5.19 shows the current-voltage behavior examined as SCLC, Frenkel-Poole, and FTE conduction models, as described in Chapter II. For this specific set of devices, the conduction mechanism that most closely fits the device data is the Poole-Frenkel model shown in Figure 5.19 b). Poole-Frenkel conduction involves a significant number of defect or impurity sites within the insulator; such a condition may very well exist within the oxide of the samples due to the RIE process. Further, if the sites

are sufficiently close together, under applied electric field the carriers are able to “hop” from one site to another [26]. If the defect sites are too far apart, the hopping mechanism becomes rate limited; the Poole–Frenkel current can become space-charge limited [26]. It is deduced as probable that contribution to the anode current from Frenkel-Poole mechanism, as observed in these 350- nm gap devices, arise from conduction in the oxide surface. Figure 5.20 shows evidence of damage to the oxide layer.





c)

Figure 5.19. a) SCLC conformance indicates space charge build up at emitter tips; b) Frenkel-Poole conduction indicates electron “hopping” from the proposed structural changes in the oxide surface and c) FTE from the sp^2 - sp^3 - sp^2 emitter tip structure would indicate a lowered potential barrier to vacuum emission.

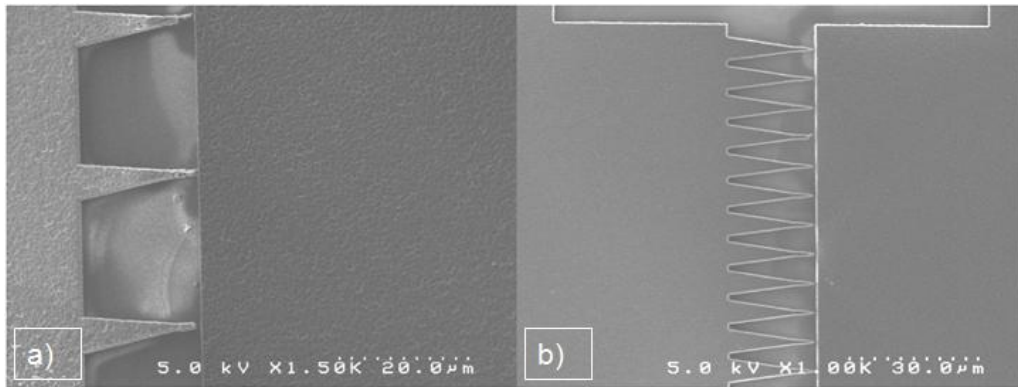


Figure 5.20. SEM images a) and b) of the 3- and 12- emitter devices captured after testing show damage to oxide and emitter tips.

5.4.4 Summary

A process was developed to consistently achieve sub-micron anode-cathode emission gap delineation. EBL was used as the sole method for device patterning in order to mitigate the introduction of impurities from cross-processing, proving helpful towards achieving the ~ 350 nm inter-electrode spacing for a pair of 3- and 12- lateral emitter lateral diodes. Prior to

characterization, the devices were subjected to prolonged concurrent thermal and electrical conditioning.

The conduction mechanism for the sub-micron devices showed the supporting oxide layer, as evidenced by the physical damage to the cathode emitter tips and the oxide surface due to RIE. A follow-up study in Section 5.5 involving the removal of surface oxide damage and the scaling of the lateral device emission gap inter-electrode distance to the sub-micron regime was conducted next to further understand the device conduction mechanisms.

5.5 Sub-micron gap field emission performance as a function of emission gap distance:

In this section, three 10-finger nanodiamond lateral emitter diode configurations with scaled emission gaps are fabricated and tested.

5.5.1 Fabrication results of EBL-delineated lateral diodes with variable emission gap

The design parameters, e.g. the emitter geometry, size, and inter-electrode spacing were software-defined and transferred onto the nanodiamond film by EBL. The devices were processed as described in section 5.4.1. The physical structure of the nanodiamond lateral diodes with 500 nm, 850 nm, and 1.5 μm inter-electrode distances were examined using scanning electron microscopy, shown in Figure 5.21. All three devices have uniformly defined emitter tips.

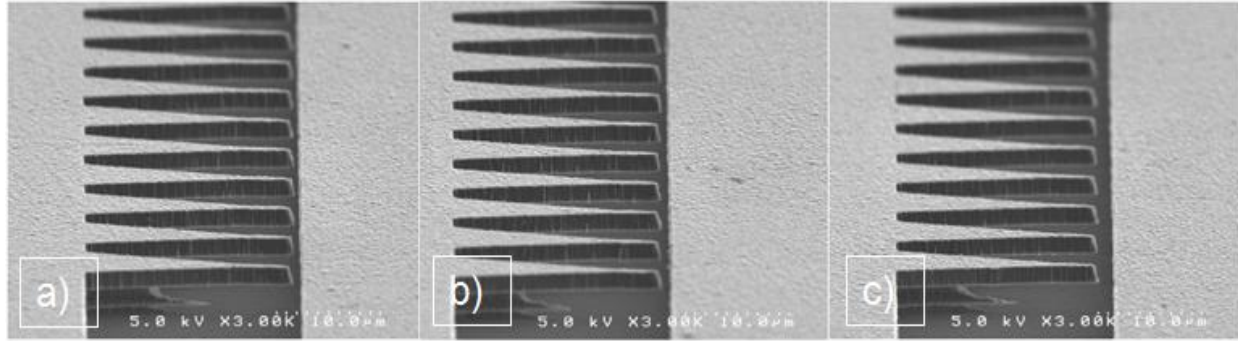


Figure 5.21. SEM of a) 500 nm b) 850 nm, and c) 1.5 μm gap configurations.

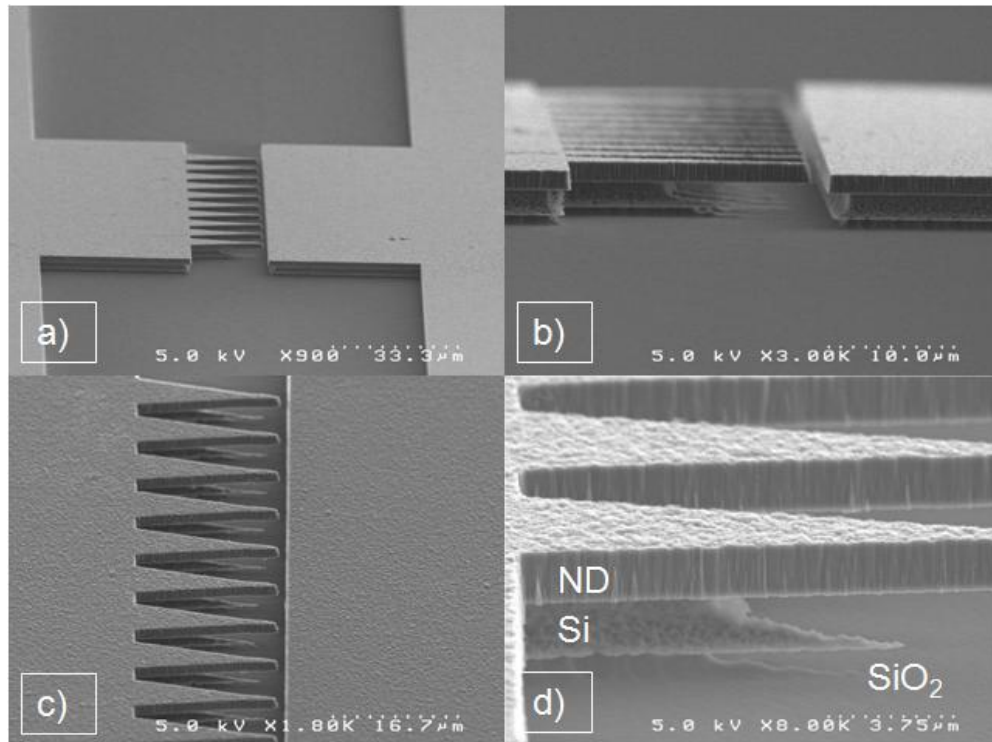


Figure 5.22. Images a)-d) show various views of the lateral device delineation with oxide removal. The SEM in d) highlights the deliberate removal of oxide top layer.

5.5.2 Conditioning process for 500 nm, 850 nm, and 1.5 μm gap diodes

To ensure the cleanliness of the devices, the nanodiamond lateral diodes were subjected to wet chemical cleaning and electrical conditioning. Buffered oxide etch (BOE) was used to remove a $\sim 0.5 \mu\text{m}$ thick layer of SiO_2 in order to extricate surface contaminants or defects from process induced damage that may be present on the oxide. The silicon wafer industry's standard

RCA chemical cleaning procedure was also used to clean the device surface prior to vacuum chamber test set-up. Thermal and electrical conditioning were performed separately; only heating was used prior to characterizing the devices. The field emission behavior of the three diodes was individually characterized under vacuum of 10^{-7} Torr.

5.5.3 Field emission characterization of 500 nm, 850 nm, and 1.5 μm gap devices

a) $E < 20\text{V}/\mu\text{m}$

At fields below $20\text{V}/\mu\text{m}$, all three devices exhibited Fowler-Nordheim behavior. It was reported in previous nanodiamond lateral field emission device work that at lower electric fields, anode current arises from cathode tip electron tunneling emission [6].

Figure 5.23 portrays the overall I - V and I - E characteristics of the three lateral devices. The turn-on voltage and corresponding turn-on field for these devices is defined as the value corresponding to 0.1 nA. Proportional to turn on voltages of 0.5, 0.9, and 1.4 V all three diodes exhibited a turn on field of $\sim 1\text{ V}/\mu\text{m}$. Figure 5.24 highlights the low-voltage characteristics of the devices. The F-N scale shown in Figure 5.25 b), derived from the I - E characteristics shown in Figure 5.25 a), shows all three devices exhibiting Fowler-Nordheim tunneling behavior in the $E < 20\text{ V}/\mu\text{m}$ region. With the F-N slope proportional to $\phi^{3/2}/\beta$, the offset seen by the $1.5\mu\text{m}$ gap configuration is attributed to the geometry.

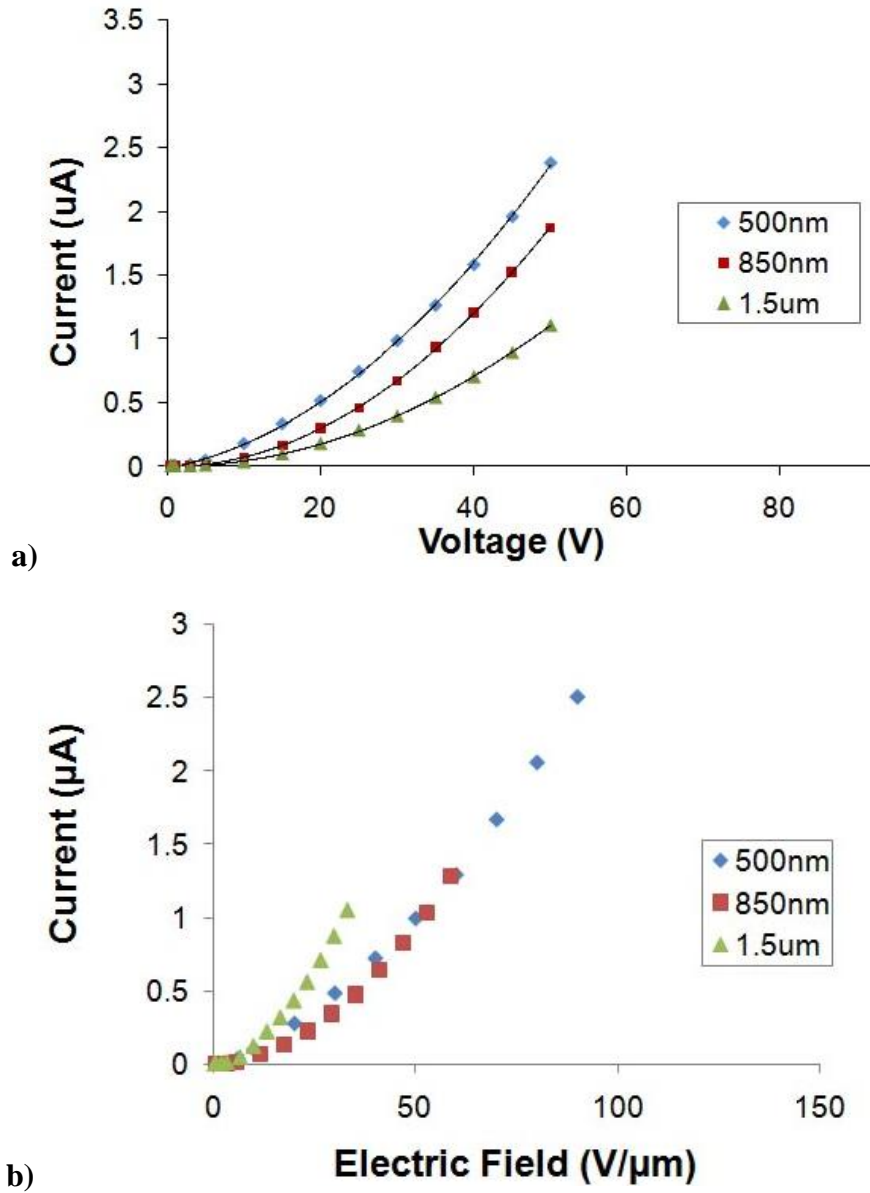


Figure 5.23. a) Complete *I-V* for the three devices and b) corresponding *I-E* characteristics.

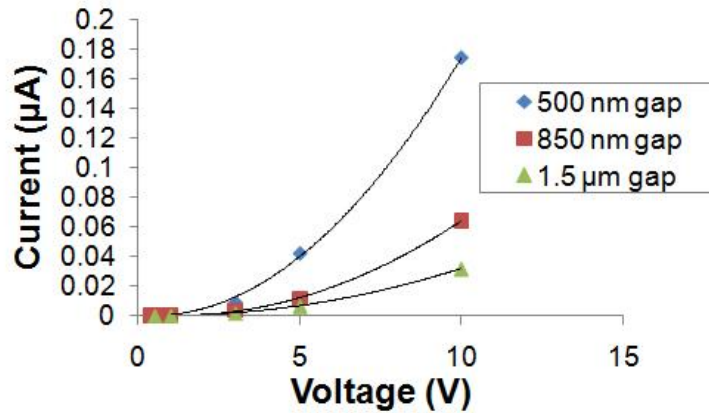


Figure 5.24. Low voltage I - V for the three diodes with different emitter gap configurations. The turn-on voltage for the 500 nm, 850 nm, and 1.5 μm gap configurations are 0.5 V, 0.9 V, and 1.4 V, respectively.

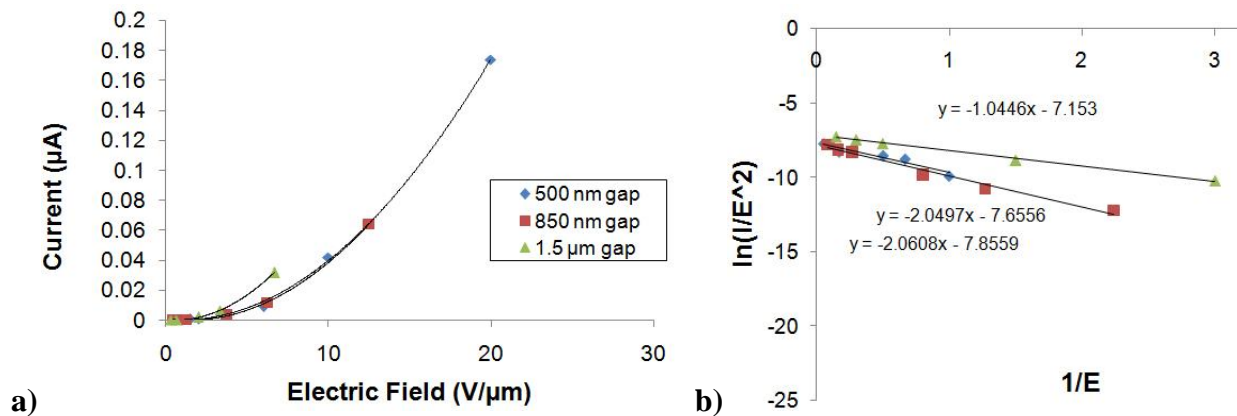
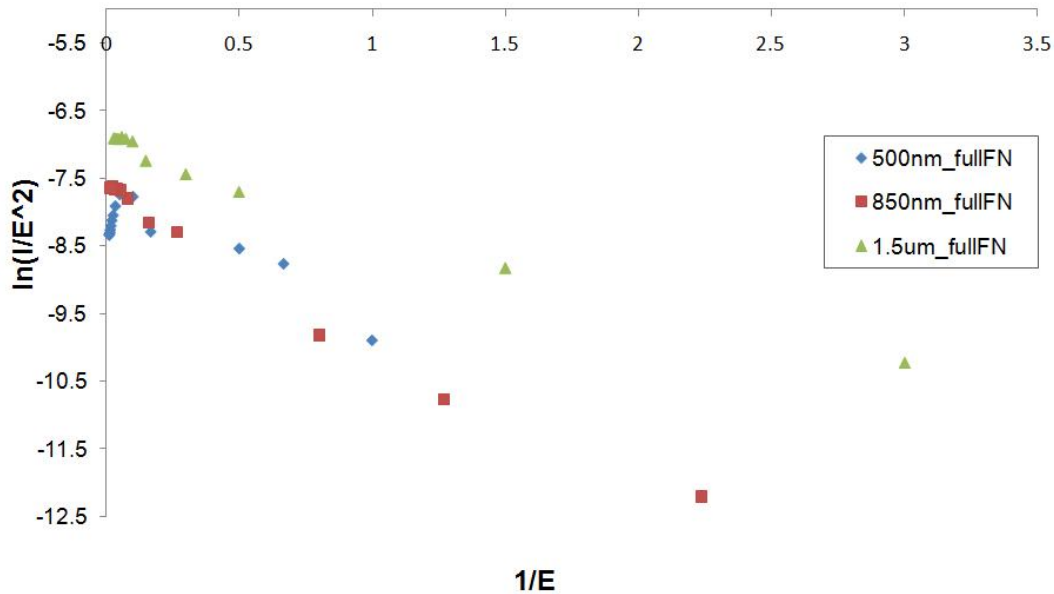


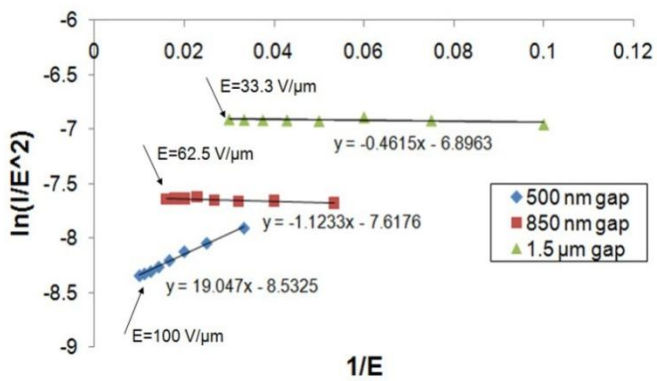
Figure 5.25. I - E characteristics and corresponding F-N behavior of the lateral vacuum diodes are shown in a) and b). Figure a) shows the I - E for $E < 20 \text{ V}/\mu\text{m}$ and the corresponding F-N conformance is presented in b). With the F-N slope proportional to $\phi^{3/2}/\beta$, the offset seen by the 1.5 μm gap is due to geometric differences.

b) $E > 20 \text{ V}/\mu\text{m}$ region

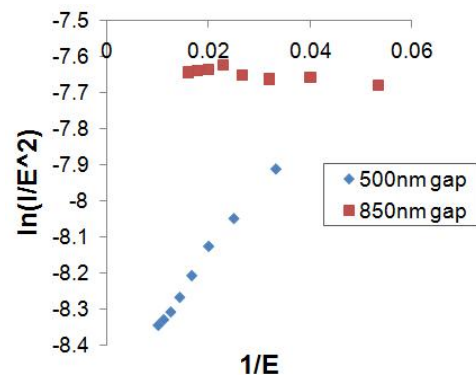
Figure 5.26 a) shows the entire data set portrayed on a F-N plot. Both the 500 nm and 850 nm gap devices exhibited deviation from F-N as they experienced an increasing field. The 500 nm gap device began to exhibit deviation at $\sim 10 \text{ V}/\mu\text{m}$ but more distinctly by $20 \text{ V}/\mu\text{m}$, while the transition for the 850 nm gap device was $\sim 12.5 \text{ V}/\mu\text{m}$.



a)



b)



c)

Figure 5.26. a) Full $F-N$ characterization of the three devices. The deviation from $F-N$ at $E > 20 \text{ V}/\mu\text{m}$ seen by the 500 nm and 850 nm gap devices is more clearly seen in b) and c).

The deviation from the tunneling mechanism at higher fields may be due to SCLC and FTE as a result of the Schottky barrier lowering that was described in Chapter II. Electron emission mechanisms and SCLC are complementary [6]; a space charge layer may arise from charge injection through a low potential barrier. It can be clearly seen in Figure 5.26 b) and c) that the 500 nm and 850 nm gap devices deviate from $F-N$ behavior at the higher field values, indicating that different conduction mechanisms may arise as the field increases. It is further

noted that only in the sub-micron gap devices were we able to achieve these high fields at the cathode, a condition not possible with wider gaps because there would be substrate oxide failure before those levels of electric field could be reached.

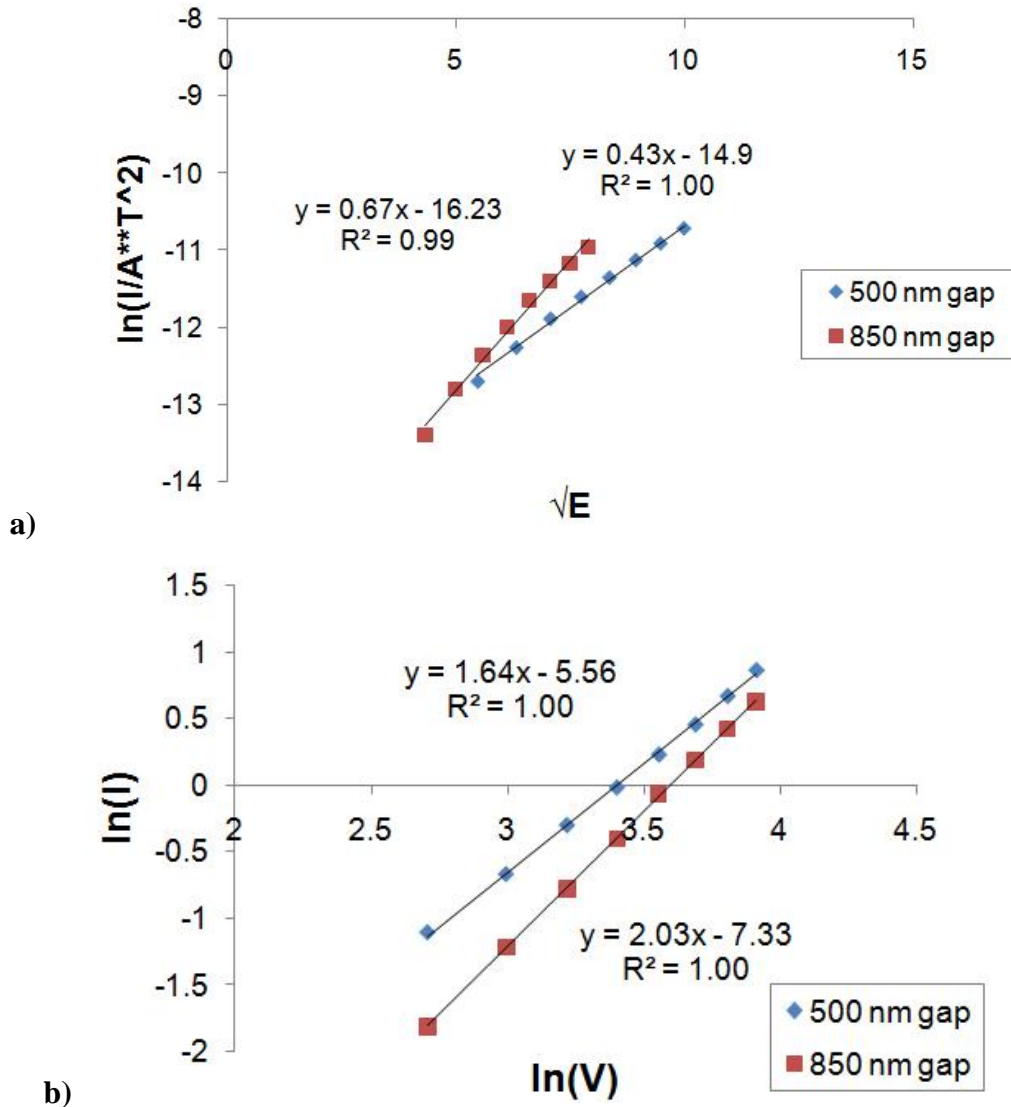


Figure 5.27. Both the 500 nm and 850 nm gap devices show conformance to the a) field-enhanced thermionic model and b) SCLC for device data $E > 20\text{V}/\mu\text{m}$.

Based on the FTE model presented in Table 2.1 of Chapter II, the barrier height estimated from the curve fit in Figure 5.27 is $\sim 0.38\text{ V}$ and $\sim 0.42\text{ V}$, respectively for both the 500 nm and 850 nm gap devices. The experimental potential barrier values are comparable to the theoretical

values ~ 0.38 V and ~ 0.66 V, reported in Appendix B. Field-enhanced thermionic emission is attributed to high field strength that was achievable through the sub-micron configuration. As a result of this study, it becomes more apparent that multiple conduction mechanisms may overlap as the field changes. The 500 nm and 850 nm gap lateral devices show deviation from F-N at increasing fields that may be attributed to FTE. The transition from F-N behavior to FTE would explain the nonlinear trend of the emission current as the emission gap is scaled down from 1.5 μm to 500 nm, shown in Figure 5.28.

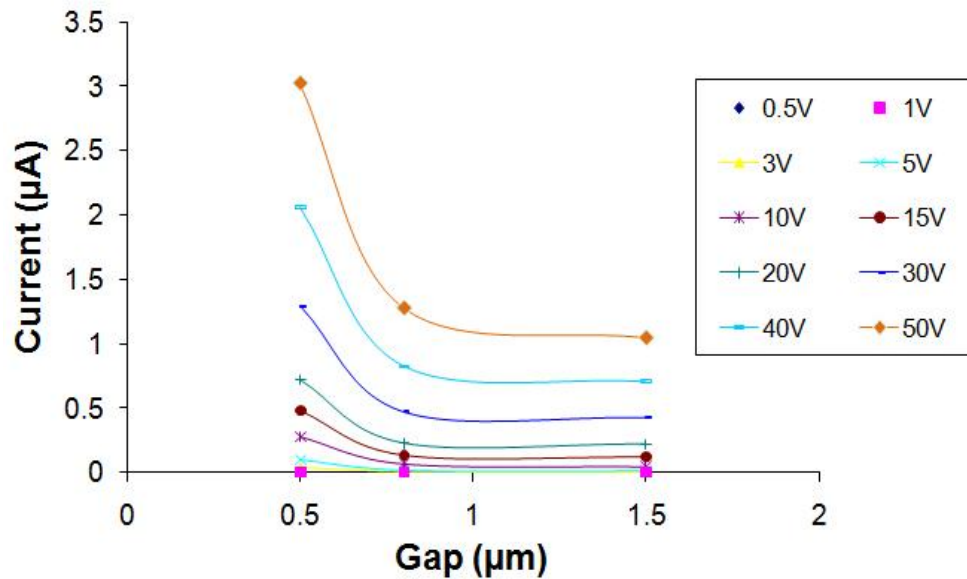


Figure 5.28. Current as a function of lateral emission gap at a constant voltage.

5.5.4 Summary

The effect of inter-electrode spacing into the sub-micron regime on electron field emission behavior was investigated using 500 nm, 850 nm, and 1.5 μm emission gap lateral device configurations. The three lateral nanodiamond vacuum microelectronic diode device configurations were used to examine low voltage operating conditions and are observed to exhibit Fowler-Nordheim emission from ~ 10 V down to ~ 0.5 V. From these devices, all of the same film, we were able to study the overall trend in device performance as the inter-electrode

distance was scaled into the sub-micron regime. Interestingly, it was observed that emission behavior not strictly F-N in nature occurred. By $E > 20\text{V}/\mu\text{m}$, the conduction mechanism in both the 500 nm and 850 nm gap devices deviated from F-N tunneling. It was shown that at increasing fields corresponding to $E > 20\text{ V}/\mu\text{m}$ the sub-micron gap device conditions resulted in the 500 nm and 850 nm gap diodes conforming to the SCLC conduction and field-enhanced thermionic emission mechanisms.

CHAPTER VI

CONCLUSIONS AND RECOMMENDATIONS

The sub-micron gap nanodiamond lateral emitter diode configuration provides a versatile construct for achieving a complete low-voltage operating field emission device. This thesis focuses on the experimental study of the underlying conduction mechanisms of nitrogen-incorporated CVD nanodiamond and the fabrication of sub-micron gap delineated lateral field emission diode devices with varying cathode designs. A procedure was developed first for optimizing the physical and electrical properties of nanodiamond film to permit low field emission and physical compatibility with EBL and subsequent device processing. Two processes were developed for incorporating EBL into the design and fabrication of lateral sub-micron emission gap configurations. In Chapter III we reported the successful fabrication of uniformly smooth and conductive nanodiamond films with grain sizes as small as ~10 nm. Finally, in Chapter V, a repeatable EBL-integrated fabrication process was presented for achieving sub-volt turn on, sub-micron gap lateral vacuum field emission devices in diode configuration. In this chapter, the findings from the reported experiments are summarized followed by recommendations for future studies on sub-micron gap nanodiamond lateral vacuum field emission device technology.

6.1 Continuous nanodiamond film fabrication and characterization

Before arriving at a conductive nanodiamond film substrate that would be compatible with EBL and subsequent device processing, two different studies were conducted in order to thoroughly investigate principle control parameters that influence the physical and electrical

properties of CVD diamond. The nanodiamond film research presented in Chapter III comprised of proposed hybridized conduction models that enable low field emission from nitrogen incorporated diamond films and study conclusions that related field emission characteristics to electron binding energy and changes in sp^2/sp^3 composition across different diamond films.

Many researchers [5-6, 63, 44, and 65] concur on the necessity of hybrid nanostructures for achieving low field emission. The proposed conduction mechanisms closely resemble the MIM and hot electron emission models that were reported by Wisitsorat-at, Xu, and Latham [1, 5]. A cascaded $sp^2-sp^3-sp^2$ structure effectively forms overlapping conduction channels that connect surface regions, thereby improving the electron transport mechanism through the diamond bulk to emitter vacuum surface.

A three-film study that was presented in section 3.4 studied the influence of hybridized sp^2 and sp^3 bonding on macroscopic field emission characteristics and concluded that a film with a relatively high sp^2 -bonded carbon content also correlated with low electron binding energy, a condition that is favorable for emission into vacuum. A nitrogenated, low growth-rate film that possessed the relatively highest sp^2 -bonded content and lowest binding energy also exhibited the shallowest F-N slope, which is indicative of a reduced effective work function. With low electron binding energy and a low surface work function, a nitrogenated nanodiamond film would be a promising substrate configuration for deriving sub-micron gap lateral devices. In comparison to an undoped nanodiamond film with a turn-on field at ~ 5.75 V/ μm , a nitrogen-incorporated nanodiamond film that exhibited a turn-on field at ~ 3.5 V/ μm would result in a ~ 2.3 V/ μm field reduction. The corresponding effective work function values were estimated to change from ~ 1.8 eV to ~ 0.6 eV.

A follow-up five-film study expanded upon the three-film study to include the sensitivity of nanodiamond film composition to nucleation seeding preparation. Additionally, Micro-Raman spectroscopy was introduced as an alternative tool for monitoring changes in graphite and diamond content across different diamond film configurations. Bias-enhanced nucleation absolves the use of physical abrasive means to create nucleation sites for diamond deposition however, if used correctly mechanical polishing would still produce useful nanodiamond films. As reported in section 3.5, using BEN resulted in an increased volume of grain boundaries. Coupled with nitrogen incorporated low growth-rate conditions, a BEN film was shown to exhibit a turn-on field at ~ 3.3 V/ μm , which is slightly lower than the ~ 3.5 V/ μm turn-on field for the mechanically polished alternative that was reported in section 3.4. The work function for the BEN, nitrogenated nanodiamond film was also a ~ 0.6 eV work function, the same value reported for its diamond seeded counterpart. Raman spectroscopy analysis was performed on all five films and the results consistently showed that nanodiamond films that were characterized by decreasingly smaller grain sizes exhibited a relatively higher degree of sp^2 -bonded carbon content upon nitrogen incorporation. The diamond films containing the increased levels of sp^2 bonding content, as indicated by both D and G bands, in turn consistently exhibited decreasingly lower turn-on fields.

6.2 The incorporation of EBL into sub-micron gap lateral device technology design and fabrication

Reducing the inter-electrode spacing to the sub-micron range offers new and exciting opportunities for nanodiamond lateral device applications, such as low voltage operation. Upon identifying a conductive, yet smooth nanodiamond film configuration, work was conducted to incorporate electron beam lithography into the design and development of sub-micron gap

nanodiamond lateral device technology. The previously reported work on nanodiamond lateral devices was limited by the resolution capability of traditional optical lithography [6]. New to this research, the incorporation of the 20 nm beam width that is used in EBL enabled much finer and more consistent device patterning results. Two processes were developed for the design and fabrication of EBL-delineated sub-micron gap devices and were described in Chapter V. We were able to report on the successful achievement of sub-micron anode-cathode separation.

6.3 Field emission characteristics of sub-micron gap nanodiamond lateral device technology in diode configuration

High field conditions that are achieved in sub-micron gap devices coupled with an emitter material work function of ~ 0.6 eV provides conditions that allow for different field emission conduction mechanisms to overlap as the field changes. The field emission characteristics of a three lateral diode set with 1.5 μm , 850 nm, and 500 nm gap variations were reported in Chapter V.

An EBL-only patterning method was employed to mitigate the introduction of impurities from cross-processing, proving helpful for achieving ~ 350 nm inter-electrode spacing for 3- and 12- emitter cathode configurations. However, the conduction mechanism is attributed to defect-induced Poole-Frenkel conduction through the SiO_2 layer caused by exposure to RIE, as evidenced by the physical damage to the cathode emitter tips and the oxide surface shown in Figure 5.21.

A comparison between 500 nm, 850 nm, and a 1.5 μm emission gap lateral diode structures revealed a sub-volt turn on as the emission gap was scaled into the sub-micron regime. Below 20 V/ μm , all three devices from this work conformed to F-N. In proportion to turn-on voltages of ~ 0.6 , ~ 0.9 , and ~ 1.4 V, all three diodes exhibited a turn-on field of ~ 1 V/ μm . Both

the 500 nm and 850 nm gap devices exhibited deviation from F-N as they experienced an increasing field in the emission gap. The deviation from the tunneling mechanism at higher fields may indicate SCLC and FTE as a result of Schottky barrier lowering. The space charge layer may arise from the ease of charge injection through a low potential barrier. Based on the FTE model presented in Table 2.1 of Chapter II, the estimated barrier height using the fitted lines in Figure 5.27 for both devices is ~0.38 and ~0.42 V, respectively. The reduced potential barrier to electron emission is attributed to high field strength that was achievable through the sub-micron configuration and the low work function property of the emitter material.

6.4 Recommendations for future work:

EBL is a useful method for achieving sub-micron emission gap delineation. The recipes for successfully and consistently achieving the sub-micron gap have now been developed and demonstrated. The following recommendations are for further improving the sub-micron gap lateral device performance:

- 1) The emission current is sensitive to the number of emitters in the cathode array; continue to increase the emitter tip density using progressively thinner (e.g. 500 nm) diamond film thickness for fine delineation.
- 2) EBL writing is very time consuming; further reduce the electrode area to allow for efficient use of EBL to pattern monolithic designs.
- 3) High grain boundary densities improve field emission performance; increase the volume density of grain boundaries by incorporating argon gas to deposit ultra-nanocrystalline diamond (3-5 nm grain size).

LIST OF PUBLICATIONS

1. X.C. LeQuan, W.P.Kang, J.L. Davidson, B.K. Choi, "The Effect of Cathode Tip Density on Threshold Voltage of Nanodiamond Lateral Vacuum Devices", *Diamond 2009, accepted*.
2. X.C. LeQuan, B.K. Choi, W.P. Kang, J.L. Davidson, "Lateral Device Field Emission Performance: Anode-Cathode Spacing and Diamond Film Thickness", *Materials Research Society, accepted*.
3. X.C. LeQuan, B.K. Choi, W.P.Kang, J.L. Davidson, "Diamond-on-SOI Field Emission Device Patterning", *ECS Transactions - San Francisco, CA vol.18 (2009)*.
4. S. Raina, X. LeQuan, W. Kang, J. Davidson, "Effect of Nitrogen Concentration on Nanodiamond Film Characteristics for Electrode Application", *ECS Symposium:16 - Novel Electrode Materials, accepted*.
5. X.C. LeQuan, W.P. Kang, J.L. Davidson, M. Guo, "Photoluminescence Properties of Nanocrystalline Diamond Grown By MPECVD in CH₄/H₂/N₂ Ambient", *ECS Transactions - Honolulu, HI vol. 16 (2009)*.
6. X.C. LeQuan, W.P. Kang, J.L. Davidson, B.K. Choi, Y.M. Wong, R. Barbosa, W.Lu, "Effect of rearranging sp²/sp³ hybridized-bonding on the field emission characteristics of nanocrystalline diamond films", *Diamond & Related Materials* 18, 200-205 (2009).
7. X.C. LeQuan, W.P. Kang, J.L. Davidson, M. Guo, B.K. Choi, "Micro-Raman, SEM, XPS, and electron field emission characterizations of nitrogen-induced shallow defects on nanodiamond films fabricated with different growth parameters", *Diamond and Related Materials* 18, 191-195 (2009).

REFERENCES

- [1] Xu, N.S. and Latham, R.V., J. Phys. D: Appl. Phys., Vol. 19, p. 477 (1986).
- [2] Brodie 1992, and Spindt C. A., Adv. Electron. Electron Phys. 83 (1992).
- [3] Kim, S., Ju, B. K., Lee, Y. H., Park, B. S., Baik, Y., Lim, S. and Oh, M. H., J. Vac. Sci. Technol. B, vol. 15, no. 2, p. 499 (1997).
- [4] Kang, W.P., Davidson, J.L. and Kerns, D. V., US Patent #6,132,278 (2000).
- [5] Wisitsorathat, A., Ph.D. Dissertation, Vanderbilt University (2002).
- [6] Subramanian, K., Ph.D. Dissertation, Vanderbilt University (2008).
- [7] Liu, H., Dandy, D., Diamond Relat. Mater., 4 1173-1188 (1998).
- [8] Karabutov, A.V., Frolov, V.D., Konov, V.I., Diamond Relat. Mater., 10 840-846 (2001).
- [9] Spindt, C.A., Brodie, I., Humphrey, L. and Westerberg, E.R., J. Appl., Phys. 47 p. 5248 (1976).
- [10] Utsumi, T., Trans. Electron Devices, vol. 38, pp. 2276-2283, (1991).
- [11] Schwoebel, P.R., and Brodie, I. , J. Vac.Sci. Technol. B, vol. 13, pp. 1391-1410 (1995).
- [12] Spindt, C. A., Shoulders, K. R., IEEE 1966 Eight Conference on Tube Techniques, p.143 (1966).
- [13] Spindt, C. A., J. Appl. Phys., vol. 39, p. 3504, (1968).
- [14] Bardeen, J. and Brattain, W.H., Phys. Rev., vol.74, 230-231 (1948).
- [15] Noyce, R.N. 1959, US Patent 2,981,877 (1959).
- [16] Kilby, J.S., IEEE Trans. Electron Devices, vol. ED-23, 648-654 (1976)
- [17] Park, C.-M., Lim, M.-S., Han, M.-K., Physica Scripta, Vol. T79, 327-329 (1999).
- [18] Han S., S-A. Yang, Hwang, T., Lee, J., Lee, J.D., Shin, H., Jpn. J. Appl. Phys. Vol. 39, 2556-2559 (2000).
- [19] Lin, Y.-J., and Wu, K.-C., Appl. Phys. Lett., Vol. 83, No. 25, 5319-5320 (2003).

- [20] Underwood, R.D., Keller, S., Mishra, U.K., Kapolnek, D., Keller, B.P., and DenBaars, S.P. *J. Vac. Sci. Technol. B* 16.2., 822-825 (1998).
- [21] Ye, Fe., Xie, E.Q., Duan, H.G., Li, H., Pan, X.J., *Applied Surface Science* Vol. 253 859-862 (2006).
- [22] Saada, D. (2000). Retrieved April 8, 2008 from Website:
<http://phycomp.technion.ac.il/~david/thesis/node3.html>
- [23] Okano, K. and Gleason, K. K. *Electron. Lett.*, vol. 31, p. 74 (1995).
- [24] Kimura, C., Koizumi, S., Kamo, M., and Sugino, T., *Diamond Relat. Mater.*, vol. 8, pp. 759-762 (1999).
- [25] Geis, M.W., Twichell, Efremow, J.C., Krohn, N.N., Lyszczarz, K., *Appl. Phys. Lett* 68 26 (1996).
- [26] May, P.W. Ludlow, W.J., Hannaway, M., Heard, P.J., Smith, J.A., Rosser, K.N., *Diamond Relat. Mater.*, 17 105–117 (2008).
- [27] Frolov, V.D., Karabutov, A.V., Pimenov, S.M., Konov, V.I., *Diamond Relat. Mater.*, 9 1196 (2000).
- [28] Li, J.J, Zheng, W.T., Gu, C.Z., Jin, Z.S., Gu, G.R., Mei, X.X., Mu, Z.X., Dong, C., *Appl. Phys. A*. 81, 357-361 (2005).
- [29] Ikeda, T., Teii, K., Casiraghi, C., Robertson, J., and Ferrari, A.C. *Journal of Appl. Phys.* 104 (2008).
- [30] Ager, J.W., ER-LTR CRADA OSTI Project, DOI 10.2172/767497 (1998).
- [31] Lee, Y.C., Pradhan, D., Lin, S.-J., Chia, C.-T., Cheng, H.F., Lin, I.N., *Diamond Relat. Mater.*, 14 2055 – 2058 (2005).
- [32] Corrigan T.D., Gruen, D.M., Krauss, A. R., Zapol P., and Chang, R. P. H *Diamond Relat. Mater.*, 11, 43 (2002).
- [33] Milanović, V., Doherty, L., Teasdale, D.A., Parsa, S., and Pister, K.S.J., *IEEE. Trans. Electron Devices*, vol. 48, pp.166-173 (2001).
- [34] Cui, J.B., Ristein, J., and Ley, L. *Phys.Rev. B*, vol. 60, p. 16135 (1999).
- [35] Ding, M., Ph.D. Dissertation, Massachusetts Institute of Technology (2001).
- [36] Davis, B., Ohio State Department of Physics, Physics 103, Website:
<http://www.physics.ohio-state.edu/103/>

- [37] Blumenthal, D., ECE 162B, Lecture 6 (2009).
- [38] Sze, S.M., Ng, K.K., “Physics of semiconductor devices”, John Wiley and Sons, New York, NY (1981).
- [39] May, P.W., Kuo, M.-T., Ashfold, M.N.R., *Diamond Relat. Mater.*, 8 1490 (1999).
- [40] Yiang, K.Y., Yoo, W.J., Guo, Q., Krishnamoorthy, A., *Appl. Phys. Lett.* Vol. 83, No.3 (2003).
- [41] Tsai, C.-H., Ono, T., Esashi, M., *Diamond Relat. Mater.*, 16, 1398-1402 (2007).
- [42] Colinge, J.P., Colinge, C.A., “Physics of Semiconductor Devices”, Kluwer, Moscow (2002).
- [43] Silva, S.R.P, Forrest, R.D., Munindradasa, D.A., and Amaratunga, G.A.J. *Diamond Relat. Mater.*, 7 645-650 (1999).
- [44] Forbes, R.G., *Solid State Electronics* 45 779-808 (2001).
- [45] Hill, R.M., *Phil. Mag* 23, p. 59 (1971).
- [46] Muto, Y., Sugino, Shirafuji, T. J., and Kobachi, K., *Appl. Phys. Lett.*, vol. 59, p. 843 (1991).
- [47] May, P.W., Höhn, S., Wang, W. N., Fox, N.A., *Appl. Phys. Lett.*, vol 72 No. 17, 2182-2184 (1998).
- [48] Castelino, J.A., Master of Engineering in Electrical Engineering, Massachusetts Institute of Technology (1995).
- [49] Joung, D., Chunder, A., Zhai, L. and Khondaker, S.I. *Nanotechnology* 21, 165202 (2010).
- [50] Murgatroyd, P. N., *J. Phys. D: Appl. Phys.* 3, 151 (1970)
- [51] LeQuan, X.C., Kang, W.P., Davidson, J.L., Guo, M., Choi, B.K., *Diamond Relat. Mater.*, 18,191-195, (2009).
- [52] Raina, S., LeQuan, X, Kang, W., Davidson, J., ECS Symposium:I6 - Novel Electrode Materials, accepted (2009).
- [53] Krauss, A. R., Auciello, O., Gruen, D. M., Jayatissa, A. , Sumant, A., Tucek, J., Mancini, D. C., Moldovan, N., Erdemir, A., Ersoy, D., Gardos, M. N., Busmann, H. G., Meyer, E. M., and Ding, M. Q. *Diamond Relat. Mater.*, vol. 10, pp. 1952-1961 (2001).
- [54] Zhu, W., *Vacuum Microelectronics*, Wiley Interscience (2001).

- [55] Wang, S.G., Zhang , Q., Yoon , S.F., Ahn , J., Zhou , Q., Wang , Q., Yang , D.J., Li, J.Q. and Shanyong, S.Z. *Surface and Coatings Technology*, vol. 167, pp. 143-147 (2003).
- [56] Ma, K.L., Zhang, W.J., Zou, Y.S., Chong, Y.M., Leung, K.M., Bello, I., and Lee, S.T., *Diamond Relat.Mater.*, vol.15, pp. 626 – 630 (2006).
- [57] Joseph, P.T., Tai, N.-H., Chen, Y.-C., Cheng, H.-F., Lin, I.-N., *Diamond Relat. Mater.*, 17 476–480 (2008).
- [58] Barbosa, D.C., Almeida, F.A., Silva, R.F., Ferreira, N.G., Trava-Airoldi, .J., Corat, E.J., *Diamond Relat. Mater.* (2009).
- [59] Subramanian, K., Kang, W.P., Davidson, J.L., Choi, B.K., *Diamond Relat. Mater.*, 17 1808–1811 (2008).
- [60] Wu, K., Wang, E.G., Cao, Z.X., *J. Appl. Phys.*, Vol. 88, No. 5, 2967-2974 (2000).
- [61] Wang , S.G., Zhang, Q., Yoon, S.F. , Ahn , J., Zhou, Q., Wang , Q., Yang, D.J., Li J.Q., and Shanyong, S.Z., *Surface and Coatings Technology* 167, 143 (2003).
- [62] LeQuan, X.C., Kang, W.P., Davidson, J.L., Choi, B.K., Wong, Y.M., Barbosa, R., Lu, W., *Diamond Relat. Mater.*, 18, 200-205 (2009).
- [63] Tuck, R.A., Taylor, W., Jones, P.G.A., Latham, R.V., *Proceedings of the 4th International Displays Workshop, Nagoya, 723-7236* (1997).
- [64] Gröning, O., Ph.D. Dissertation, University of Fribourg (1999).
- [65] Toyama, T., Yasuo, K., Masanori, M., *Diamond Relat. Mater.*, 11, 1897-1904 (2002).
- [66] Latham, R.V., London: Academic (1981).
- [67] Latham, R.V., editor, London: Academic (1995).
- [68] Bajic, S, Latham, R.V., *J. Phys. D. Appl. Phys* 21, 200-204 (1998).
- [69] Ferrari, A.C., Satyanarayana, Robertson, B.S., Milne, J., Barborini, W.I., Piseri, E., Milani, P., *Europhys. Lett.*, 42 245-250 (1999).
- [70] Peng, X.L, *Thin Solid Films* 370, 63-69 (2000).
- [71] Xianfeng, Z., M.A. Zhibin, W. Zhenhui, H.E. Aihua, W. Jianhua, Y.Songliu, *Plasma Sci. Technol.* 10, 336 (2008).
- [72] Filik,J., *Spectroscopy Europe*, Vol. 17 No. 5 p. 10-17 (2005).

- [73] Pfeiffer, R., Kuzmany, H., Knoll, P., Bokova, S., Salk, N., Gunther, B., *Diamond and Related Materials* 12, 268-271 (2003).
- [74] Lubbe, M., Bressler, P.R., Drews, D., Braun, W., Zahn, D.R.T., *Diamond Relat. Mater.*, 7, 247-249 (1998).
- [75] Subramanian, K., Kang, W.P., Davidson, J.L., Howell, M., *Diamond Relat. Mater.*, 14 404-410 (2005).
- [76] Nordheim, L. W., *Proc. Roy. Soc. Lond.* A121 626 (1928).
- [77] Oro, J.A., Ball, D.D., *J. Vac. Sci. Technol. B* 11, pp. 464-467 (1993).
- [78] Davidson, J.L., Kang, W.P., Subramanian, K., Wong, Y.M., *Phil. Trans. R. Soc. A* 366, 281-293 (2008).
- [79] Liou, Y-L., Liou, J-C., Huang, J-H., Tai, N.H., Lin, I-N., *Diamond Relat. Mater.*, 17, 776-781 (2008).
- [80] Subramanian, K., Kang, W. P., and J. L. Davidson, *IEEE Electron Device Letters* (2008).
- [81] LeQuan, X.C., Kang, W.P., Davidson, J.L., Choi, B.K., *Diamond 2009 Conference Abstract*, accepted (2009).
- [82] Gorecka-Drzazga, A., Dziuban, J.A., Gorol, M., *IEEE* 208-209 (2005).
- [83] Spindt, C.A., Holland, C.E., Rosengreen, A., Brodie, I., *IEEE Transactions on Electron Devices*, 38, 2355-2363 (1991).
- [84] Jiang, Y., Carnegie Mellon, Electrical and Computer Engineering Data Storage Systems Center (2005).
- [85] Babin, S., Cabrini, S., Dhuey, S., Harteneck, B., Machin, M., Martynov, A., Peroz, C., *Microelectronic Engineering*, Article in Press (2009).
- [86] Otterbach, R., Hilleringmann, U., Goser, K., *IEEE*, 1873-1877 (2000).
- [87] Rozen, S., Hagooly, A. J. Wiley & Sons, New York (2004).
- [88] Dorsch, O., Werner, M., Obermeier, E., *Diamond Relat. Mater.*, 4, 456-459 (1995).
- [89] Thuy, B., European Patent Office, 0573212A2.
- [90] Gupta, S., Morrell, G., and Weiner, B.R. *Journal of Appl. Phys.* Vol 95, No. 12, 8314-8320 (2004).

[91] Koeck, F.A.M., and Nemanich, R.J., *Diamond Relat. Mater* 15, 217-220 (2006).

[92] Lee, C.-S. and Han, C.-H. *Sensors and Actuators A* 97-98, 739-743 (2002).

[93] Chou, T.C. and Tu, K.N., *Appl. Phys. Lett.* 52 (16) 1317-1319 (1998).

APPENDIX A

FIELD ENHANCEMENT FACTOR CALCULATION

A.1 β enhancement:

The occasion of sharp micro/nano tips and increased sp^2 for low field emission is well known. Modeling the field enhancement effect of the cathode emitter geometry (β_{geometry}) and sp^2 content (β_{sp^2}) would provide useful insight into the field emission performance of each diode as the emission gap was scaled into the sub-micron dimensions. In agreement with Wisitsorat-at, the work function for all emitter tips derived from the same diamond film remains constant [5]; the β_{sp^2} contribution to the total enhancement factor may be solved given the estimated β_{geometry} . The following table summarizes the enhancement factors for the 500 nm, 850 nm, and 1.5 μm gap lateral diodes. Given the nitrogen-incorporated nanodiamond film work function of ~ 0.6 eV from Chapter III and an estimated β_{geometry} value for the 500 nm gap device based on SEM measurements, the β_{sp^2} contribution is ~ 1.2 . The remaining β_{geometry} for the 850 nm and 1.5 μm gap devices can be solved algebraically. The order in magnitude of the β_{geometry} and β_{sp^2} shown in Table A.1 are in agreement with the values reported by Wisitsorat-at ($\beta_{\text{sp}^2} = 2.42$) and Subramainan ($\beta_{\text{geometry}} \sim 1300$) [5-6].

Gap (μm)	β_{total}	β_{geometry}	β_{sp^2}
0.5	1587	1300	1.2
0.85	1580	1320	1.2
1.5	3130	2600	1.2

Table A.1. Summary of enhancement factors for the 500 nm, 850 nm, and 1.5 μm gap lateral diodes.

APPENDIX B

CALCULATION DETAILS

B.1 Field-enhanced Thermionic Emission (FTE)

From Table 2.1, FTE can be expressed by the equation:

$$J = A^{**} T^2 \exp\left(\frac{-q(\phi_B - \sqrt{qE_i} / 4\pi\epsilon_i)}{kT}\right) \quad (\text{B.1})$$

where A^{**} is the Richardson constant, $\sim 120 \text{ A/cm}^2 \cdot \text{K}^2$ ($1.2 \text{ } \mu\text{A}/\mu\text{m}^2 \cdot \text{K}^2$) [91], T is the temperature (in K), ϕ_B (V) is the barrier height, E_i is the electric field in the emitter material, kT/q is the thermal voltage at room temperature (0.0258 V) and ϵ_i is $5.7 \times \epsilon_0$ for diamond [5], with ϵ_0 being the vacuum permittivity ($8.85 \times 10^{-18} \text{ F } \mu\text{m}^{-1}$). Using these parameters to calculate the theoretical current, the corresponding theoretical FTE conformance is shown in Figure B.1. The extracted barrier height using the intercept from the FTE scale for the 500 nm and 850 nm gap configurations are $\sim 0.38 \text{ V}$ and $\sim 0.66 \text{ V}$, respectively. The variation in barrier height would affect the net transfer of electrons and would help to explain the difference in the transition point from Fowler-Nordheim behavior between the two devices seen in Figure 5.26.

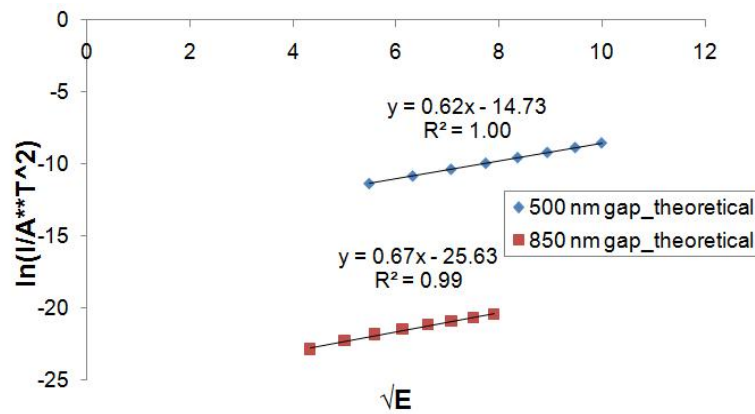


Figure B.1. The 500 nm and 850 nm gap devices show conformance to the field-enhanced thermionic model at $E > 20 \text{ V}/\mu\text{m}$. The barrier height, ϕ_b , for the 500 nm and 850 nm gap configurations are $\sim 0.38 \text{ V}$ and $\sim 0.66 \text{ V}$, respectively.

A lowered barrier height would facilitate the emission of electrons into vacuum; a condition where the emission occurs more rapidly than can be accommodated by the electron supply would cause space charge limited current to arise. The difference in barrier height for the two devices are more distinct in the theoretical model shown in Figure B.1 when compared to the experimental data model shown in Figure 5.27 a).

B.2 Space charge limited current (SCLC)

From Table 2.1, SCLC conduction can be expressed by:

$$J = \left(\frac{9\epsilon_i \mu V^2}{8d^3} \right) \quad (\text{B.2})$$

where ϵ_i is $5.7 \times \epsilon_0$ for diamond [5] with ϵ_0 being the vacuum permittivity ($8.85 \times 10^{-14} \text{ F cm}^{-1}$), the electron mobility μ is $10 \text{ cm}^2 \text{ V}^{-1} \text{ s}^{-1}$ [29], and the constant d represents the diamond material thickness (μm). If the mobility of the sample is low, then charge injection would be limited by the rate at which the charge can be transported to a junction interface [48]. The emission current is a function of applied bias; the theoretical SCLC conformance for the 500 nm and 850 nm gap configurations would overlap, as shown in Figure B.2.

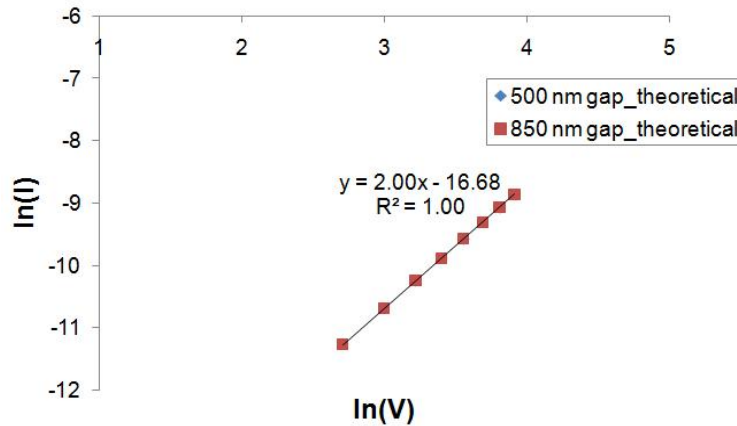


Figure B.2. With the 500 nm and 850 nm gap devices fabricated from the same nanodiamond film, the theoretical SCLC model for both devices at $E > 20\text{V}/\mu\text{m}$ is shown.

B.3 Discussion of experimental vs. theoretical sub-micron gap FTE and SCLC parameters

Our experimental results demonstrate that as the emission gap is scaled into the sub-micron regime, other accepted conduction mechanisms may arise. The conclusions are consistent with other reported work using nanodiamond [47, 91]. As expected, the experimental data for the 500 nm and 850 nm gap devices deviate from theoretical values due to testing non-idealities; however, it can be shown that our results highlight the same FTE and SCLC conformance trends as the theoretical data shown in Figures B.1. and B.2. While the experimental and theoretical potential barrier height for the 500 nm gap configuration are the same at ~ 0.38 V, the potential barrier height deviation seen in the 850 nm gap configuration, ~ 0.42 and ~ 0.66 V, may be attributed to the structural changes as a result of extended voltage cycling (applying electric field) to obtain experimental data. The deviation from the theoretical SCLC slope of 2 towards lower values, which is more evident in the 500 nm gap device, indicates that charge injection limitation is occurring closer to the vacuum interface rather than the nanodiamond bulk [43]. Additionally, the discrepancy in the actual SCLC slope for the 500 nm and 850 nm gap configurations may be attributed to the differences in the potential barrier height, which in turn helps to explain the change in transition point from F-N tunneling seen in Figure 5.26.